# 博士論文

# Studies of Electric Conduction and Phase Transition Mechanisms in Neutral-Ionic Transition Materials

# （中性 - イオン性転移物質の電気伝導および相転移機構の研究）

竹原　陵介

# Acknowledgments

I would like to express my sincere gratitude to Professor Kazushi Kanoda for his thoughtful guidance, incentive discussions, and enlightening suggestions.

I would like to express my appreciation to Kazuya Miyagawa for his continual encouragements, and daily experimental supports.

I am very grateful to H. Okamoto for the sample preparation, and helpful discussions.

I would like to thank to N. Nagaosa, A. Maeda, and F. Kagawa for fruitful discussions and comments.

I am very grateful to T. Miyamoto, H. Uemura, H. Matsuzaki, H. Tanigchi, K. Matsubayashi, and Y. Uwatoko for their valuable cooperation in my experiments.

I would like to say thank to M. Hosoda, T. Nishikawa, and K. Sunami for useful discussions.

I am grateful to all the members of Kanoda Laboratory for helpful discussions and sharing joys through daily research life.

Finally, I would like to thank my parents and brother for kind encouragements.

# Contents

# Chapter 1 Introduction

This chapter gives the background, motivation, and purpose of the present study. In the background section, we explain the general properties of neutral-ionic transition and summarize the previous theoretical and experimental results. Finally, we raise unsolved problems and describe the purpose of the present work.

## 1.1 Introduction

The properties of a solid depend on the degrees of freedom of charge, spin, lattice, and orbital. Furthermore, interactions between these degrees of freedom give systems diversity in physical properties. For instance, it is well known that by onsite Coulomb interactions between electrons, a system with a half-filled band changes from a metal to an insulator (Mott transition). To understand, and control the phenomena in such correlated systems and develop new states are among central issues in modern material science. In this thesis, we focus on neutral-ionic transition systems, because they have strong electron-electron and electron-lattice interactions. Furthermore, charge, spin, and lattice are intricately interrelated in the neutral-ionic transition system. In the present study, we investigate the neutral-ionic (NI) transition systems form a point of view of charge degree of freedom. Adding to this, we have tried to metalize the neutral-ionic transition systems in order to develop possible novel metallic states.

Here, we describe the characteristic properties of organic materials, where the basis unit of crystal can be assumed to be a molecule rather than an atom. Because the transfer integrals within a molecule is much larger than those between the molecules, we can treat molecular orbital (MO) in organic systems like atomic orbital in inorganic systems and the tight binding approximation using MO and their transfer integrals is turns out to be effective. Because of the low symmetry of a molecule frame, the energy levels of MO are not degenerate in many cases and the energy splitting between MO's are much larger than the energy scale of room temperature. Thus, it is reasonable to take into consideration only the highest occupied molecular orbital (HOMO) and/or the lowest unoccupied molecular orbital (LUMO) for the band structure calculations. Then, the organic materials have simple electron structures. In some systems, the band width is comparable with electron interactions; these salts can be regarded as correlated electron systems. Since the molecules condensate into a solid mainly due to the Van der Waals force, the molecular solid is highly compressible. Therefore, pressure is an effective external parameter to vary the transfer integrals and the Coulomb interactions in the neutral-ionic transition materials

The present thesis describes the transport study of the neutral-ionic transition systems under pressure. The content of this thesis is as follows. In Chapter 2, we describe the experimental methods

for investigating the transport properties of controlled temperatures and pressures. In Chapter 3, we present the experimental data of TTF-CA around the neutral-ionic transition/crossover and argue the mechanisms of the charge transport and the phase transition. Chapter 4 describes the experiments performed with the aim at making the neutral-ionic systems metallic. Chapter 5 concludes the present study.

## 1.2 Background

### 1.2.1 Neutral-ionic transition

The neutral-ionic (NI) transition is mainly observed in quasi-one-dimensional mixed-stack organic charge transfer complexes, where two kinds of molecules are arranged alternately; one is a donor molecule and the other is an acceptor molecule (Fig. 1.2.1) [1]. The transfer integral along the stacking axis, is larger than that in other directions, making the electronic state one-dimensional [2]. In the following, we explain the NI transition in tetrathiafulvalene-*p*-chloranil (TTF-CA, Fig. 1.2.2 (a)), which is studied in this thesis.

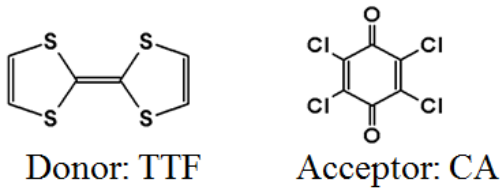


Fig. 1.2.1. Donor molecule TTF and acceptor molecule CA of the neutral-ionic system TTF-CA.

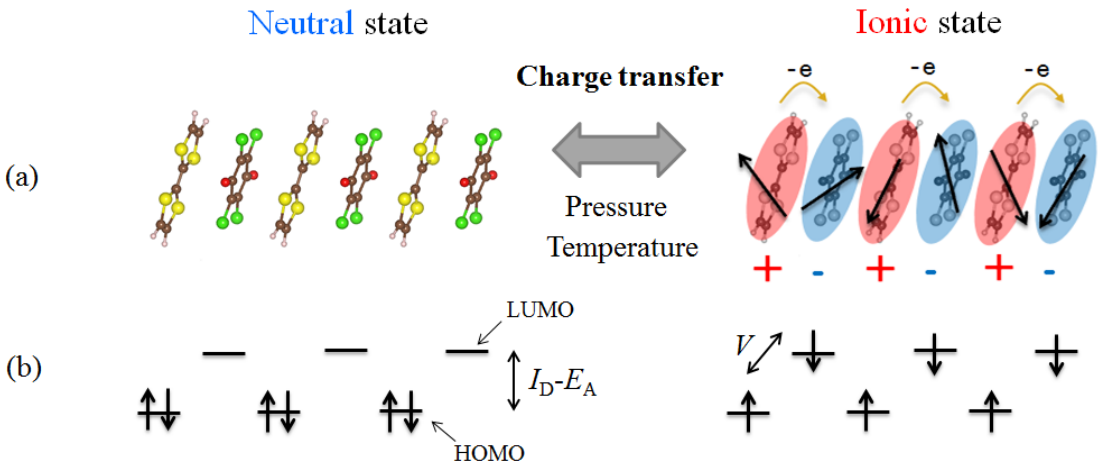


Fig. 1.2.2. (a) Quasi-one-dimensional mixed-stack charge transfer complex TTF-CA. (b) The energy levels of the HOMO of the donor molecule and the LUMO of the acceptor molecule.

The NI transition is a charge transfer transition between donors and acceptors, leading to a modification of the chemical bond. In the neutral state, each molecule has a closed shell structure, in which, the HOMO of the donor molecule are filled with two electrons and the LUMO of the acceptor molecule are vacant (Fig. 1.2.2 (b)). The molecular bonding is due to van der Waals forces. When pressure is applied or temperature is lowered, an electron moves from the HOMO of the donor molecule to the LUMO of the acceptor molecule, making the molecular bonding ionic [1, 3]. The electronic energy of the neutral state is determined by the energy difference between the HOMO of the donor and the LUMO of the acceptor molecules, expressed as $I_D$-$E_A$, where $I_D$ and $E_A$ are the ionization energy of the donor molecule and the electron affinity of the acceptor molecule, respectively. The electronic energy of the ionic state is described in terms of the Madelung energy gain $\alpha V$, corresponding to the total Coulomb energy gain, where $\alpha$ is a Madelung constant and $V$ is the Coulomb repulsive energy acting between the neighbor donor and acceptor molecules. According to the calculation for the one-dimensional point charge model, the Madelung constant is 2ln2. When the energy difference, $I_D$-$E_A$, is larger than the Madelung energy $\alpha V$, the electrons keep staying in neutral donor and acceptor molecules; however, in case $\alpha V > I_D$-$E_A$, an electron transfers from a donor molecule to an acceptor molecule, causing the system to undergo the NI phase transition. In reality, the NI transition is observed under pressure, since the Madelung energy $\alpha V$ is increases with increasing pressure as a result of lattice contraction.

The NI transition was first theoretically predicted by H. M. McConnell [4] and discovered by J. B. Torrance [1]. Torrance provided the fundamental concept of the NI transition as explained above. Moreover, he introduced a charge transfer (CT) energy, which is required to generate a CT exciton in the neutral or ionic background. When the system is in the neutral state, it is the energy to create an ionic donor/acceptor pair (ionic DA pair) and is given by the form of $h\nu_{CT}=I_D$-$E_A$-$V$. When the system is in the ionic state, it is the energy to create one neutral DA pair, which is given by $h\nu_{CT}=(2\alpha$-1$)V$-($I_D$-$E_A$). Torrance examined $h\nu_{CT}$ and $I_D$-$E_A$ of many materials at ambient pressure and summarized them as shown in Fig. 1.2.3. The $h\nu_{CT}$s have V shape. The line in the right side follows $h\nu_{CT}=I_D$-$E_A$-$V$, and the left line shows $h\nu_{CT}=(2\alpha$-1$)V$-($I_D$-$E_A$). Various materials can be located in this diagram, which distinguishes the neutral and ionic systems. The cross point of the two lines corresponds to the NI phase boundary; that is, $I_D$-$E_A=\alpha V$. The CT energy provides information on the lowest one-particle excitation energy in the NI system, and is referred to in the discussion of the present results in Chapter 3.

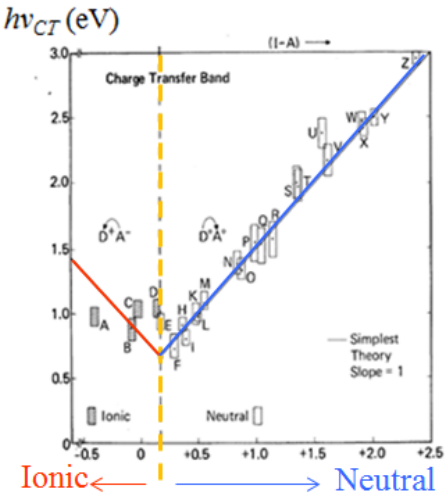


| Symbol | Compound | N/I |
|---|---|---|
| A | TMPD-tetrafluoroTCNQ | I |
| B | dimethylphenazine-TCNQ | I |
| C | TMPD-TCNQ | I |
| D | TMPD-chloranil | I |
| E | TMDAP-TCNQ | N |
| F | TTF-chloranil | N |
| G | TTF-fluoranil | N |
| H | DibenzeneTTF-TCNQ | N |
| I | DEDMTSeF-diethylTCNQ | N |
| J | TMDAP-fluoranil | N |
| K | TTF-dichlorobenzoquinone | N |
| L | perylene-tetrafluoroTCNQ | N |
| M | perylene-DDQ | N |
| N | perylene-TCNE | N |
| O | perylene-TCNQ | N |
| P | TTF-dinitrobenzene | N |
| Q | perylene-chloranil | N |
| R | pyrene-TCNE | N |
| S | pyrene-chloranil | N |
| T | anthracene-chloranil | N |
| U | hexamethylbenezene-chloranil | N |
| V | naphthalene-TCNE | N |
| X | anthracene-PMDA | N |
| Y | anthracene-tetracyanobenzene | N |
| Z | phenanthrene-PMDA | N |

Fig. 1.2.3. Torrance diagram [1]. The blue line expresses $h\nu_{CT}=I_D-E_A-V$ and the red line expresses $h\nu_{CT}=(2\alpha-1)V-(I_D-E_A)$. At the cross point of these lines, the relation of $I_D-E_A=\alpha V$ holds. Indexes from A to Z indicate the NI materials.

The NI transition described above is the simplest case, where the charge transfer $\rho$ from donor to acceptor is zero or 1. In reality, however, $\rho$ takes intermediate values because of transfer integrals between the molecules, which bring quantum mixing of the neutral and ionic states [5-13]. For example, in the neutral state of TTF-CA at ambient pressure and room temperature, $\rho$ is not 0 but 0.3. The transfer integral causes the mixture of the donor and the acceptor orbitals. In the neutral state, two electrons are in the HOMO-dominant orbital, and in the ionic state, one electron is in the HOMO-dominant orbital and the other electron is in the LUMO-dominant orbital. Even above the NI transition temperature, there are thermal and quantum fluctuations between the neutral and the ionic states, which makes the charge transfer, $\rho$, an intermediate value (Fig. 1.2.4).

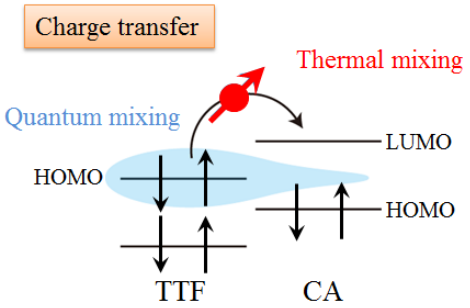


Fig. 1.2.4. Schematic of quantum mixing and thermal mixing.

### 1.2.2 Lattice Dimerization

The NI transition itself is a transition in the degree of charge transfer, $\rho$ without symmetry breaking. However, most of the NI transitions observed until now accompany lattice dimerization. The dimerization involves an inversion symmetry breaking, which causes ferroelectricity, and the real NI transitions accompany symmetry breaking.

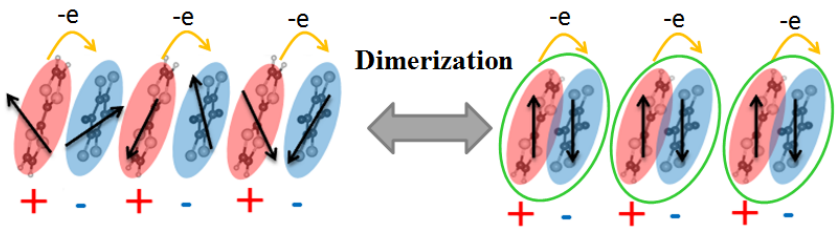


Fig. 1.2.5. Schematic dimerization of molecules. Left: non dimerized ionic molecules. Right: dimerized ionic molecules.

The dimerization occurs only in the ionic state, and figures of non dimerized and dimerized ionic cases are shown in Fig. 1.2.5. The spin-Peierls mechanism is suggested for the origin of lattice dimerization theoretically. The ionic state has no charge degrees of freedom but is paramagnetic if there is no lattice dimerization. The spins form one-dimensional chains, where spins are antiferromagnetically interacting with the exchange interaction $J$, which is derived from the second-order perturbation of the Hubbard model. It is well known that one-dimensional systems have Peierls instability. The lattice displacement, $u$, is taken as the order parameter of the lattice dimerization. The magnetic energy gain and the energy cost of the lattice elastic energy can be described with $u$ in a one-dimensional antiferromagnetic Heisenberg model; the magnetic energy gain is proportional to the four-third power of $u$ and the lattice elastic energy is proportional to the square of $u$ [14]. Thus, there is a range of finite $u$ such that the magnetic energy gain is larger than the lattice elastic-energy cost, leading to the spin-Peierls transition. So, the total energy gain depends on the electron-lattice interaction, and the NI systems have been considered to be strongly electron-lattice-coupled systems.

### 1.2.3 Physical properties of TTF-CA

TTF-CA is one of the most celebrated NI transition materials, and plenty of theoretical and experimental studies have been carried out on TTF-CA over thirty years since the NI transition was discovered. In this section, the physical properties, especially at ambient pressure, are explained.

Many experiments on the NI systems have been performed to know the degree of the charge transfer $\rho$, which characterized the NI transition. The experimental methods to measure $\rho$ are infrared (IR) spectroscopy [5-12], visible light spectroscopy [9, 16], and nuclear quadrupole resonance (NQR) [17]. In the IR spectroscopy, particular molecular vibrations are sensitive to molecular charge and the frequency shift reflects the amount of charge transfer [7]. It is known the transferred charge from the donor to the acceptor is concentrated around C=O in the CA molecule, making the frequency of the C=O stretching mode. Thus, by observing the change of the frequency of the C=O stretching mode, the change of $\rho$ can be known. The absolute values of $\rho$ are obtained from a proportional relation between $\rho$ and the frequency [13, 18]. An experimental result of $\rho$ against temperature variation at ambient pressure is given in Fig. 1.2.6, where the $b_{1u}\nu_{10}$ vibrational mode of CA is observed by using a polarized light parallel to **b** axis, which is different from the one-dimensional stacking direction [19]. A jump of $\rho$ from 0.32 to 0.55 is observed at 81K, where the NI transition occurs, and the discontinuous behavior indicates the NI transition at ambient pressure is the first-order transition. In the low-temperature ionic phase, the value of $\rho$ is approximately 0.55, which is far from $\rho$=1, indicating that the ionic phase is not a complete ionic state.

The low-temperature ionic state is also known as the dimerized state. The $a_g$ vibrational mode, which is sensitive to the dimerization, is activated only when the symmetry is broken. Fig. 1.2.7 shows the temperature dependence of the reflectance spectra for a polarized light parallel to the **a** axis. It is clear that the $a_g$ modes are strongly activated below 81K [20].

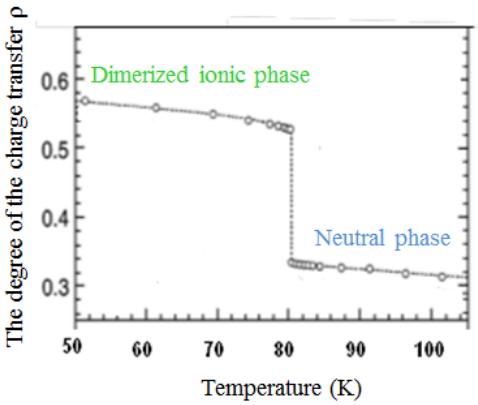


Fig. 1.2.6. Temperature dependence of the degree of the charge transfer ρ at ambient pressure [19].

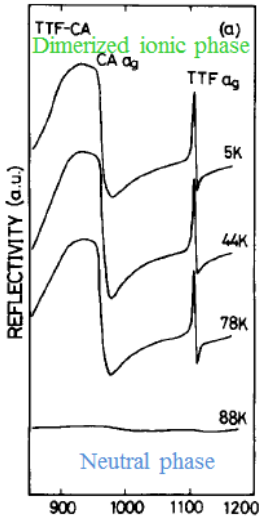


Fig. 1.2.7. Temperature dependence of the reflectance spectra around the frequency of the $a_g$ modes at ambient pressure [20].

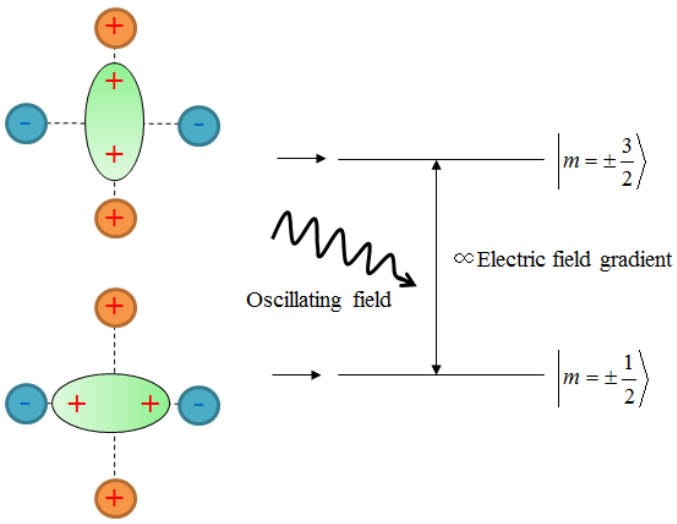


Fig. 1.2.8. Schematic of nuclear quadrupole resonance (NQR).

The NQR measurements can also probe the charge transfer and the dimerization [21-23]. The most different point between the IR measurements and the NQR measurements is in their time scales. The NQR measurements use the quadrupole moments of nuclei as probes, whose resonance has much slower time scale, $10^6$~$10^8$Hz, than that of molecular vibrations of the IR probes, $10^{13}$~$10^{15}$Hz [16]. The difference of the time scale is sometimes a decisive point in the interpretation of experimental results, as seen later about the problem of the dimerization.

In the NQR measurements of TTF-CA, chlorine-35 ($^{35}$Cl) of the CA molecule is used as the probe. The CA molecule has four $^{35}$Cl nuclei, which have nuclear quadrupole moments nuclear spins $I$=3/2 [24]. The nucleus with a quadrupole moment can be modeled intuitively to an ellipse shape, and an orientation of the ellipse corresponds to that of the nuclear spin as schematically shown in Fig. 1.2.8. In a situation where the surrounding electronic charges make an electric field gradient at the nuclear site, the nucleus is turned around in such a way that a state of $m$=±3/2 becomes a high energy state and a state of $m$=±1/2 becomes a low energy state. The energy splitting between the two states is proportional to the electric field gradient. For example, the energy splitting in $^{35}$Cl NQR for TTF-CA is around 37MHz, which is a very slow time scale in comparison with the optical measurements [17, 25]. Differently from the NMR measurements, the energy splitting corresponding to the states between $m$=±3/2 and $m$=±1/2 is spontaneously yielded by circumstances around the nucleus in a crystal even without magnetic field. These principles of the NQR measurements indicate that if the charge distribution surrounding the nucleus is changed by the charge transfer from a donor to ac acceptor, the energy splitting is changed. Thus, one can detect the charge transfer by means of the change of the resonance frequency corresponding to the energy splitting. Furthermore, the spectra have information on the symmetry of the crystal. TTF-CA in the neutral state has two pairs of equivalent $^{35}$Cl in a CA molecule with inversion center on CA (Fig. 1.2.9), and two lines are observed [22]. In contrast, in the dimerized state all the four $^{35}$Cl in a CA become nonequivalent (Fig 1.2.9), resulting in four distinguished lines. Therefore, the number of lines gives a yes/no answer to the question whether TTF-CA is dimerized or not.

The temperature dependence of the NQR frequency at ambient pressure is shown in Fig. 1.2.9. At 81K, a jump of the resonance frequency is observed, and simultaneously the spectra are split; each of the two resonance lines further split into two, yielding four lines in total below 81K. These results indicate that the charge transfer and the dimerization occur at the same time at 81K as the first-order transition. As these results show, the NQR measurements have such advantage that the charge transfer and the dimerization can be observed at one time. A curve of the resonance frequency from the room temperature to 81K obeys Koukoulas's rule that the resonant frequency shift is determined by the average of the anisotropic electric field gradient (tensor) fluctuating due to a thermal motion of the electronic environments, namely molecules [26]. This gives some ambiguity to the estimation of accurate values of $\rho$ from the NQR resonance frequency.

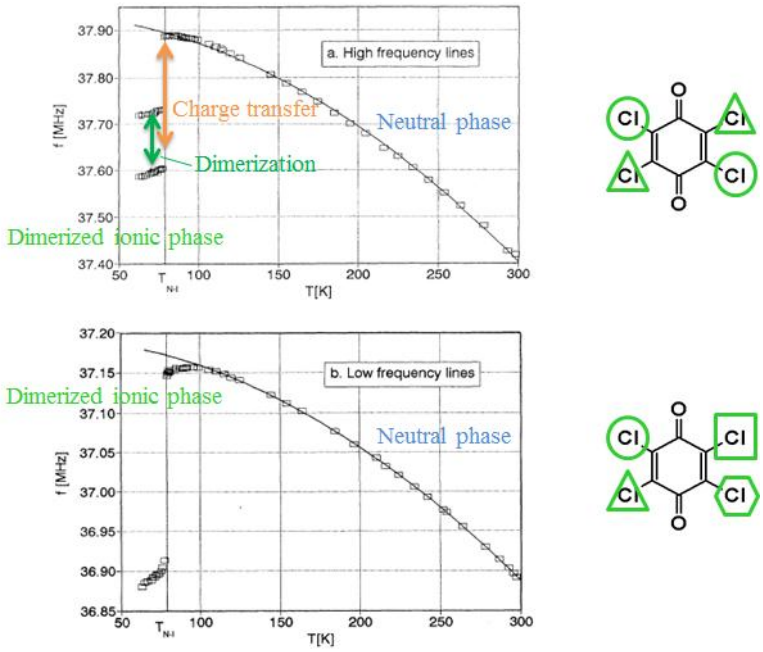


Fig. 1.2.9. Temperature dependence of the NQR resonance frequency [22]. In the neutral phase, two resonant frequencies can be observed, corresponding to two pairs of equivalent $^{35}$Cl in the crystal (see the upper right figure). In the dimerized ionic phase, each of the two lines further splits into two due to the symmetry-breaking dimerization and totally four resonant lines are observed because all $^{35}$Cl become nonequivalent. However, the lowest two resonant frequencies are not resolved appreciably.

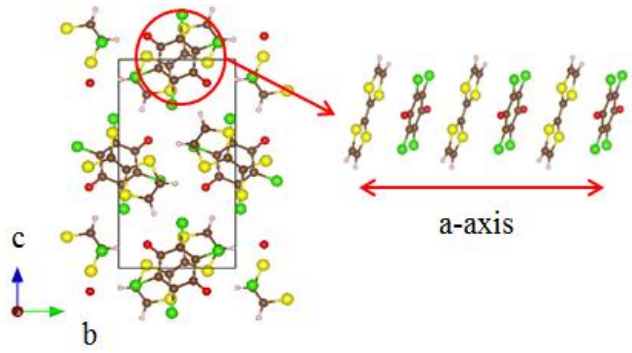


Fig. 1.2.10. Structure of TTF-CA at ambient pressure and room temperature.

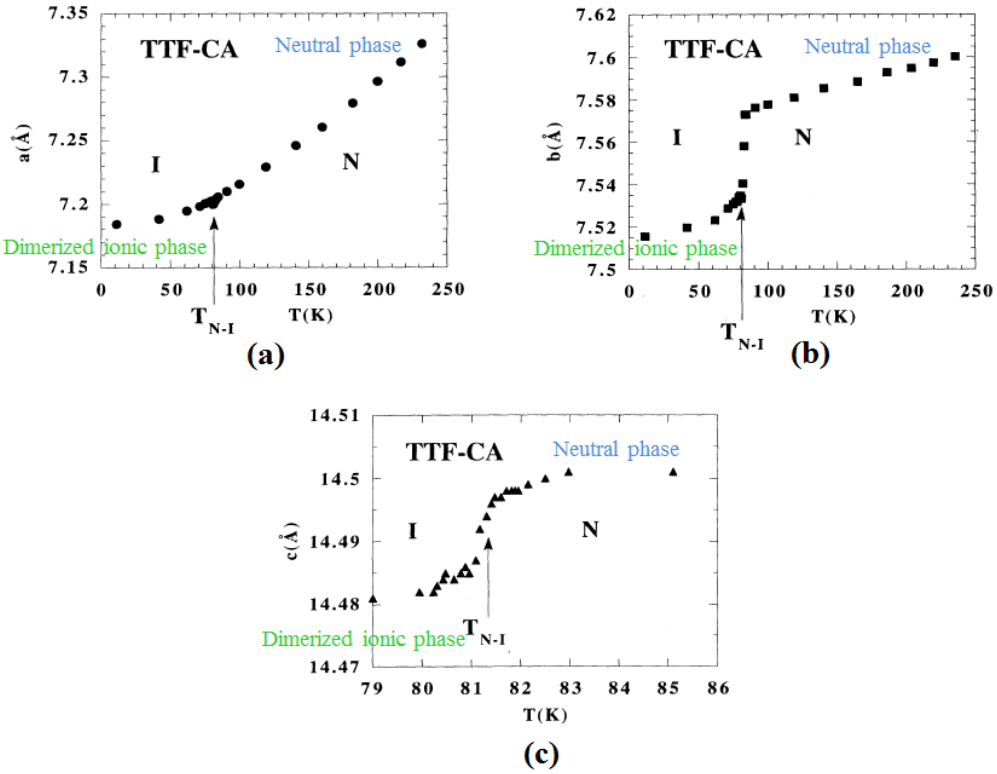


Fig. 1.2.11. Lattice constants of TTF-CA at ambient pressure. (a), (b) and (c) correspond to the lattice constant of the **a**, **b** and **c** axes, respectively [28].

Here, we give a detailed explanation on the crystal structure of TTF-CA. X-ray diffraction and neutron scattering experiments were performed to determine the structure of TTF-CA [27-29]. The schematic structure of the unit cell at room temperature and the temperature dependence of lattice constants of TTF-CA are shown in Fig. 1.2.10 and Fig. 1.2.11, respectively.

At room temperature, the lattice constants of **a**, **b**, **c** axes are 7.40, 7.620, 14.59Å, respectively. The **a** axis corresponds to the one-dimensional chain direction in which TTF and CA molecules stack alternately, and thus the distance between the two molecules TTF and CA is the half value of 7.40Å, namely, 3.7Å. While the lattice constants of the **b** and **c** directions show clear change at the NI transition, there is no appreciable change in the lattice parameter of the **a** direction (Fig. 1.2.11 (a)), but the intradimer and interdimer donor-acceptor distances get unequal to 3.504 and 3.685Å , respectively. The change of the intradimer donor-acceptor distance is 1.26% [28]. It is noteworthy that this change is much larger than the changes in the **b** axis (0.5%) and the **c** axis (0.1%) at the transition temperature. Additionally, the abrupt change of the unit-cell volume corroborates the

first-order nature of the NI transition at ambient pressure from the thermodynamic point of view.

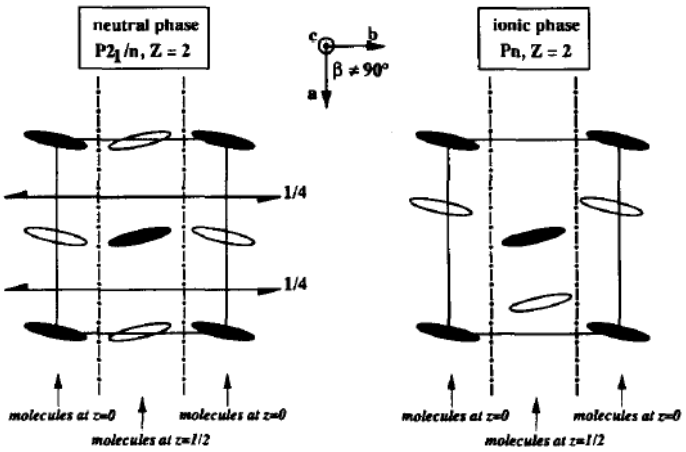


Fig. 1.2.12. Unit cell of TTF-CA projected onto the **ab** plane. The unit cell in the high temperature neutral phase (left ) and the unit cell in the low temperature dimerized ionic phase (right) [29].

Fig. 1.2.12 shows the unit cell projected onto the **ab** plane [29]. The left and right panels in Fig. 1.2.12 show the unit cells in the neutral and dimerized ionic states, respectively. The crystal structure of the neutral state is monoclinic with the space group of $P2_1/n1$. The **a** axis and **b** axis are normal to each other (that is, $\gamma=90°$), but the **c** axis is not perpendicular to the **ab** plane. The unit cell contains two equivalent TTF and CA molecules, which are located on inversion centers at (1/2, 1/2, 0) and (0, 1/2, 0), respectively. This crystal has two important symmetry, screw and glide symmetries. There is a screw axis $2_1$ parallel to **b** axis, which contributes to systematic extinction: $0k0$: $k=2n+1$. There is also a glide plane parallel to **ac** plane, which contributes to systematic extinction: $h0l$: $h+l=2n+1$. In the low temperature ionic phase, the structure is changed to a triclinic crystal and the space group becomes $P1n1$, indicating that the inversion symmetry that exists in the neutral state disappears. The change of space group was confirmed by an appearance of a Bragg spot of (0 3 0), as seen in Fig. 1.2.13, shows a first-order structural transition. In contrast, the systematic extinction $h0l$: $h+l=2n+1$ still remains below the transition temperature, which indicates that the structure in the dimerized ionic state has the glide symmetry. This means that the equivalent two molecules in the unit cell move in the same direction (Fig. 1.2.12), and thus TTF-CA has the ferroelectricity not antiferroelectricity.

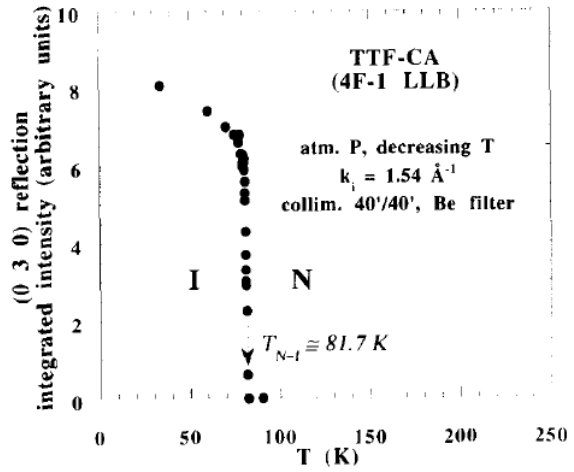


Fig. 1.2.13. Temperature dependence of the integrated intensity of the X-ray reflection (0 3 0) [29].

The ferroelectricity of TTF-CA was confirmed by a *P-E* hysteresis curve, where *P* is polarization and *E* is an external electric field, and this experiment shows that TTF-CA has a large polarization value of 7~9 μC/cm$^2$ [30]. Furthermore, electronic ferroelectricity was suggested by X-ray diffraction under an electric field, where the ionic molecules move in the opposite direction to the electric field. The polarization is predicted not to be the conventional polarization that displacement of the ionic molecules makes, but to be electronic polarization that the displacement of the electrons makes [30, 31, 32].

It is suggested that the electrons in the dimerized ionic phase of TTF-CA are not completely localized but are in the intermediate state between the localized and itinerant states [31, 32]. In fact, the degree of the charge transfer $\rho$ deviated sizably from 1 as described above, which provides a room for discussion against the thought that the transition at 81K is the spin-Peierls transition and invokes the Peierls transition [33]. However, it does not make sense to distinguish whether the dimerization is due to the spin-Peierls or Peierls mechanism, because they are the limiting pictures and the real systems are situated in between them. The relation between $\rho$ and the dimerization is also examined in terms of the electron-lattice interaction [34, 35]. When the electron-lattice interaction is weak, the transition with change of $\rho$ is of the first order, but in contrast the electron-lattice interaction becomes strong, the transition has the continuous nature. Among the NI materials, dimethyl-tetrathiafulvalene-chloranil, represented as DMTTF-CA, shows the continuous transition at ambient pressure, which is predicted to have the strong electron-lattice interaction [10, 36-41].

The ground states of TTF-CA have so far been reviewed. Next, the excited states of TTF-CA are

described. In the previous section, we have seen the mechanism of charge transfer of TTF-CA, which corresponds to a one particle excitation. However, it has been suggested that the low-energy properties of the NI system cannot be explained only by such one-particle excitations; the NI system should have other particular excitations, a neutral-ionic domain wall (NIDW), a charge soliton and a spin soliton [34, 42]. The NIDWs can be generated at the boundary between the neutral and ionic phase below the first-order transition, as illustrated in Figs. 1.2.14 (a) and (b). Interestingly, the NIDW is suggested to be not classical but quantum in nature [42]. There are two kinds of NIDW. One is the NIDW generated between the neutral and the non-dimerized ionic phases (Fig. 1.2.14 (a)), and the other is the NIDW generated between the neutral and the dimerized ionic phases (Fig. 1.2.14 (b)). The former is created in no association with the lattice, but the latter accompanied by dimerization in the ionic phase due to the electron-lattice coupling and is called the lattice relaxed (LR-) NIDW.

The generation of the solitons is deeply related to the dimerization. In the dimerized phase, the inversion symmetry disappears, and as a result, two degenerate ground states, which correspond to the two types of direction of the polarization, appear. In between the two polarizations in opposite directions to each other, there can appear an unpaired molecule, which is the soliton [43, 44]. There are two types of the solitons: one is the charge soliton (Fig. 1.2.14 (c)) and the other is the spin soliton (Fig. 1.2.14 (d)). The charge soliton is a soliton where the unpaired molecule is in the neutral state, which has effective charge but doesn’t have a spin. The spin soliton is a soliton where the unpaired molecule is in the ionic state, which has both effective charge and a spin; however, it is distinguished from the spin soliton in polyacetylene that has only a spin but not effective charge [45].

Because these excitations have the charge or the spin, in the NI system, the excitations can respond to external fields. For example, in the neutral phase at ambient pressure, the excitations of LR-NIDW's are predicted to take on dielectric responses (Fig. 1.2.15) [46]. In the same temperature region, the existence of the LR-NIDW's is also indicated by X-ray diffuse scattering measurements (Fig. 1.2.16) [47]. In the low-temperature dimerized ionic phase, some isolated spins are observed by the ESR measurements regardless of the non-magnetic phase (Fig. 1.2.17) [48]. These spins are considered to be the spin solitons. As these examples show, the NIDW, LR-NIDW, charge soliton, and spin soliton can take central roles in elementary excitations in the NI systems, because these unconventional excitations are low-lying in energy.

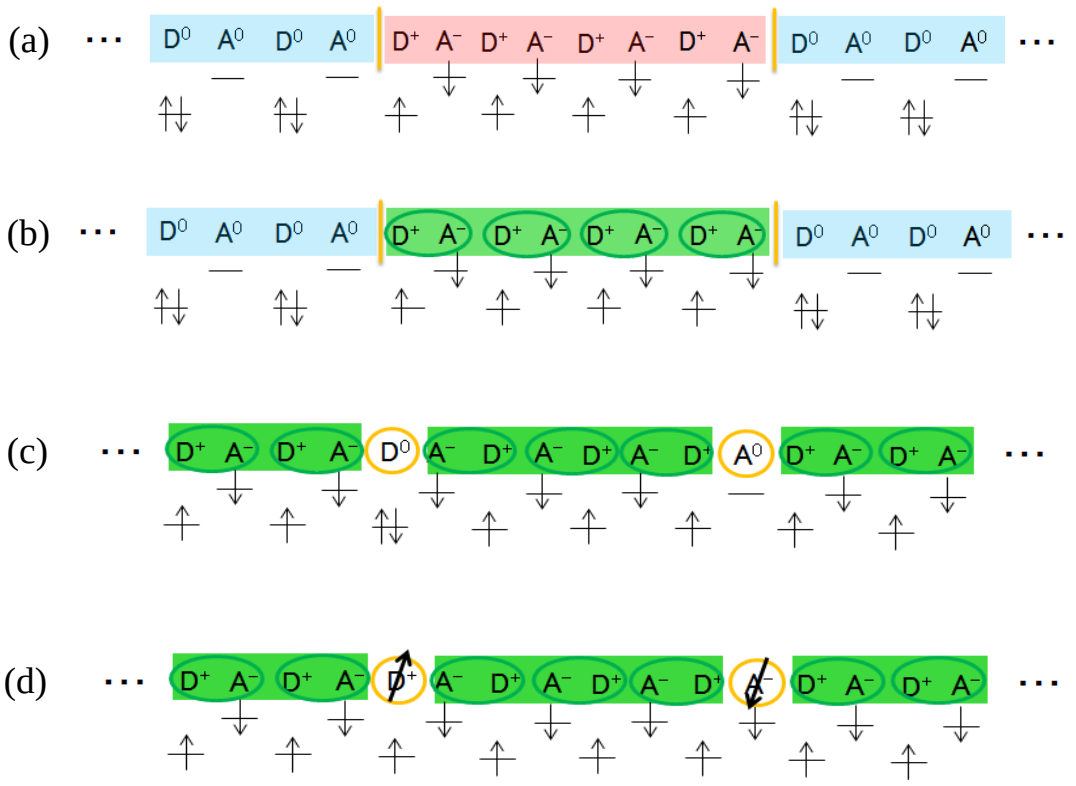


Fig. 1.2.14. Excitations in the NI system; (a) NIDWs, (b) LR-NIDWs, (c) charge solitons, and (d) the spin solitons

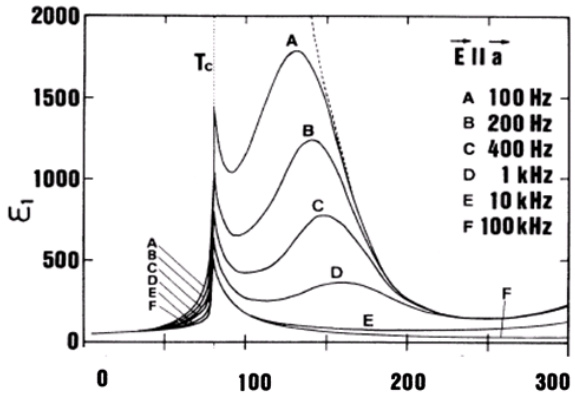


Fig. 1.2.15. Temperature dependence of dielectric constant along the **a** axis of TTF-CA at ambient pressure [46].

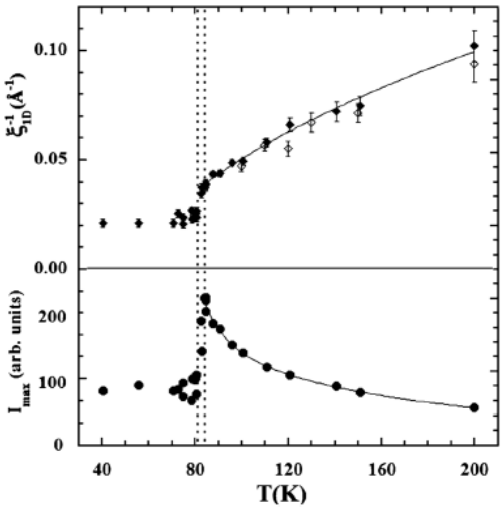


Fig. 1.2.16. Temperature dependence of inverse correlation length along **a*** axis and X-ray intensity maximum [47].

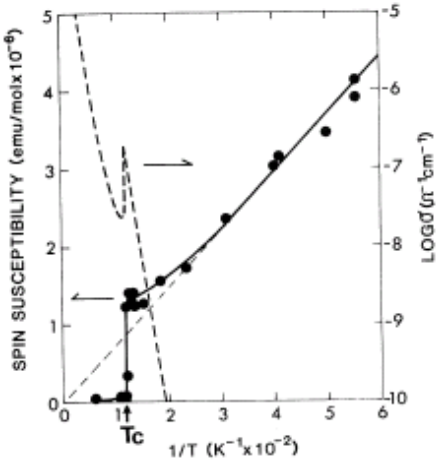


Fig. 1.2.17. Temperature dependence of spin susceptibility of TTF-CA evaluated by the ESR intensity at ambient pressure [48].

### 1.2.4 Recent progress on TTF-CA

In the previous section, the properties of TTF-CA at ambient pressure have been described. Many experiments of TTF-CA have been performed under pressures as well. Recently, new information on the NI transition under the pressures has been obtained in the NQR measurements. In this section, we review the experiments of TTF-CA under the pressures.

A previously proposed phase diagram of TTF-CA is shown in Fig. 1.2.18. It was constructed on the basis of the previous NQR, neutron scattering, vibrational spectroscopy, and electric conductivity measurements.

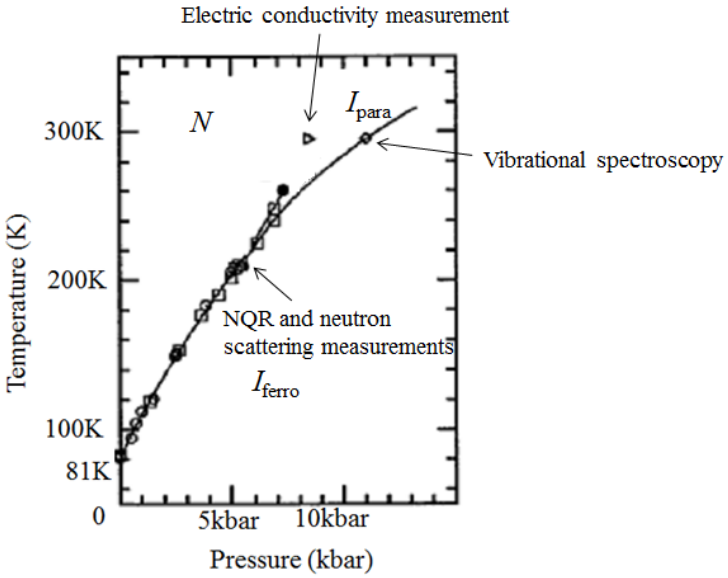


Fig. 1.2.18. Previously suggested phase diagram of TTF-CA. It is constructed by the NQR, neutron scattering, electric conductivity measurements and vibrational spectroscopy. The critical end point is suggested in the phase diagram [23].

There are three phases in the diagram; neutral phase $N$, dimerized ionic phase $I_{ferro}$, and non-dimerized ionic phase $I_{para}$. The existence of the $N$ and $I_{ferro}$, phases were confirmed by many experiments, but the $I_{para}$ phase was only suggested by the experiments described above. The $I_{ferro}$ phase has the three-dimensional ferroelectric order of ionic molecules, but the $I_{para}$ phase doesn't. The $I_{ferro}$ and $I_{para}$ phases are called the ferroelectric and the paraelectric ionic phases. With increasing pressure, the transition temperature of the dimerization rises, and concomitantly the features of the transition are changed. As shown in Figs. 1.2.19 (a), the change of lattice constants around transition temperature becomes moderate at higher pressures, indicating that the first-order nature of the transition is weakened under pressure [23]. As shown in Figs. 1.2.19 (b), the results of

the NQR measurements under pressures indicate that a precursory charge transfer occurs from above the dimerization transition temperature under pressure different from the transition at ambient pressure. According to the previous transport investigations, which is described in detail in the next section the electric conductivity against pressure at room temperature has a peak at 8.7kbar, which is located in Fig. 1.2.18 [49]. It has been suggested that the peak in the electric conductivity should be related to the charge transfer [34]. The vibrational spectroscopy measurements at room temperature under pressures show the dimerization at 11kbar as plotted in Fig. 1.2.18 [23, 50, 51]. The anomalies in the optical and transport results in Fig. 1.2.18 appear not to be coincident, differently from the transition at ambient pressure.

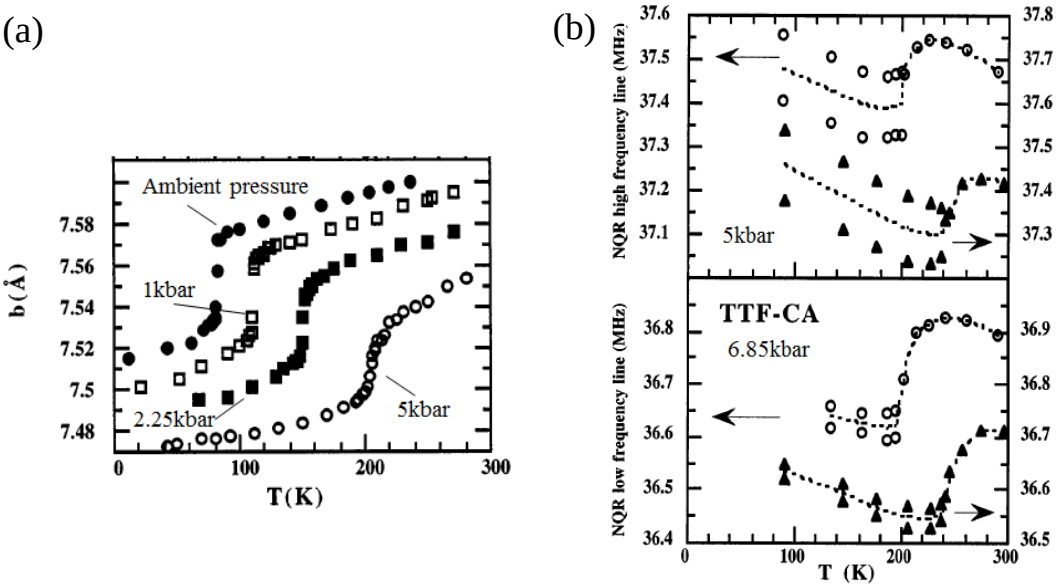


Fig. 1.2.19. (a) Temperature dependence of the **b** axis lattice constants of TTF-CA under pressure. (b) Temperature dependence of the $^{35}$Cl NQR frequency of TTF-CA under the pressure [23].

On the basis of these results, M. H. Lemée-Cailleau and T. Luty interpreted the NI transition as the gas-liquid-solid transition just like the transition of water [52]. It is well known that the *P-T* phase diagram of water has a first-order phase transition line terminated at the critical end point between the gas and liquid phases. Thus, they proposed the existence of the first-order line and critical end point between the *N* and $I_{para}$ phases (Fig. 1.2.18). According to this model, there are only a small number of $I_{ferro}$ domains in the *N* phase, and the $I_{para}$ phase contain plenty of the $I_{ferro}$ domains [53]. In the $I_{ferro}$ phase, the $I_{ferro}$ domains are condensed into the ferroelectric state. Furthermore, this idea

is theoretically implemented with the Blume-Emery-Griffiths (BEG) model that is the mean field approximation of spin-1 system [54].

Recently, NQR studies have been performed around 7~9kbar, where the existence of the first-order transition and the critical end point of the charge transfer had been proposed, and in the higher pressure region above 9kbar [17]. Figs. 1.2.20 (a) and (b) show the pressure dependence of the NQR spectra and of the NQR frequencies at room temperature, respectively [17, 25]. The red and blue lines represent the resonance frequencies of the neutral CA crystal under pressure for reference to see the purely pressure effect without charge transfer. TTF-CA exhibits neither jump nor split of the NQR spectra but the NQR frequency shifts to the ionic side as pressure is increased, which indicates that the neutral state at ambient pressure crosses over to the ionic state, but the ionic state is not the ferroelectric phase. Figs. 1.2.21 (a) and (b) show the temperature dependence of the NQR frequencies and the magnitude of the jumps of the NQR frequencies at the NI transition, respectively, for several pressures. As explained in section 1.2.3, two lines and four lines are observed in the neutral and ionic phases, respectively, only the lines in the higher frequency region are displayed in Fig. 1.2.21. The frequencies in the ferroelectric ionic phase are averaged values of split frequencies. With temperature lowered under pressure, the NQR frequency gets to deviate from the Koukoulas' rule above the dimerization transition temperature, indicating that the precursory charge transfer gradually develops in the neutral phase. In the lower pressure region, the jump of the NQR frequency is clear (*e.g.*, orange line 5kbar), but in the higher pressure region (*e.g.*, purple line 9.0kbar), that is not the case. It is noted that at 18kbar a tiny but finite jump of the frequency is observed.

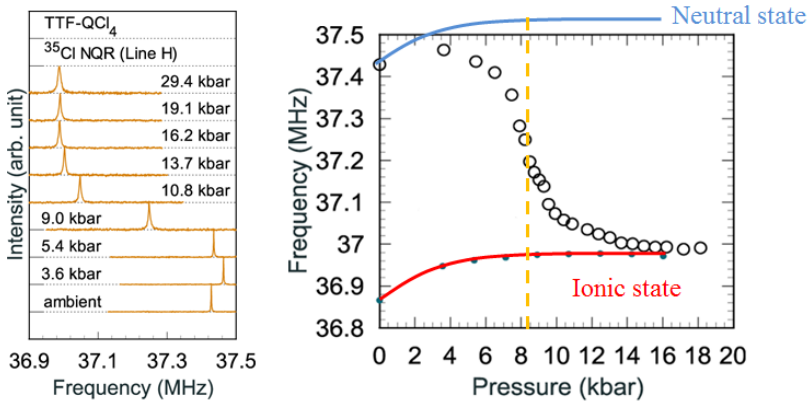


(a) (b)

Fig. 1.2.20. (a) Evolution of $^{35}$Cl NQR spectra of TTF-CA at room temperature with pressure [25]. (b) Pressure dependence of $^{35}$Cl NQR frequencies of TTF-CA and neutral CA (for reference) at room temperature [17].

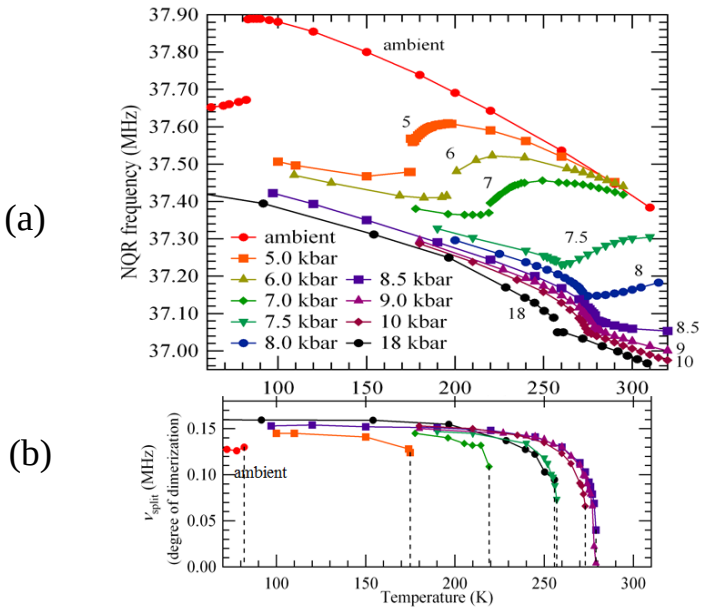


Fig. 1.2.21 [17]. (a) Temperature dependence of the NQR frequencies of TTF-CA at several pressures. Only the two frequencies (in high frequency region) are plotted here. The frequencies of two split lines in the ferroelectric ionic phase are averaged. (b) Temperature dependence of the line splitting in the ferroelectric ionic phase at several pressures.

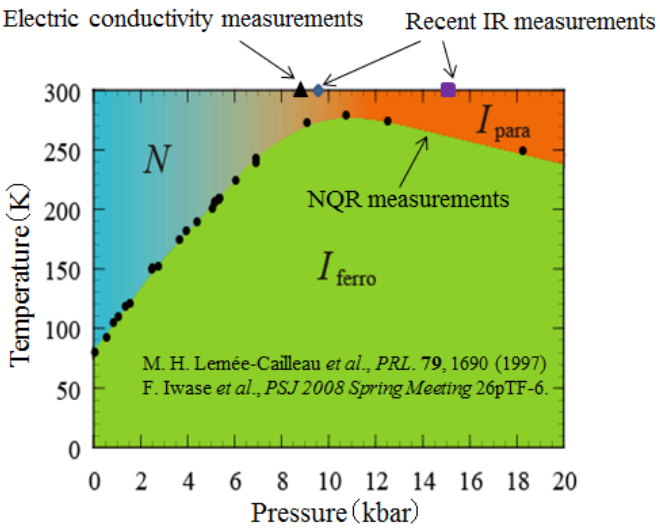


Fig. 1.2.22. Phase diagram of TTF-CA recently suggested by NQR measurements [25]. The newly proposed transition line over 8kbar was determined by the NQR measurements. Results of recent IR measurements are also plotted. The IR measurements show that the volume fractions of the *N* and *I* molecules become comparable at 9.5kbar and the dimerization occurs at 15kbar. The closed triangle indicated by the electric conductivity measurements is the identical point as in Fig. 1.2.18 [23].

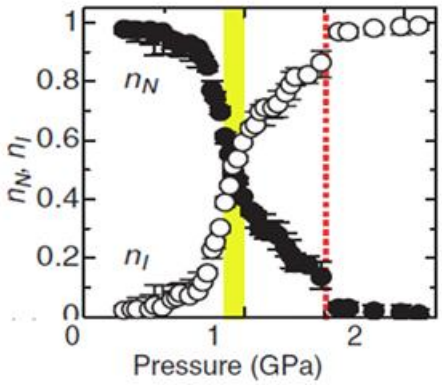


Fig. 1.2.23. Pressure dependence of the fractional ratio of the *N* and *I* molecules deduced from the .recent IR measurements [9].

These results of NQR measurements are summarized in Fig. 1.2.22, which is a new phase diagram of TTF-CA. It is different point from the conventional phase diagram that there is no critical end point of the charge transfer and the paraelectric ionic phase exists extensively in the high pressure and high temperature region (orange region in Fig. 1.2.22). In this phase diagram, recent results of IR measurements are plotted, which shjow ratio of the *N* and *I* molecules are equal at 9.5kbar and the dimerization should occur at 15kbar (Fig. 1.2.23) differently from the previously predicted dimerization point at 11kbar [48, 49].

NMR experiments also have been carried out, and Fig. 1.2.24 shows pressure dependence of spin-lattice relaxation $1/T_1$ of $^1$H-NMR of TTF-CA [55]. In the logarithmic plot $1/T_1$ is exponentially enhanced especially in the low pressure region, which can be interpreted as emergence of spins. The results of the NMR measurements support the existence of the paraelectric ionic phase under pressure. However, this result is inconsistent with the results of the vibrational spectroscopy. In the vibrational spectroscopy, the $a_g$ mode is enhanced under pressure and it indicates the ionic phase under pressure is in the dimerized state [16]. Inconsistency between the NQR and IR measurements will be discussed in Chapter 3.

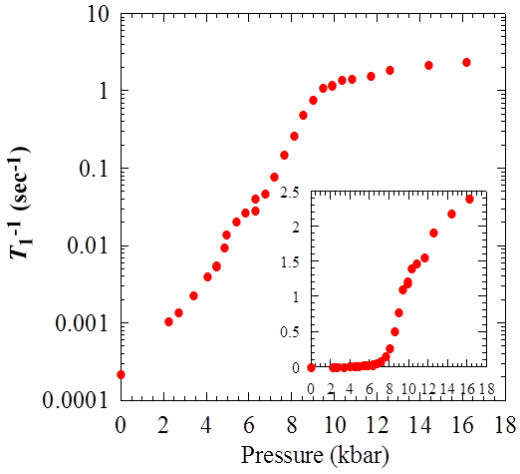


Fig. 1.2.24. Pressure dependence of spin-lattice relaxation $1/T_1$, at the $^1$H sites at room temperature [55].

### 1.2.5 Previous electric conductivity measurements of TTF-CA

A result of electric conductivity of TTF-CA at ambient pressure is shown in Fig. 1.2.25 [49]. When temperature is lowed at ambient pressure, the electric conductivity shows insulating behavior in both the *N* and the $I_{ferro}$ phases. This result corresponds to prediction that the *N* phase should be a band insulator and the *I* phase should be the Mott insulator. It is because in the *N* state all the HOMOs, which form the valence band, are filled with electrons, and in the *I* state, where one electron exists at each HOMO and LUMO, electronic state is in the Mott insulator. Rigorously the band insulator and the Mott insulator in the one-dimensional system cannot be distinguished in finite temperature, but here they are distinguished nominally. The most anomalous behavior is a jump and increase of the electric conductivity at the NI transition, because the increase of the electric conductivity, namely, behavior like metal occurs between the two insulator phases.

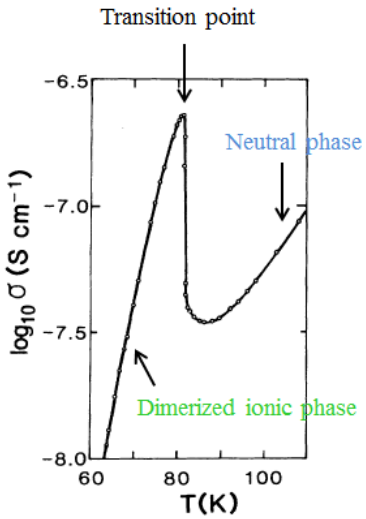


Fig. 1.2.25. Temperature dependence of the electric conductivity of TTF-CA at ambient pressure [49].

This increase can be also observed under pressures (Figs. 1.2.26 (a) and (b)) [49, 56]. The increase of the electric conductivity under the pressures is not as sharp as that at ambient pressure. This result is consistent with the results of the NQR measurements which show that the jump of the NQR resonant frequency becomes smaller with pressure increasing. Furthermore the peaks of the electric conductivity become moderate above 6kbar (Fig. 1.2.26 (b)). Thus it is difficult to determine the transition points clearly, but characteristic points, maximum values of the electric conductivity, are plotted on the phase diagram as previously described (Fig. 1.2.18 and Fig. 1.2.22).

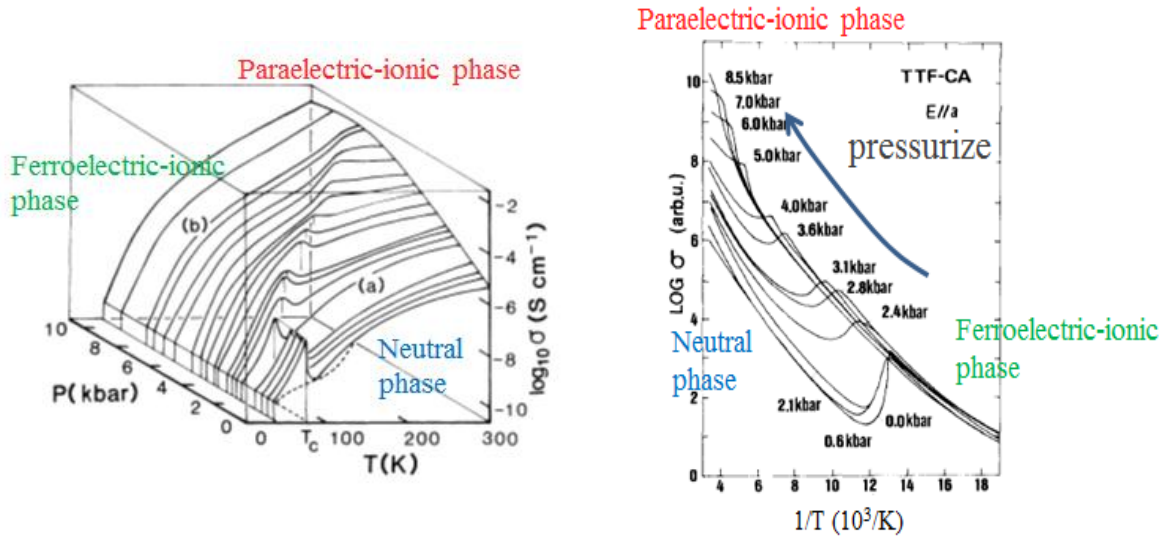


(a) (b)

Fig. 1.2.26. (a) Temperature dependence of conductivity of TTF-CA under various pressures [49]. (b) Activation plot of the conductivity of TTF-CA under the pressure [56].

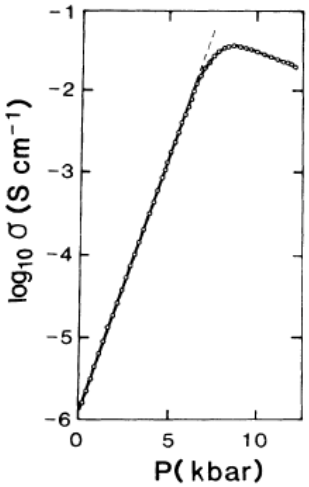


Fig. 1.2.27. Pressure dependence of the electric conductivity of TTF-CA at room temperature [49].

Absolute values of the electric conductivity are also anomalous. For the measurements are performed by two-terminal method, the absolute values has ambiguity but very helpful. Fig. 1.2.27 shows pressure dependence of the electric conductivity at room temperature. As described previously, the electric conductivity has a peak at 8.7kbar, around which the charge transfer can be observed by the NQR measurements (Fig. 1.2.21 (b)). This peak is not a sharp but rounded shaped peak, which is different from the sharp peak observed at ambient pressure. The value of the electric conductivity is changed by about 5 orders of magnitude from the ambient pressure to the rounded shaped peak. The value at the peak is about $10^{-1}$~$10^{-2}$S/cm and it's so small values as the typical insulator.

## 1.3 Motivation and Purpose

As described above, there are many unsolved problems in the NI transition materials and the new phase, the paraelectric ionic phase in TTF-CA is suggested. So, in this thesis, we aim to clarify the nature of the NI phase transition and explore novel metallic phases by means of detailed measurements of the charge transport under high-pressure conditions as follows.

(I) The recent NQR measurements have provided a new phase diagram of TTF-CA, which contain several phases with and without the coupling between the charge, spin, and lattice degrees of freedom. This suggests the emergence of diverse and exotic phased due to the interplay of these degrees of freedom and the comprehension of each constituent phase in the diagram is expected. However, the proposed phases are not fully consent with other experiments such as the IR measurements. The first purpose of the present work is to solve the seeming discrepancy and clarify the nature of the phases in TTF-CA in the light of the roles of charge, spin and lattice by investigating the charge transport in detail.

(II) It is widely recognized that TTF-CA is a good conductor around the transition or crossover of charge transfer despite that the adjacent phases are both insulators. For this region, exotic elementary excitations such as NI domain wall and solitons have occasionally been mentioned. The second purpose of this work is to clarify the elementary charge excitations in respective phases and in the vicinity of phase boundaries by the detailed four-terminal resistivity measurements. One of our focuses is whether the neutral-ionic domain walls are realistic carriers or not in TTF-CA because such kind of elementary excitations potentially open a new window to the charge physics in insulating states.

(III) There is no report on the realization of metallic states in the NI system. Considering that exotic phases and exotic excitations are being argued in this class of materials, there is no reason why we do not expect novel properties if they were metalized. As the third purpose, we tackle this issue by three different strategies; the application of extreme high pressures, compression in a particular direction and choice of a quasi-two-dimensional material.

# Chapter 2 Experiments

In the present study, electric resistivity measurements of the NI transition materials, TTF-CA and $M_2P$-$TCNQF_4$(M2P:5,10-dihydro-5,10-dimethylphenazine;TCNQF4:2,3,5,6-tetrafluoro-7,7,8,8-tetra cyanoquinodimethane), were carried out under pressure. As for $M_2P$-$TCNQF_4$, we describe its properties in Chapter 4, and thus will only give its structure in this chapter. Generally, there are two methods to measure electric resistivity, the four-terminal method and the two-terminal method. The NI transition materials had so far been measured only by the two-terminal method because of their high resistance values. In the present study, however, the four-terminal method was employed to obtain accurate electric resistances free from any contact resistance influence. The electric resistivity also probes the anisotropy of electronic states. The anisotropy of TTF-CA was characterized for the first time and gives information on the dimensionality of electrical conduction. Pressure also plays an important role in investigating the NI transition, since the pressure is a parameter to cause the transition. Two methods to apply pressure on materials, hydrostatic and uniaxial pressures, were adopted in the present study for revealing the conduction mechanism and seeking the metallic state in the NI transition materials. For the metallization, the two materials were investigated under extremely high pressures, which are generated with a cubic anvil system. In this chapter, these experimental details are described.

## 2.1 Samples

### 2.1.1 TTF-CA

The crystals of TTF-CA used in the present study were provided by Okamoto-Kida group, the University of Tokyo. To examine the anisotropy of TTF-CA, the crystallographic axes of TTF-CA were identified as follows. The crystals have cuboid-like shapes as shown in Fig. 2.1.1. In general, the **ab** plane of TTF-CA appears on the face when it is put on a flat table, and can be easily identified. The **ab** plane takes a rectangle shape because the **a** axis and the **b** axis are normal to each other, but the **c** axis is not perpendicular to the **ab** plane [28]. In many cases, the long side of the rectangular **ab** plane is parallel to the **a** axis, but it is not always the case. As another way to distinguish the **a** axis from the **b** axis, we used polarization of light reflected from the **ab** plane. When the **ab** plane is looked at through a light polarizer, if the **ab** plane looks bright the polarization direction is parallel to the **b** axis, and if the **ab** plane looks dark the direction is parallel to the **a** axis, as is expected in the reflectance spectra of TTF-CA (Fig. 2.1.2) [57]. The reflectivity against the polarized light along the **b** axis is much more enhanced in the visible light region than against the polarized light parallel to the **a** axis. Thus, the three crystallographic axes can be distinguished. For example, in the sample in Fig. 2.1.1 the horizontal direction is parallel to the **b** axis though the side length along the **b** axis is

larger than the other along the **a** axis.

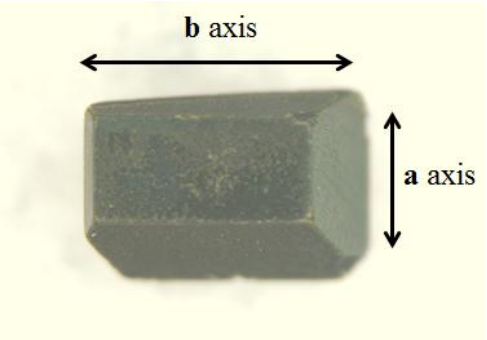


Fig. 2.1.1. Picture of TTF-CA. The assignment of the a and b axes were made, referring to the reflectance spectra.

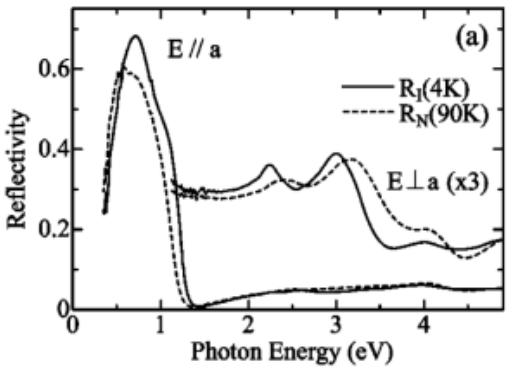


Fig. 2.1.2. Reflectance spectra of TTF-CA [57].

### 2.1.2 $M_2P$-$TCNQF_4$

$M_2P$-$TCNQF_4$ is a material which has an intermediate molecular arrangement between the mixed-stack and the segregated-stack. Fig 2.1.3 shows the schematic structure of $M_2P$-$TCNQF_4$ at ambient pressure and room temperature, where the donor molecule is $M_2P$ and the acceptor molecule is $TCNQF_4$ (its real image is shown in Fig. 2.3.3) [58, 59]. The [111] is the direction of the DA axis, where the donor and acceptor molecules are arranged alternately, and [100] is the directions of the DD/AA axis, where the same type of molecules are arranged. A point distinct from TTF-CA is that the distance between neighboring donors (neighboring accepters) is almost the same as that between the donor and acceptor molecules, making $M_2P$-$TCNQF_4$ an intermediate material between the mixed-stack and segregated stack systems. Because the crystal axes cannot be distinguished only from the appearance of the sample and the directional distinction of polarized light reflection differently from TTF-CA, we measured the reflectance spectra in Okamoto-Kida group to assign the axes, since the reflectivity spectra of the DA axis and the DD/AA axis are different (Fig. 2.1.4) [58]. As shown in Fig. 2.1.4, the reflectivity spectrum for the light polarized along the DD/AA axis shows a peak at 0.72eV, while that for the polarized light along the DA axis shows at 0.9eV.

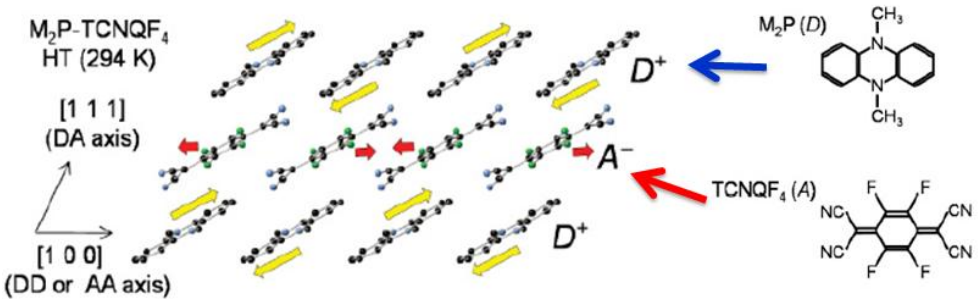


Fig. 2.1.3. Left: Schematic structure of $M_2P$-$TCNQF_4$ at ambient pressure and room temperature. Right: A donor molecule $M_2P$ and an acceptor molecule $TCNQF_4$ [59].

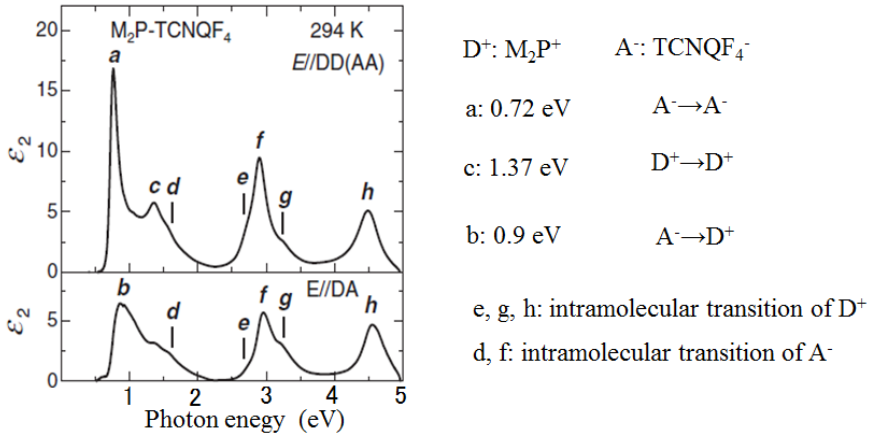


Fig. 2.1.4. Reflectance spectra of $M_2P$-$TCNQF_4$ for polarized light along the DD/AA axis and DA axis [58].

The reflectance spectra were measured with the microspectrophotometer MSV370, which. changes an optical source, a spectroscope, a detector, and a filter automatically depending on the wavelength in the region of 250~2500nm. The measurements were performed in a range of 800~2500nm. Polarization of light was fixed, and sample was rotated against the polarization direction of light. By comparing the experimentally obtained spectra with Fig. 2.1.4, the axes were assigned.

## 2.2 Electric resistivity measurements

### 2.2.1 Four-terminal method and two-terminal method

Electric resistance measured by the two-terminal method always includes the so-called contact resistance between a sample and a terminal (Fig. 2.2.1 (a)), and thus it is not a real sample resistance. The four-terminal method, in contrast, can avoid this problem. In this method, four terminals attached to the surfaces of a sample have roles as current and voltage terminals. The two terminals on the edge of the sample are used for the current injection and are connected to a current source. The other two terminals in the middle of the sample are used for the voltage sensing and are connected to a voltmeter.

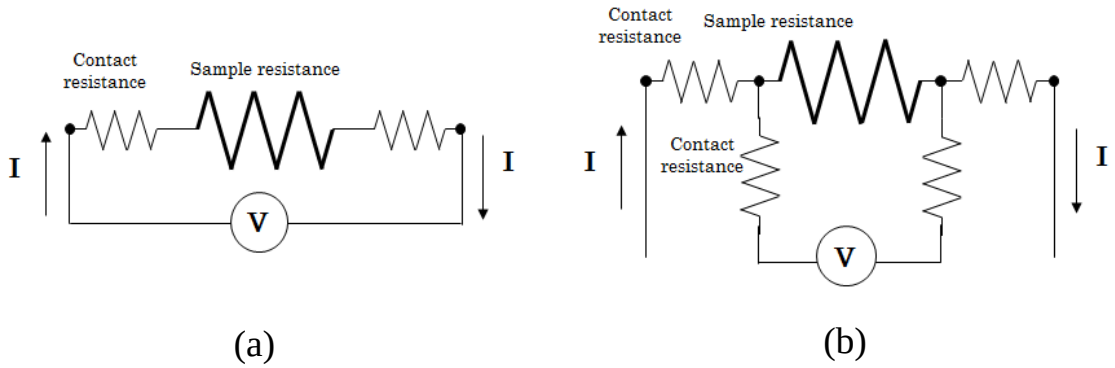


Fig. 2.2.1. (a) and (b) are schematic sample and contact resistance in circuit diagrams of the two-terminal and four-terminal methods, respectively.

A circuit diagram of the four-terminal method is shown in Fig. 2.2.1 (b). In the four-terminal method, current flows between the two current terminals through the sample, and voltage drop between the two voltage terminals are measured. In this way, the contact resistances at the current terminals have no influence to the voltage drop. The voltmeter has so large internal impedance that almost no current flows through the two voltage terminals, leading to no influence of their contact resistances to the voltage sensing. In the present experiments, the current was reversed in order to cancel out the thermoelectric power that arises in the sample.

In the present experiments, a contact resistance of TTF-CA is one order higher than that by four-terminal method, as explained in Chapter 3: at ambient pressure and temperature, the two-terminal method gives several MΩ, and the four-terminal method gives several hundred kΩ. Furthermore, TTF-CA shows insulating behavior at ambient pressure, and thus we cannot use four-terminal method at ambient pressure. However, resistance of TTF-CA is decreased drastically against pressure variation, and we can use the four-terminal methods above 3.7kbar.

Finally, another caution for using the four-terminal method is noted. We occasionally had difficulty in measuring the sample resistance over the order of mega ohms, in spite of the resistance sufficiently lower than the internal impedance. This is probably because of the capacitances inevitably introduced in the circuit. A measure which we took in such a case is explained in the section 2.2.5.

### 2.2.2 Attachment of terminals

Carbon paste is used as an adhesive to attach the terminals. First, some amount of the carbon paste was dissolved to a certain amount of diethyl succinate. We took care of viscosity of the mixed paste because if the paste has too high or low viscosity, the terminals come off from the sample in the process of applying pressure or lowering temperature. Next, gold wires of 0.5~1.0 mm in length and 25 μm in diameter for electrical leads were attached to the surface of the sample with the carbon paste mixed with the diethyl succinate. We attached the current terminals to the side of the sample with so sufficient amount of the paste that the paste covers the whole side to make electric fields applied homogeneously. In contrast, the voltage terminals were attached by a small amount of paste because, if the paste spreads too widely, the distance for the voltage drop is not well defined and the current flow in the spread paste parallel to the sample surface leads to the contamination of the resistance of the paste to observed ones. In addition, the voltage contacts were taken around the middle position between the two current terminals. It is because the electric field is expected to be most uniform there. In the final step, only the diethyl succinate was vaporized. It took a day for the carbon paste to dry.

### 2.2.3 Instruments used for electric resistance measurements

The used sourcemeter is Keithley 2400, nanovoltmeter is Keithley 2182A, and picoanmeter is Keithley 6487. The configurations of the circuits of the two- and the four-terminal methods are shown in Figs. 2.2.2 (a) and (b). The connection diagram of the picoanmeter is shown in Fig. 2.2.3. We used Lake Shore 340 for reading the sample temperature, connecting to Cernox thermometer, whose resistance is converted to temperature. The Cernox thermometer was attached to a pressure cell so that the sample temperature can be detected. All these instruments were connected with GPIB cables.

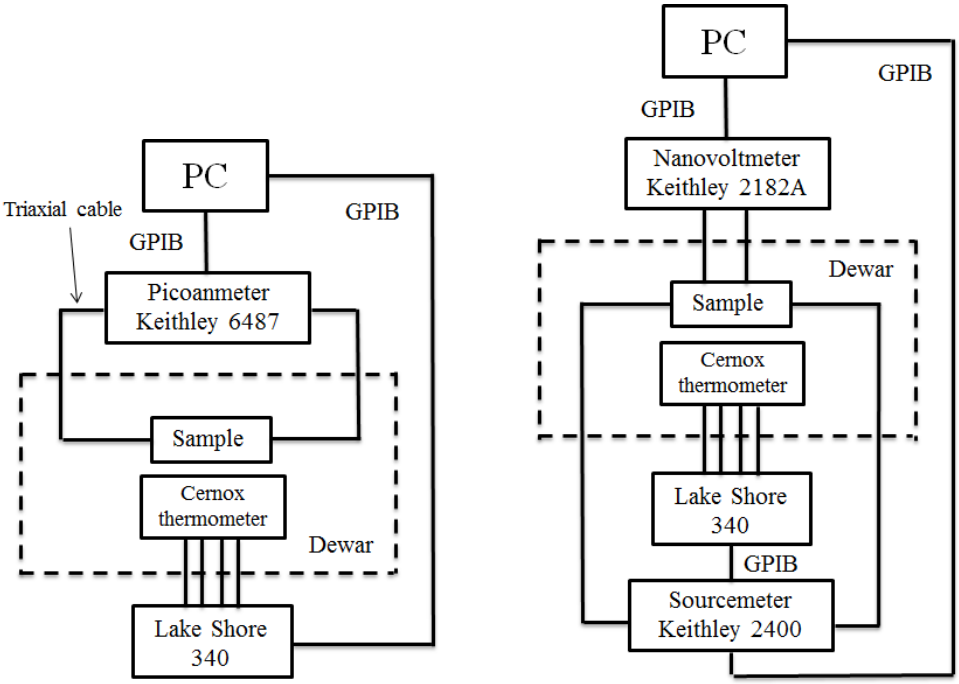


(a) (b)

Fig. 2.2.2. (a) and (b) are circuit diagrams of the two-terminal and four-terminal methods, respectively.

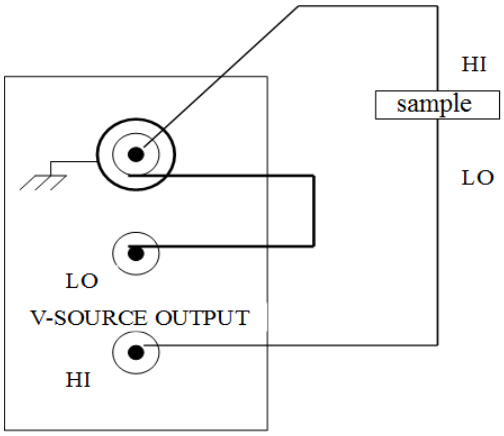


Fig. 2.2.3. Connection diagram of the picoanmeter.

### 2.2.4 Method of variable temperature

A probe was inserted in a Dewar which has a temperature control system. Temperature was varied automatically, using a temperature controller, or manually.

The automatic temperature control is attained with the use of a variable temperature-insert (VTI), where helium extracted from the helium bath is heated to maintain the temperature.

In the manual temperature control system, we equipped the probe with Dewar which has double thermal insulation. The Dewar was inserted into a helium Bessel by hand. We controlled position of the Dewar from a liquid helium level. Sometimes we putted helium gas into inner thermal insulation space as a exchange gas. Additionally, we used Manganin wire as a heater, which was wound onto a pressure cell. We mounted the thermometer on the pressure cell. We monitored and controlled sample temperature by Lake Shore 340.

We took the cooling (warming) rate of 0.1 ~ 0.3 K/min, since we avoid the thermal clack of sample and the generation of temperature difference between thermometer and sample space.

### 2.2.5 High resistance measurements

It is well known that capacitance component between terminals, cables, and connectors, so called shunt capacitor, gives resistivity measurement serious effect. Because the time constant to read voltage is decided by RC, where the R is resistance of sample and C is shunt capacitance (Fig.2.2.4), it takes long time to obtain true voltage value. Resistance of TTF-AC reaches sometimes mega ohm over.

To measure such a high resistance, we used a function called HOLD equipped on the nanovoltmeter (KEITHLEY 2182A) [60]. The HOLD option is a method to judge if the obtained voltage is the reliable value or not. So, we used this voltage value to obtain the resistance.

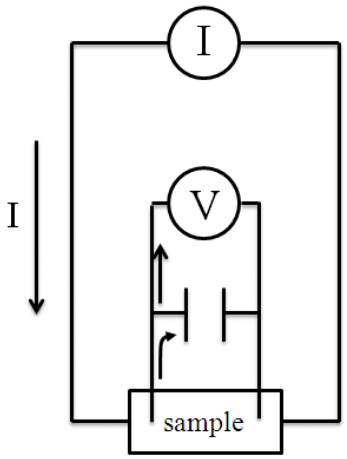


Fig. 2.2.4. Schematic capacitance which comes into the circuit in parallel with the sample.

## 2.3 Method of applying pressure

### 2.3.1 A pressure cell

In order to apply pressure, we used a clamp type pressure cell. Fig. 2.3.1 shows a cross-section view of pressure cell. We used a dual structure type cell made from BeCu alloy and a NiCrAl alloy.

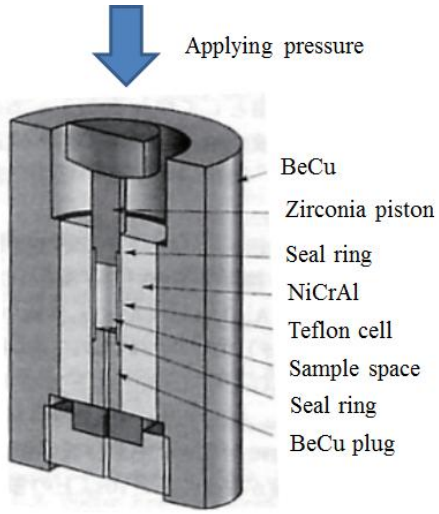


Fig. 2.3.1. schematic pressure cell.

We take two different sample space cells. One is φ5.5mm and the other is φ4.0mm hole sizes. The φ4.0mm type cell is shown in Fig. 2.3.2 (a). It is experimentally known that available maximum pressure decreases with larger space cell. The φ5.5mm and φ4.0mm sample space cells are used below 20kbar and 40kbar, respectively. Figs. 2.3.2 (a) ~ (d) show process of building a pressure cell. A plug, a seal ring, a piston, a sheet of copper foil, and a piston backup are put in the cylinder in this order. The seal ring, the piston and the piston backup are made from zirconia (ceramics). Only φ4.0mm piston is composed of two parts for preventing from breaking at high pressure. The copper foil, which is put between the piston and the piston backup, prevents corrupting then due to direct contact between hard materials.

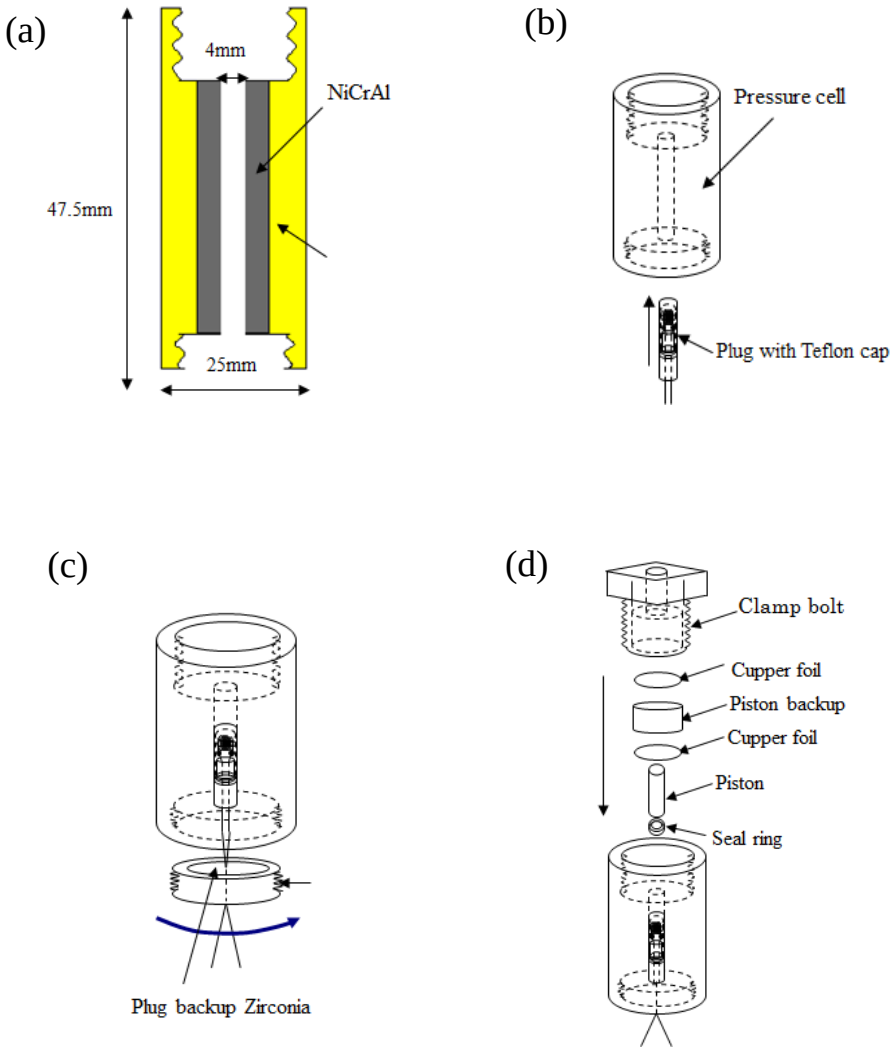


Fig. 2.3.2. (a) ~ (b) Process of building a pressure cell.

### 2.3.2 Setting the sample on the plug

We used a copper wire with a polyurethane coat as a lead. This wire has diameter of 0.13mm (including thickness of coating). Four lead wires were passed through the hole with diameter of 0.6mm of plug. We made two twisted pair wires for reducing noise. To fill in the hole and to fix the wires, epoxy encapsulant**,** stycast 1266, is used. Before solidification, to purge the air from stycast, we evacuate it by a vacuum pump, and after that, it was poured into the hole of the plug. We wiped off the stycast at the bottom of the plug until hardening, because extra solidified stycast may wrench off the lead wires under pressure. Before the stycast was solidified completely, we set the basal plate (Fig. 2.3.3), which is made by cutting a rectangle with the size about 2mm×5mm from flexible cable. We connect the copper twisted pair and the gold wire attached on sample using the terminal of basal plate by soldering (right panel of Fig. 2.3.3). Because of difference of heat contraction between a sample and plate, when a sample adheres to a plate, it sometimes has cracks at low temperature. So, we set the sample away from the plate. Additionally, we also made the gold wires from the basal plate loose, because the cracks may happen in the sample because of the tension due to a thermal contraction of the gold wires. Left panel in Fig. 2.3.3 shows the real image of $M_2P$-$TCNQF_4$ where the four terminals are attached.

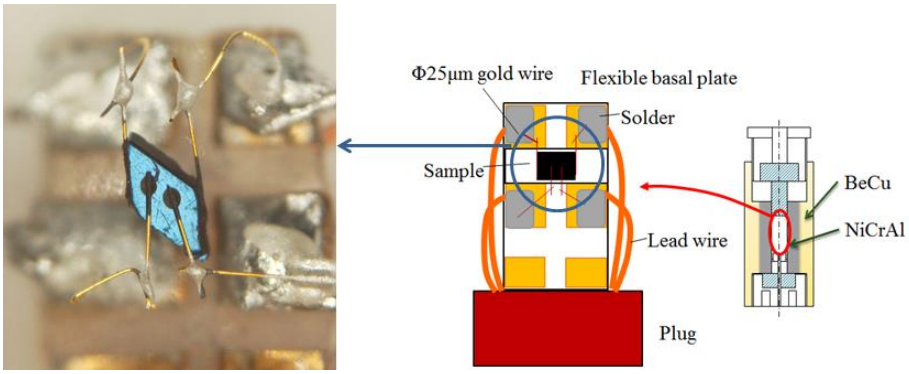


Fig. 2.3.3. Left: Real sample of $M_2P$-$TCNQF_4$ where the four terminals are attached.
Right: Schematic sample setting on the basal plate.

### 2.3.3 Applying pressure

There are two pressurizing methods used in this study: one is hydrostatic pressure and the other is uniaxial strain.

Hydrostatic pressure: Two kinds of oil as a pressure medium were used, Daphne 7373 and Daphne 7474, whose solidification pressure at room temperature are 22kbar and 37kbar, respectively [61]. We used Daphne 7474 for measurements above 10kbar, since a large hysteresis of temperature dependence of resistivity of TTF-CA around solidification (or melting) temperature of oil was observed. We did not observe this hysteresis in same pressure region in case of Daphne 7373. We confirm that there is no difference in resistivity between Daphne 7373 and 7474 cases above 15kbar. Before assembling the plug with a Teflon cap, air which was solved in oil was purged by a pumping. The plug with the Teflon cap was put into the piston cylinder, and the pressure cell was built in the way described in the previous section.

The cell was putted on pressure apply system The piston of the pressure cell is pressed by the machine as shown in Fig. 2.3.4.

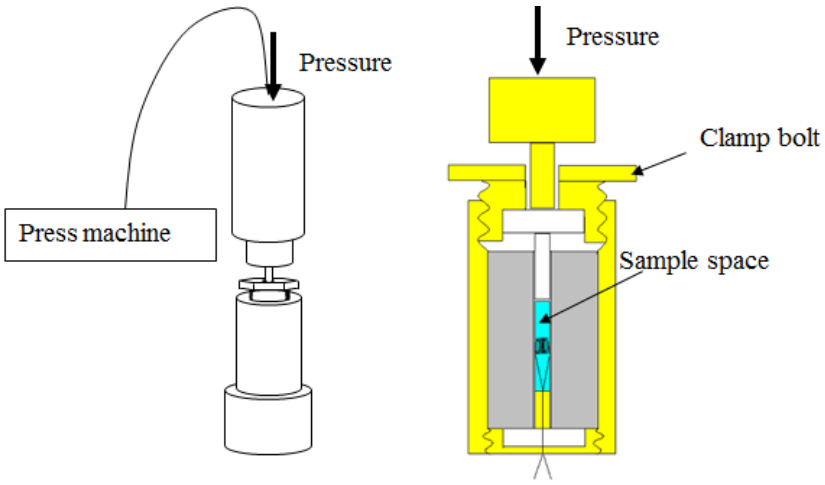


Fig. 2.3.4. Illustration of the way of applying pressure

Value of pressure was monitored by a pressure gage, which indicates the external pressure (not a sample space pressure). So, we obtained the sample space pressure to use conversion coefficient of 0.9, (that is sample space pressure = 0.9 × external pressure). When we need to know more accurate value of pressure, we set Manganin wire at sample space and measured its resistance by the four-terminal method. It is well kwon that the resistance of Manganin increases at a rate of 0.23%/ kbar.

Uniaxial strain: It is almost the same way as the hydrostatic pressure method except for a pressure medium. We used the stycast 1266 as a pressure medium instead of the Daphne oil. The two types of liquid A and B were mixed to solidification of stycast, and this liquid and a sample were put in the Teflon cap before the solidification. After that, the pressure cell was pressed and clamped at 1kbar immediately. It had been kept for more than three days until completely solidification of the stycast. After solidification process, we loosed the clamp bolt and release pressure to 0kbar, and we apply uniaxial strain to sample. While the uniaxial strain is different from hydrostatic pressure in a quality manner, we used same conversion value of 0.9 from the external pressure to the inner value. By using the same conversion, we compare the resistivity data under the hydrostatic pressure with the uniaxial strain data.

### 2.3.4 High pressure measurements

Extremely high pressure measurements over 40kbar were carried out by a cubic anvil pressure system in Uwatoko group of ISSP.

In the cubic anvil measurements, a gasket, which is a cube with 6mm side length and is made from pyrophyllite, was used. A Teflon cylinder whose internal diameter is 1.5mm was set in the gasket, and the sample was put in the Teflon cylinder. In this measurement, sample terminals were attached by Dr. Taniguchi in Saitama University. In Fig. 2.3.5, the real image of TTF-CA and pictures of the gasket are shown [62].

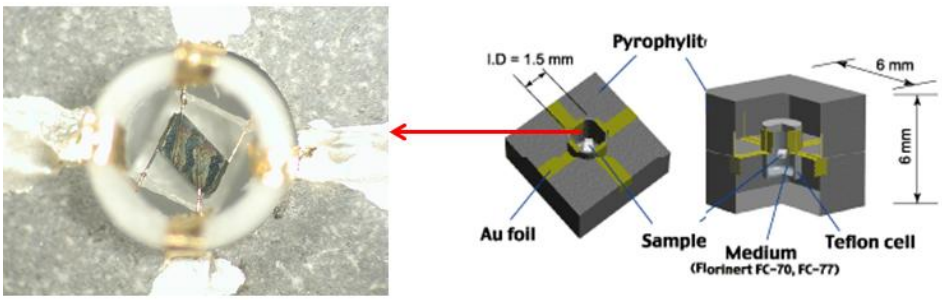


Fig. 2.3.5. Left: Real image of TTF-CA where the four terminals are attached. Right: Schematic gasket [62].

Fluorinert was chosen as pressure medium and it filled the Teflon cylinder. After assembling the gasket, it was set on the stage, around which there were six anvils made from tungsten carbide. These gasket and anvils were put into a cryostat, which was cooled by flowing liquid nitrogen and helium. A thermometer was attached to the anvils.

First, the pressure was applied to the sample at room temperature. After reaching a target pressure, the resistivity measurement was started with temperature decreasing.

# Chapter 3 Mechanisms of electric conduction and phase transition of TTF-CA

As described in Chapter 1, the NQR measurements indicated the existence of the non-dimerized ionic phase; however, the IR measurements in the same pressure region point to the presence of the dimerized ionic phase. This inconsistency is attributable to the difference in the time scale between those experiments. To address this issue from the transport measurements, Section 3.1 deals with the *P-T* phase diagram of TTF-CA determined by the dc electric conductivity measurements, whose time scale is totally different from those of the NQR and IR measurements. In Section 3.2, we argue the mechanism of the electric conduction in TTF-CA especially in the light of the possibility of the NIDW excitations as charge carriers. In section 3.3, the charge transfer, which is observed between the neutral and the paraelectric ionic phases, is examined by using the scaling analysis of the electric conductivity against pressure variation. The results suggest a NI phase diagram different from the conventional one envisioned on the basis of the BEG model [52-54]. Section 3.4 revisits the conduction mechanism, which is discussed in terms of the NIDW and the LR-NIDW excitations on the basis of the scaling analysis and other relevant measurements. Section 3.5 summarizes this chapter.

## 3.1 Phase diagram

### 3.1.1 Results

First, we show the pressure dependence of electric resistivity of TTF-CA at room temperature in Fig. 3.1.1, which was measured under descending pressure. The resistivity exhibits a minimum at approximately 8.8kbar. The decrease of the resistivity for pressures up to 8.8kbar is nearly exponential, but above 20kbar the resistivity is almost insensitive to pressure. The previously reported pressure dependence of the conductivity is shown in Fig. 3.1.2 (a), which corresponds to the data of Fig. 1.27 [49]. The present results (Fig. 3.1.2 (b)) reproduce the features of the previous results, except for the absolute values; the present values are two orders of magnitude smaller than the previous data obtained by the two-terminal method, indicating that the contact resistance inevitably incorporated by the two-terminal method does not affect the present four-terminal measurements.

The temperature dependence of electric resistivity of TTF-CA along the **a** axis under pressures is shown in Figs. 3.1.3 (a) ~ (c). The measurements were performed for three samples of TTF-CA to examine the sample dependence. We used Daphne 7373 and 7474 oils as pressure-transmitting media, and confirmed that the results at least around 15kbar were not dependent on the kind of the

oils.

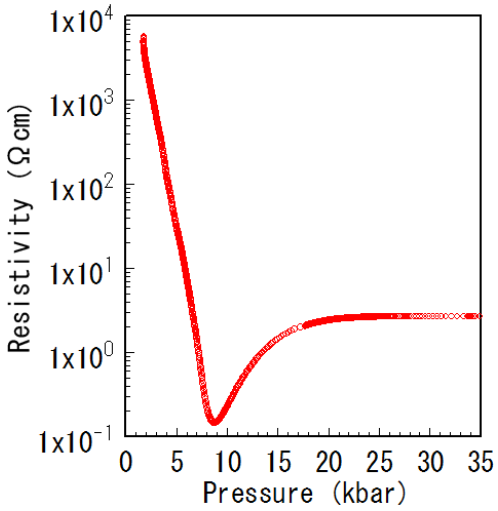


Fig. 3.1.1. Pressure dependence of electric resistivity of TTF-CA at room temperature.

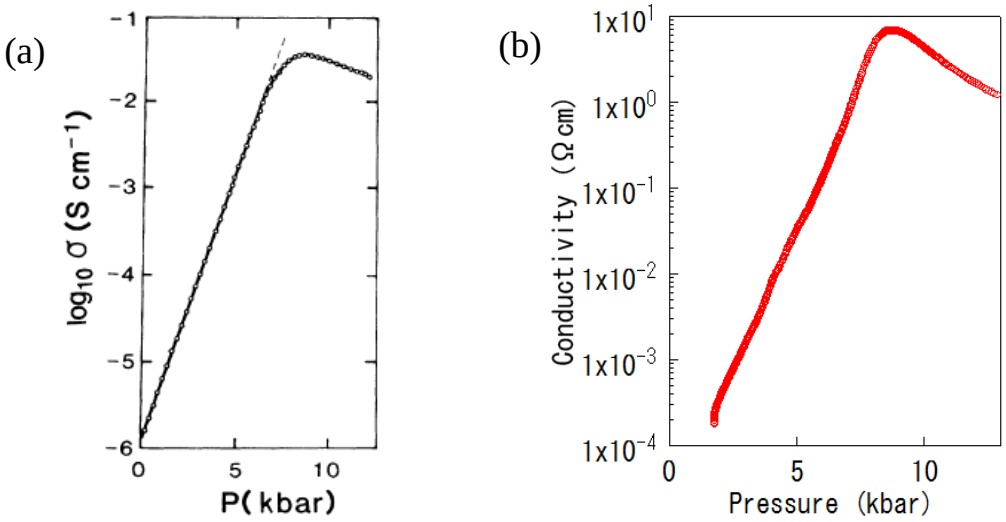


Fig. 3.1.2. Pressure dependence of electrical conductivity of TTF-CA; (a) the previous results (the same data as in Fig. 1.27) by two-terminal measurements [49]. (b) the present results (the same data as in Fig.3.1.1 ) by four-terminal measurements.

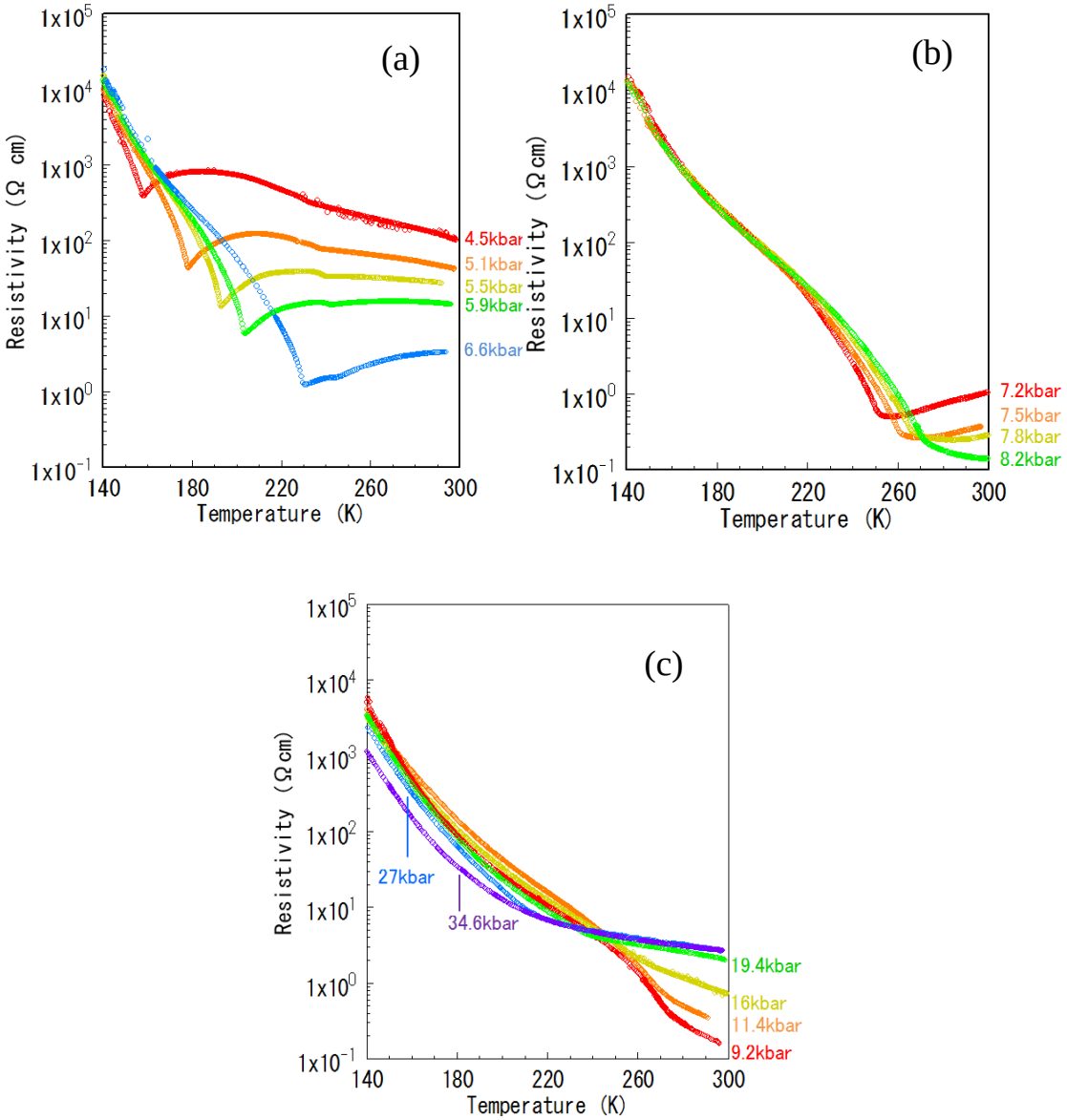


Fig. 3.1.3 Temperature dependence of electric resistivity of TTF-CA under pressures of (a) 4.5~6.6kbar, (b) 7.2~8.2kbar and (c) 9.2~34.6kbar.

The temperature and pressure profiles of resistivity suggest that there are three characteristic pressure regions: region I (4.5~6.6kbar), region II (7.2~8.2kbar) and region III (above 9.2kbar) (see Fig. 3.1.3). The resistivity around the ambient pressure is too high to be measured at low temperatures by the four-terminal method. By pressure, however, the resistivity is decreased drastically and, above 3kbar, falls into a range of measurable values. In region I, the resistivity increases with decreasing temperature but show a kink structure. Before giving the kink, the resistivity shows a turnabout to decrease and this temperature region of the resistivity decrease becomes more extended as applied pressure is higher. Below the kink temperature, the resistivity increases steeply, indicating that a large charge gap opens. The resistivity in the pressure region II (7.2~8.2kbar in Fig. 3.1.3 (b)) also takes a minimum but without a sharp kink, and the magnitude of the resistivity yields 0.1~1Ωcm, which are comparable to those of conventional organic conductors. At low temperatures, however, the resistivity increases up to the same range of values as in region I. In the pressure region III (above 9.2kbar in Fig. 3.1.3 (c)), the resistivity has no minimum but is monotonously increased with temperature decreased. At high temperatures, the absolute value of the resistivity increases with applying pressure on the contrary to the regions II and III. At low temperatures, however, the resistivity takes similar values for all pressures.

In Fig. 3.1.4, the present results are compared with the previous measurements performed by the two-terminal method. The previous data are reproduced in Fig. 3.1.4 (a), which is the same as Fig. 1.26 (b) [56]. The present resistivity data are converted to the conductivity in Fig. 3.1.4 (b), which corresponds to the white area in Fig. 3.1.4 (a). Overall, our results are similar to the previous results, but the close examination of the data finds two distinguishable features. One is the shape of the peak in the pressure region I; the peaks in Fig. 3.1.4 (b) are sharper than those in Fig. 3.1.4 (a). The other is that the rounded peaks observed in 7~8kbar in the present study as shown in Fig. 3.1.4 (b) were not clearly observed in Fig. 3.1.4 (a). Fig. 3.1.5 compares two data sets of the electric resistivity measured by two- and four-terminal methods simultaneously for an identical crystal at 5.2kbar. The absolute values of the resistivity are several times different between the two- and four-terminal methods, as expected. Moreover, the resistivity minimum around 185K is sharper in the four-terminal measurements than in the two-terminal one. These differences between the two- and four-terminal methods imply that the two-terminal resistivity contains spurious contributions such as the contact resistance in the same way as the case of the pressure dependence of the resistivity.

(a)

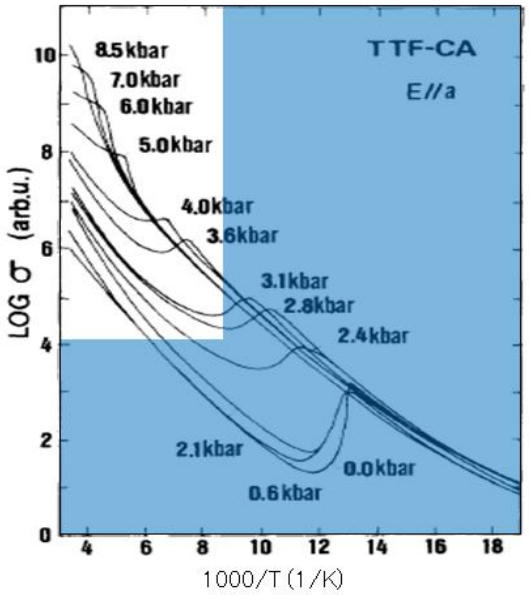


(b)

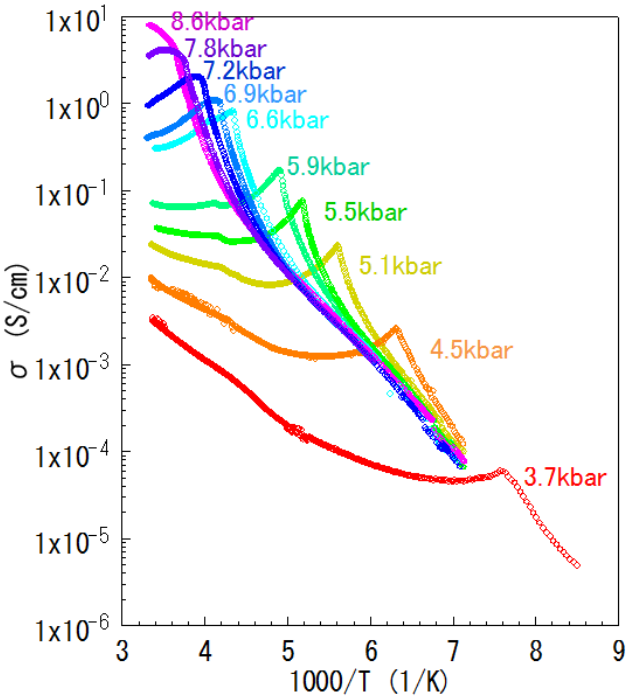


Fig. 3.1.4. Activation plot of the electric resistivity of TTF-CA; (a) the previous results (the same as Fig. 1.26 (b)) [56]; (b) the present results. The white region in (a) corresponds to the whole region of (b).

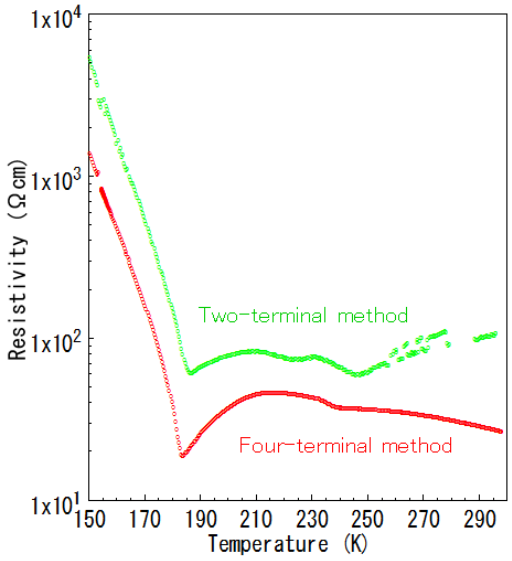


Fig. 3.1.5. Comparison of the resistivity data obtained by the two- and four-terminal methods.

Next, we focus on the behavior of the resistivity minimum in the pressure regions I (4.5~6.6kbar) and II (7.2~8.2kbar). As described above, the resistivity minima occur in a form of sharp kink in region I, and the sharpness becomes moderate in region II. To define the characteristic temperature of resistivity anomaly, we differentiate $ln\sigma$ with respect to $1/T$, that is, $d(ln\sigma)/d(1/T)$, where $\sigma$ and $T$ are electric conductivity and temperature. The resistivity and $d(ln\sigma)/d(1/T)$ are plotted against $T$ in Fig. 3.1.6 (a)~3.1.9 (b). As seen in Figs. 3.1.6 (a) and (b), jumps occur in the resistivity and $d(ln\sigma)/d(1/T)$ coincidentally at 265K, giving a good reason for defining the characteristic temperature in regions I and II. In region III, however, it is not straightforward to seek for the characteristic temperature in the temperature dependence of the resistivity; nevertheless, $d(ln\sigma)/d(1/T)$ exhibits anomalies at well-defined temperatures as seen in Fig. 3.1.7 ~ Fig. 3.1.9.

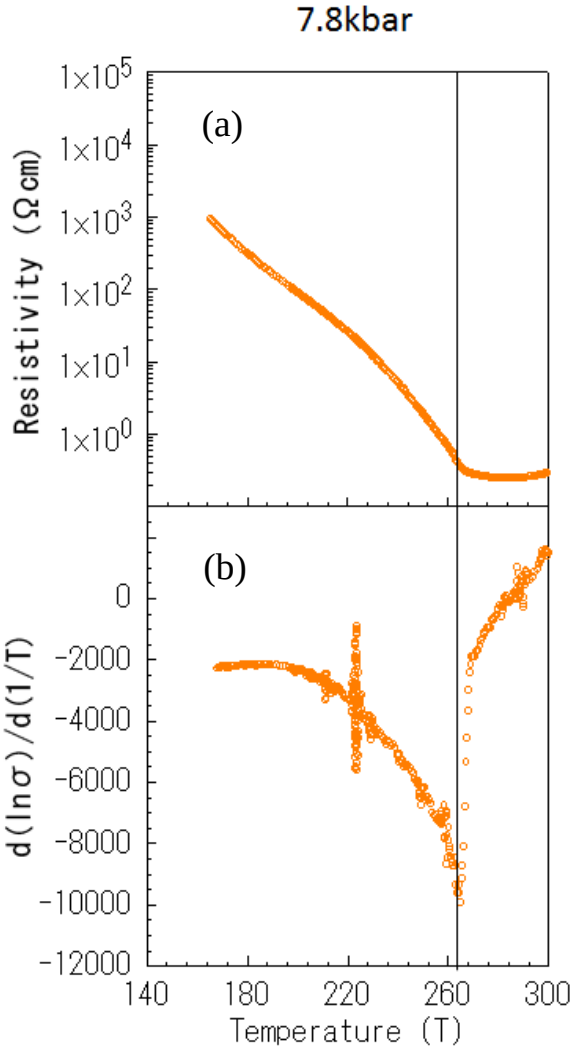


Fig. 3.1.6 Temperature dependences of (a) resistivity and (b) 1/*T*-derivative of logarithmic conductivity, d(*lnσ*)/d(1/*T*) at 7.8kbar.

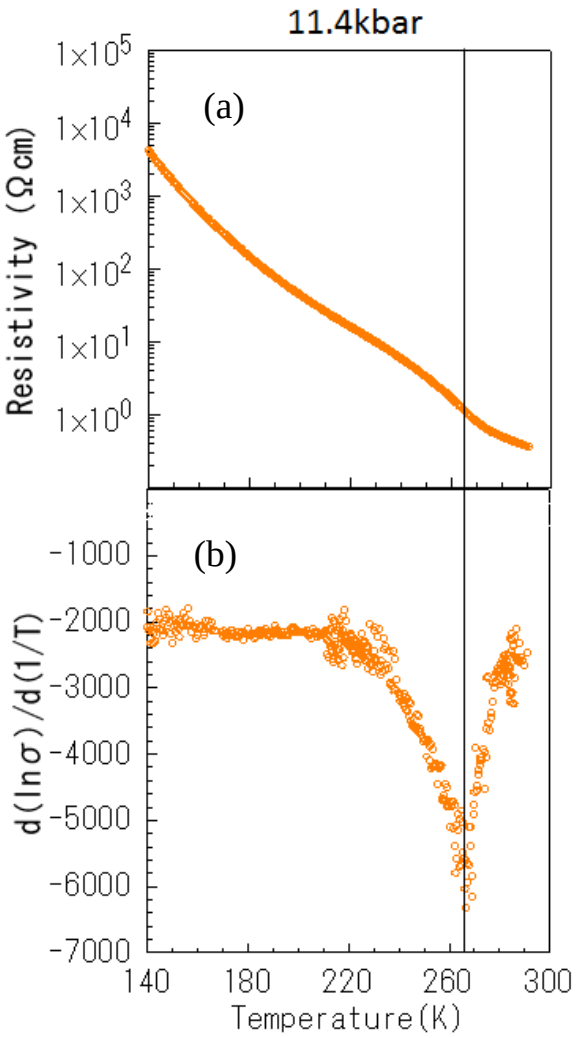


Fig. 3.1.7 Temperature dependences of (a) resistivity and (b) 1/*T*-derivative of logarithmic conductivity, d(*lnσ*)/d(1/*T*) at 11.4kbar.

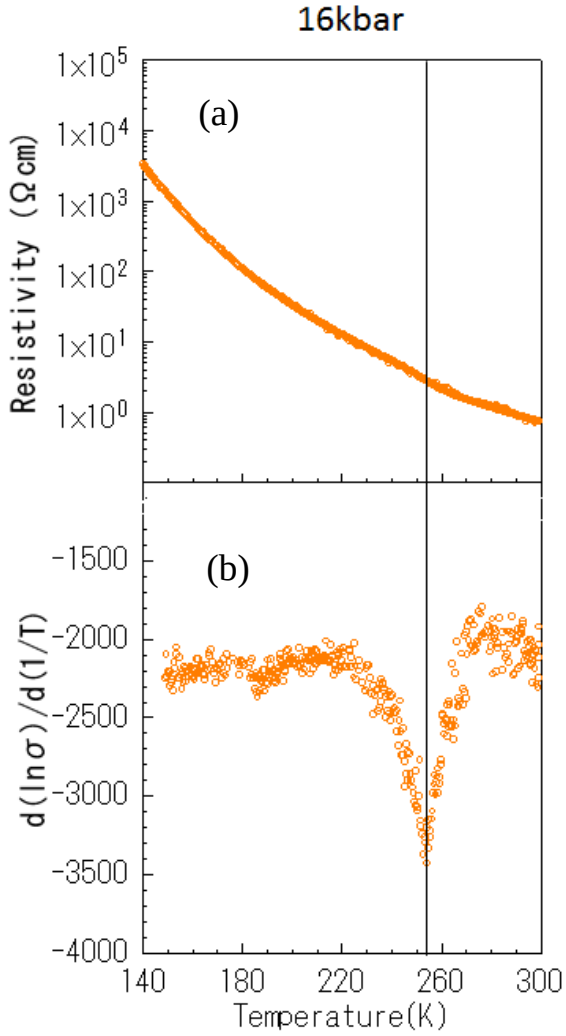


Fig. 3.1.8 Temperature dependences of (a) resistivity and (b) 1/*T*-derivative of logarithmic conductivity, d(*lnσ*)/d(1/*T*) at 16kbar.

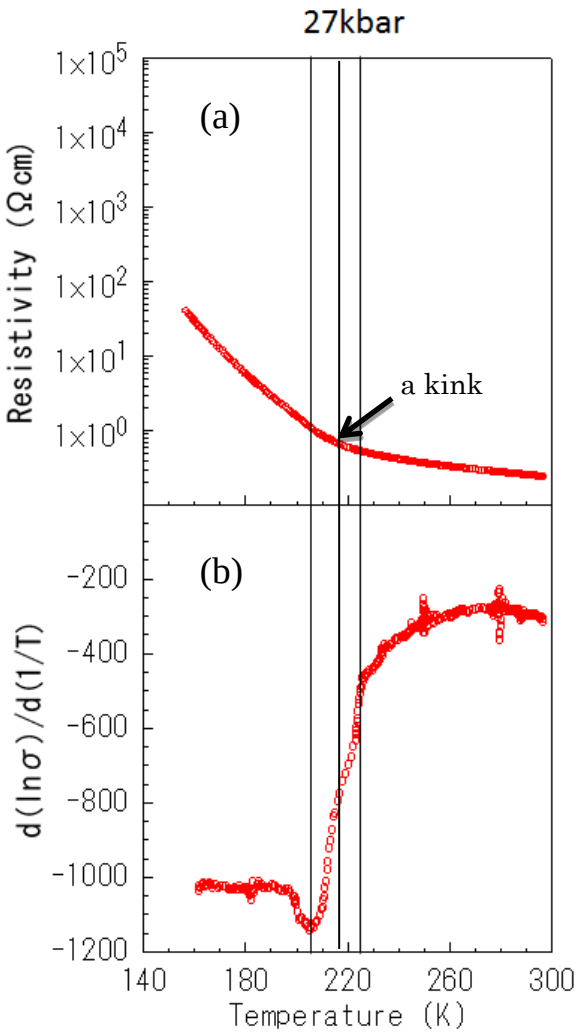


Fig. 3.1.9 Temperature dependences of (a) resistivity and (b) 1/*T*-derivative of logarithmic conductivity, d(*lnσ*)/d(1/*T*) at 27kbar.

Therefore we define temperatures giving the sharp peaks in the derivatives as characteristic points. The peaks appear without jumps, differently from the results for 7.8kbar. At 27kbar, d($ln\sigma$)/d(1/$T$) has further different temperature dependence, as shown in Fig. 3.1.9 (b). When the temperature is lowered, d($ln\sigma$)/d(1/$T$) begins to show an appreciable change at 225K and completes the change at 205K, ending up with a small dip. However, if d($ln\sigma$)/d(1/$T$) in Fig. 3.1.9 (b) is compared with the resistivity in Fig. 3.1.9 (a), a broad but appreciable kink can be identified between 205K and 225K, neither at 205K nor 225K in Fig. 3.1.9 (a). Thus, we consider that 205K and 225K may not be necessarily the characteristic temperatures. Instead, the d($ln\sigma$)/d(1/$T$) in Fig. 3.1.9 (b) appears to show that a change in the activation gap occurs in a range of 205 K-225 K. Actually, the activation plot of the resistivity at 27kbar as shown in Fig. 3.1.10 shows a clear break in linearity around 216 K, the midpoint of 205 K and 225K. Therefore, the cross point of the two, activation behaviors is defined as a characteristic temperature in case a sharp minimum in the derivative curve cannot be observed at high pressures.

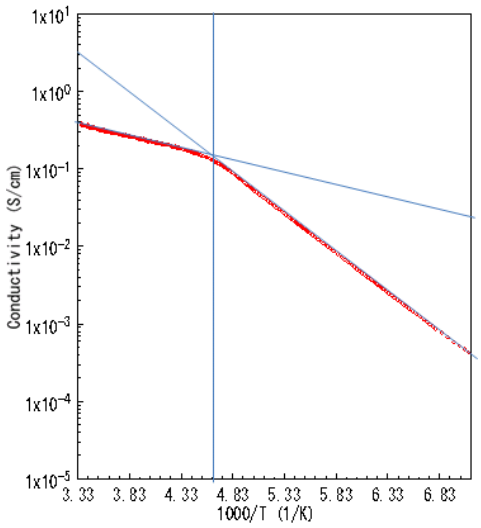


Fig. 3.1.10. Activation plot of the electric resistivity at 27kbar.

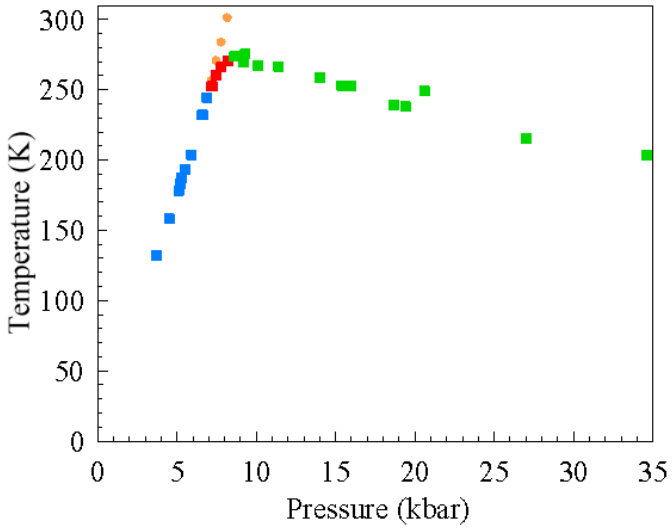


Fig. 3.1.11. Phase diagram of TTF-CA determined by the electric resistivity measurements. Blue, red, and green squares represent temperatures of the sharp minima of resistivity in Fig. 3.1.3 (a) (4.5kbar <P< 6.6kbar), temperatures of the sharp minima of d($ln\sigma$)/d(1/$T$) in Fig. 3.1.6 (b)~3.1.8 (b) (7.8kbar <P< 16kbar), and the points where the activation energy is changed in Fig. 3.1.10 (27kbar <P). Orange circles represent pressures of resistivity minima under pressure variation in Fig. 3.1.3 (b).

Thus defined characteristic temperatures are plotted against pressure in Fig. 3.1.11, which constructs a phase diagram of TTF-CA determined by the resistivity measurements along the **a** axis. The orange circles indicate the pressures where the resistivity takes minima under temperature variation in Fig. 3.1.3 (b).

### 3.1.2 Discussion

The phase diagram (Fig. 3.1.11) constructed on the basis of the resistivity behavior is compared with the previous one in a pressure range below 10kbar in Fig. 3.1.12 [49]. The blue, the red, and the green squares and the orange circles are identical to the symbols in Fig. 3.1.11. The open red circles taken from the previous work indicate the points where the conductivity takes peaks. There is no significant difference between the present and previous results for pressures up to 7kbar. Above 7kbar, the two results differ appreciably; instead, the green circles are located close to the red open circles above 7kbar. The implication is discussed later.

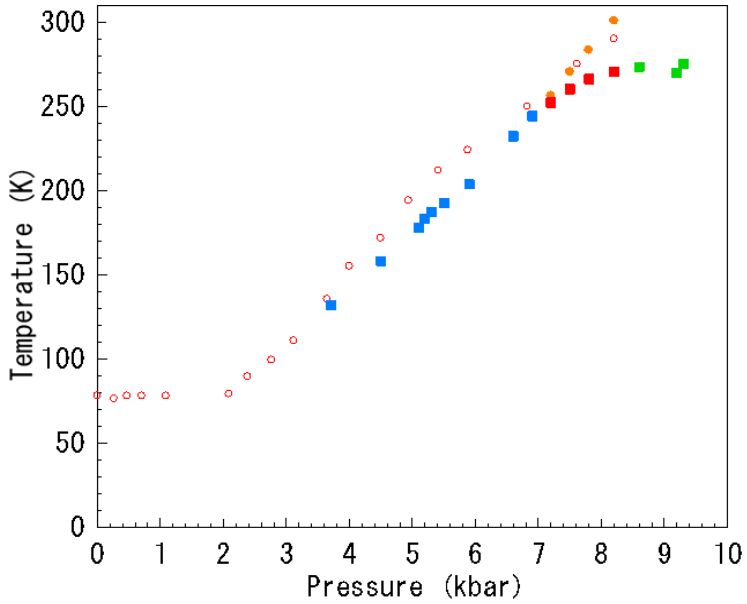


Fig. 3.1.12. Phase diagrams of TTF-CA. Blue, red, and green squares and orange circles are identical to the symbols in Fig. 3.1.11. The open red circles mean the points where the conductivity takes maximum peaks determined in the previous measurements [49].

Next, the phase diagram proposed in the present study is compared with that determined by the NQR and IR measurements in Fig. 3.1.13 [9, 23, 25]. The points of the dimerization transition determined by NQR (open and closed blue triangles) are approximately in accordance with those determined by the resistivity measurements (blue, rea, and green squares), indicating that the resistivity anomalies are attributable to the dimerization transition. Rigorously, below 8kbar the resistivity anomalies are not coincident with the NQR anomalies under the gas pressure (open blue triangles) but they are coincident under the oil pressure (closed blue triangles) [17]. This is because, as is well known, the internal pressure of the oil medium in a clamp type pressure cell is reduced approximately by 2kbar on the solidification of oil. The open red square indicates the point where the lattice dimerization transition is suggested to occur by the IR measurement predicts. Around 15kbar, the dimerization transition temperature determined by the IR, NQR, and the resistivity measurements are different. This can be due to differences in time scale between lattice fluctuations and the experimental probes. The dimerization transition above 10kbar is suggested to be a continuous or the weak first-order transition by the NQR measurements; the lattice fluctuations are expected to slow down on approaching the dimerization transition. If the time scale of the IR measurements, $10^{13}$~$10^{14}$Hz, faster than that of the lattice dynamics, the snapshot of the lattice dimerization is captured by the former even at temperatures far from the transition temperature. In contrast, the time scale of NQR is of the order of MHz or slower and is by far slower than the IR measurements; thus the time scale of the dimerization fluctuations is expected not to enter into the range of NQR until the vicinity of the long-range order. As for the resistivity, the anomaly occurs at temperatures lower than those of the NQR measurements. The resistivity cannot detect the lattice dimerization directly but may reflect changes in the properties of conduction carriers at the transition, differently from the spectroscopic measurements like the NQR and IR measurements. As shown in Fig. 1.20 (b), the split of the NQR frequency continues to be enhanced in a range of 10~30K below the onset marked by the closed blue squares. Thus, the resistivity anomaly likely occurs at temperatures where the dimerization completes. In the low pressure region, where the lattice dimerization transition is of the first-order, the lattice fluctuations should keep fast all the way down to the transition. Hence, the coincidence between the transitions seen by these measurements is reasonable.

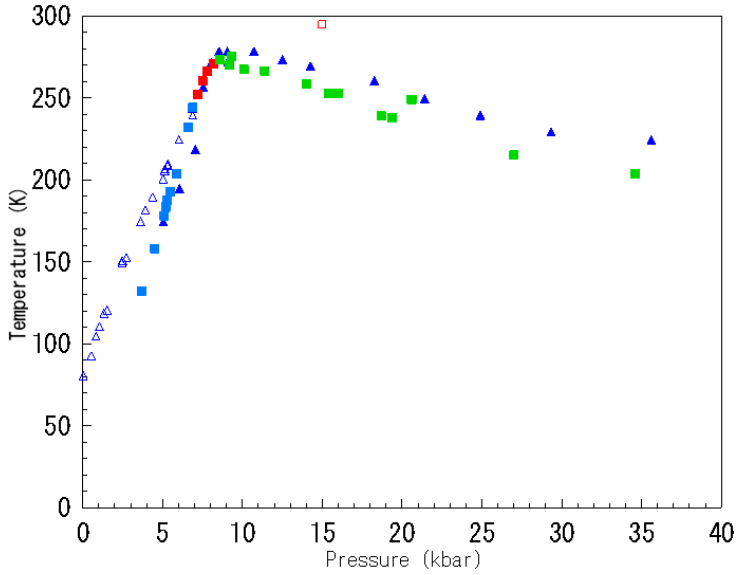


Fig. 3.1.13. Phase diagram of TTF-CA. The blue, the red, and the green squares are the same as the symbols in Fig. 3.1.11 and Fig. 3.1.12. The open blue triangles indicate the dimerization points determined by the previous NQR measurements under the gas pressure [23]. The blue triangles represent the dimerization points determined by the recent NQR measurements under the oil pressure [25]. The open red squares at 15kbar at room temperature indicate the transitions suggested by IR measurements [9].

Next, we focus our attention on the orange circles in Fig. 3.1.11 and Fig. 3.1.12, which indicate the temperatures giving the resistivity minimum as shown in Fig. 3.1.3 (b). They appear at 7~9kbar in the temperature region above 250K. The pressure dependence of resistivity in Fig.3.1.1 at room temperature also shows a rounded minimum around 8.8kbar, which is considered to originate from the common origin to those appearing in Fig. 3.1.3 (b). Figs. 3.1.14 (a) ~ (c) show the pressure dependence up to 20kbar of the NQR resonance frequency, the fractional ratio of the neutral and ionic molecules estimated from the IR measurements, and the conductivity, respectively, where Figs. 3.1.14 (a) and (b) are identical to Fig. 1.21 (b) and Fig. 1.23, respectively [12, 28]. Around 7.8~9.8kbar (the orange-colored region), the NQR frequency steeply changes between the frequencies of the neutral and ionic states, and the IR-detected volume ratio crosses 0.5, indicating that the charge transfer evolves with the total $\rho$ crossing 0.5 in this pressure range. The peak in the conductivity is observed at approximately the same pressure within a pressure error of about ±1kbar. This indicates that the conductivity is most enhanced around the points where $\rho$ is 0.5. Furthermore, the electrical conduction in TTF-CA around 7.8~9.8kbar is predicted to be strongly related to the dynamical charge transfer. It is noted that no split of the NQR spectra is observed under the pressure

as is shown in Fig. 3.1.14 (a), indicating that the dimerization, if it exists, fluctuates faster than the NQR frequency. The conductivity only shows a broad peak without a jump and no anomaly around 15kbar where the dimerization transition is suggested in the IR measurements.

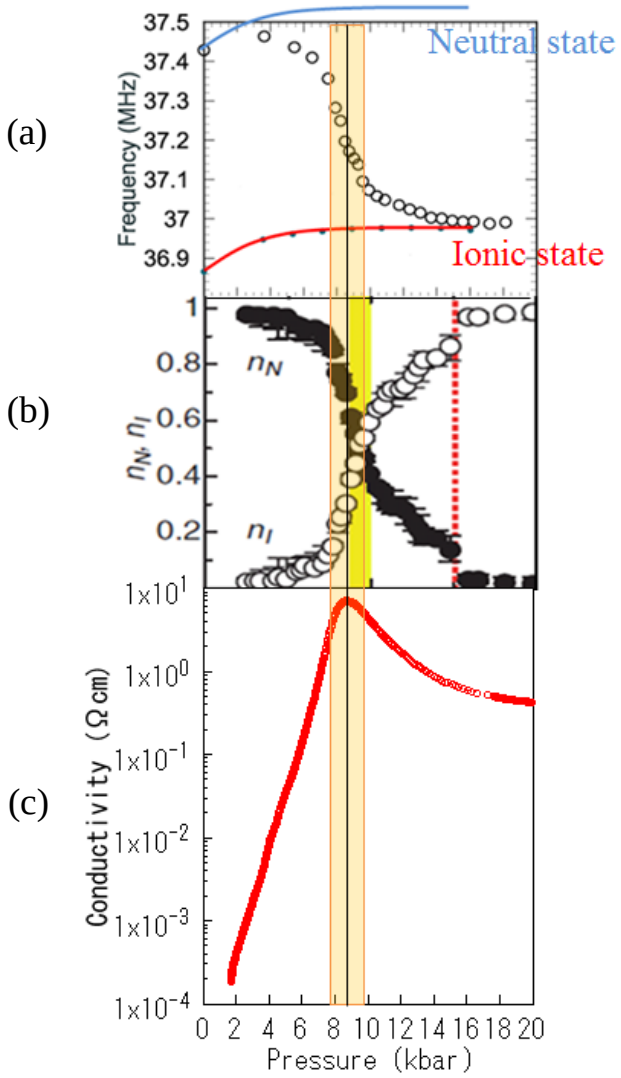


Fig.3.1.14. Pressure dependences of (a) NQR frequency [25], (b) the ratio of the *N* and *I* molecules detected by IR measurements [9], and (c) conductivity. The transient region is indicated by the orange cover.

The present conductivity results support the phase diagram constructed by the neutral phase, the ferroelectric ionic phase and the paraelectric ionic phase, and in particular, the presence of the crossover where only the charge transfer occurs without the lattice dimerization. We address that this crossover as the original NI transition without the symmetry breaking.

## 3.2 Carriers of the electric conduction of TTF-CA

As shown in the last section, the values of the electric resistivity of TTF-CA in the pressure region of 8~10kbar in between two insulator phases (Figs. 3.1.3 (a) ~ (c)) reaches around 0.1Ωcm, which is in the range of the values of organic conductors. Another notable character of the electric conduction is apparently metallic temperature dependence of resistivity (Fig. 3.1.1 (a) and (b)), between the *N* and $I_{ferro}$ insulator phases. We call the metal-like high conductivity between the two insulator phases the excess conduction here. In this section, the carriers responsible for the excess conduction are discussed in the light of the role of NIDW excitations.

### 3.2.1 Results

Although a band gap of the neutral and the ionic phases along the one-dimensional direction, which is explained more closely later, should not change by pressurization, electric resistivity of TTF-CA shows dramatic decreases on the phase boundary. At ambient temperature and pressure, the resistivity in the neutral phase is several hundred kΩcm, and it shows nearly six orders decrease to 0.1Ωcm on the boundary. We call the decrease in resistivity that we cannot explain only with the conventional band picture excess conduction. In a region where the excess conduction is observed, the resistivity also shows metallic behavior (Fig. 3.1.3 (a) ~ (c)), which is colored in the phase diagram of TTF-CA (Fig. 3.2.1). As this figure shows, the excess conduction appears in a region between the *N* phase and the $I_{ferro}$ phase, and between the *N* phase and the $I_{para}$ phase; however, it is not observed between the $I_{ferro}$ phase and the $I_{para}$ phase, where only the lattice dimerization occurs. These results indicate that the excess conduction is mainly attributed to the charge transfer between the neutral and the ionic states.

Next, the pressure dependence of resistivity measured along the **a**, **b**, and **c** directions is shown in Fig. 3.2.2. Although the absolute values are different, the resistivity data all show qualitatively similar pressure dependence; namely, they have minima, which, however, occur at different pressures partly because of the experimental ambiguity in absolute value in separately preformed measurements for the three directions. The resistivity decreases nearly exponentially up to the pressure of the resistivity minima. Figs. 3.2.3 (a) and (b) show the anisotropies of conductivity defined as the ratio of the conductivities along different directions, ($\sigma_a/\sigma_b$) and ($\sigma_a/\sigma_c$). Fig. 3.2.3 (a) shows the temperature dependence of the ratios. Fig. 3.2.3 (b) shows those with the pressure correction, which means that pressure is shifted so that the pressures of the resistivity minima coincide for three directions as a tentative analysis; the origin of the difference of the pressure values of the resistivity minimums is not known at present. Nevertheless, it is obvious that a large enhancement of the anisotropy 7~12kbar is visible, whether the correction is made or not (Fig. 3.2.3 (a) and (b)). The peak appears around 9kbar, where $\rho$ is estimated at about 0.5 (Fig. 3.1.14). These results strongly suggest that the excess conduction has strong one-dimensional feature, which is

distinguished from the conduction outside of this pressure region, and thus is attributable to the charge transfer of NI transition along the **a** axis. Fig. 3.2.4 shows temperature dependence of the resistivity under pressures in the three directions around 7kbar, and indicates that only the **a** axis conduction is attributable to the excess conduction. In contrast, insulating behaviors are observed in other directions.

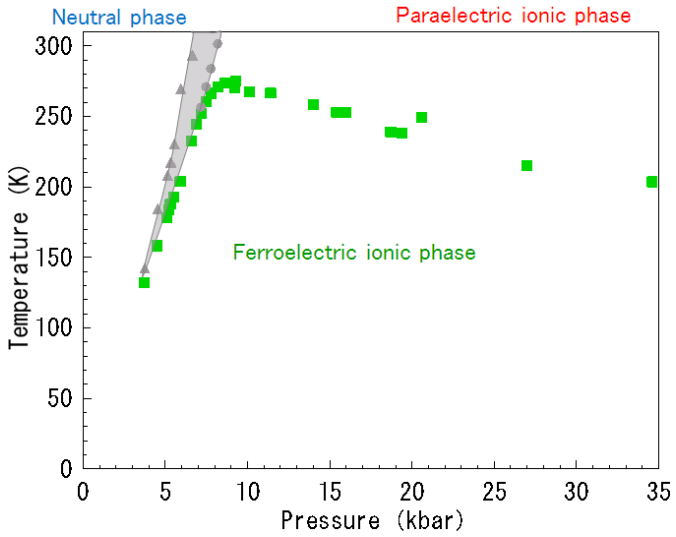


Fig. 3.2.1. Phase diagram. The region where the excess conduction is observed was grey-colored. The gray triangles are defined as the temperatures where the excess conduction starts in cooling process.

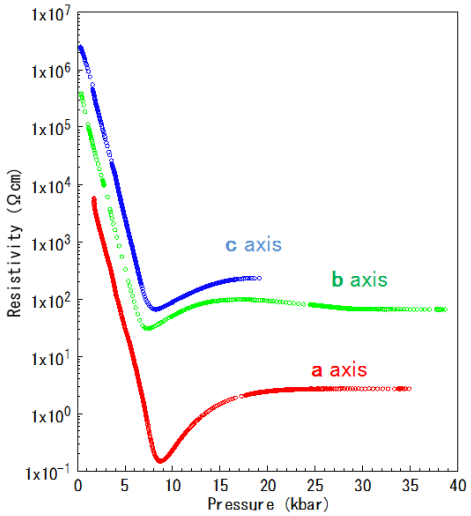


Fig. 3.2.2. Pressure dependence of electric resistivity along **a**, **b** and **c** axes.

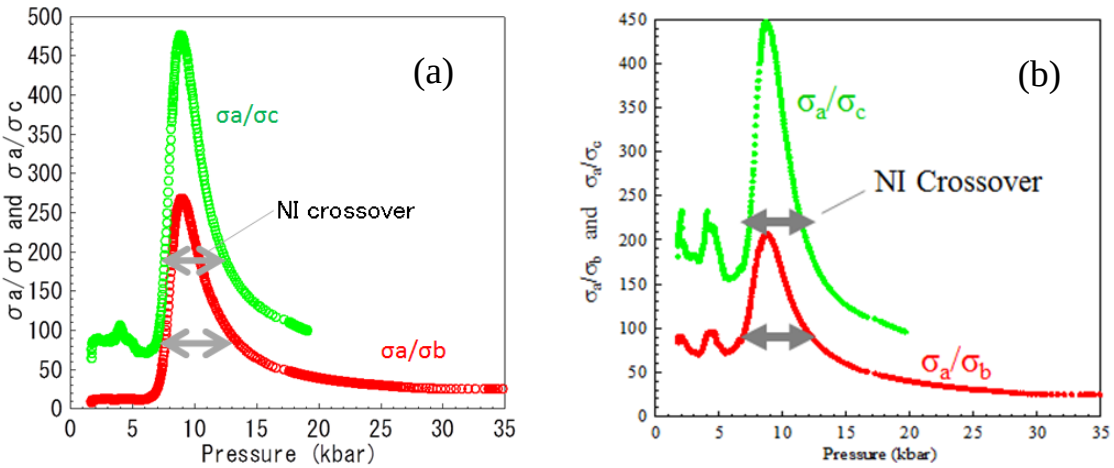


Fig. 3.2.3 Ratio of conductivities along different directions at room temperature. The red and green symbols indicate the ratio of the conductivity along **a** axis to that along **b** axis, and the ratio of the conductivity along **a** axis to that along **c** axis, respectively, without pressure correction (a) and with correction (b).

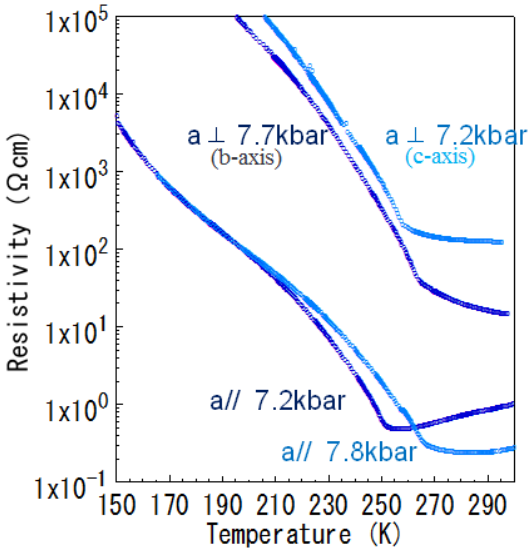


Fig. 3.2.4. Temperature dependence of electric resistivity along **a**, **b**, and **c** axes in the charge transfer crossover region.

In order to analyze the resistivity behavior in more detail, we carried out more detailed resistivity measurements in a pressure range of 5.5-11.5kbar in approximately 0.1kbar interval. For monitoring pressure in the pressure cell accurately, we mounted the Manganin wire, whose resistivity gives the pressure value, into the pressure cell as well as the sample. The results are shown in Fig. 3.2.5 (a), and the *P-T* phase diagram constructed from the experimental results is shown on the bottom plane in Fig. 3.2.5 (a) and in Fig. 3.2.5 (b). The green line means the dimerization transition determined in the same way as explained in the section 3.1, and the gray line corresponds to the peak positions appearing in the pressure dependence of the conductivity at fixed temperatures. The conductivity data around the peaks were well fitted by cubic functions. Note that the gray line indicates not a transition but crossover related to the charge transfer as indicated by the NQR results. Here, we call the crossover NI crossover. We assume that the characteristic points correspond to the NI boundary across $\rho$=0.5, which is confirmed at least at room temperature as shown in Fig. 3.1.14. In fact, it is hard to confirm for other temperatures that the peaks of the conductivity correspond to the exact NI boundary, since there are no experimental data on molecular valency to be compared. However, the pressure profile of the conductivity for all the temperatures are homothetic with that for room temperature as shown in the scaling analysis described in the next section. Therefore, we regard the gray line as the NI boundary. The development of the NI boundary in the phase diagram is visible in the contour plot of the resistivity values as shown in Fig. 3.2.6. The NI boundary or crossover is found to develop in a tilted direction in the pressure-temperature plane. The red region around the gray line, where the conductivity is high, are located in the pressure region 8.5~ 9.5kbar above the dimerization transition temperatures. This result indicates that the excess conduction is not related to the static dimerization.

(a)

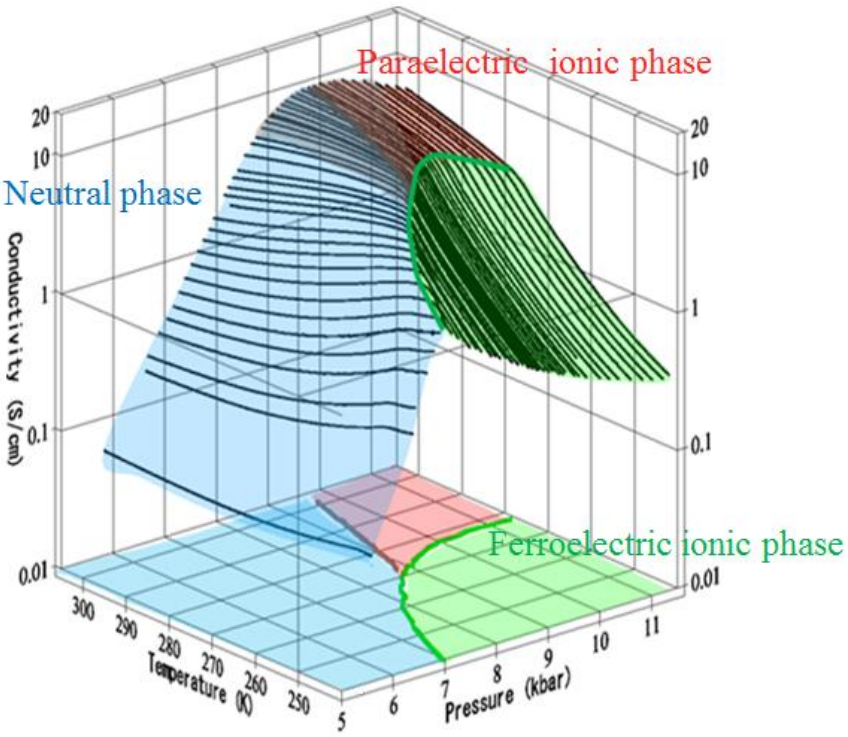


(b)

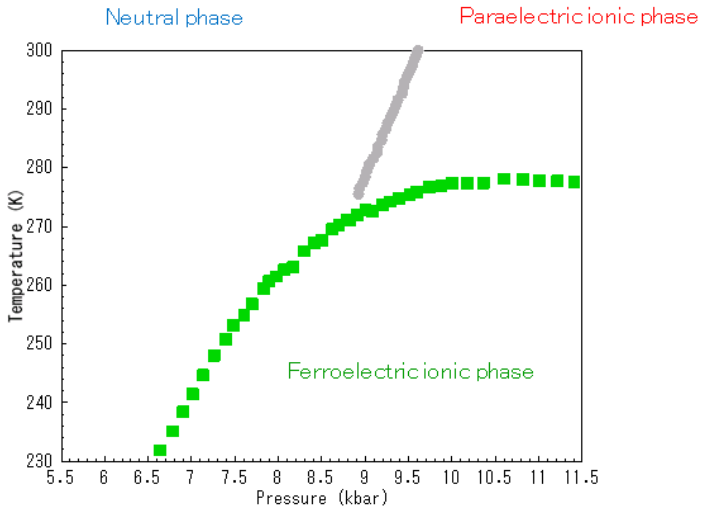


Fig. 3.2.5 (a) Electric conductivity in the NI crossover region (b) Detailed phase diagram in the NI crossover region, constructed on the basis of the experimental data of (a).

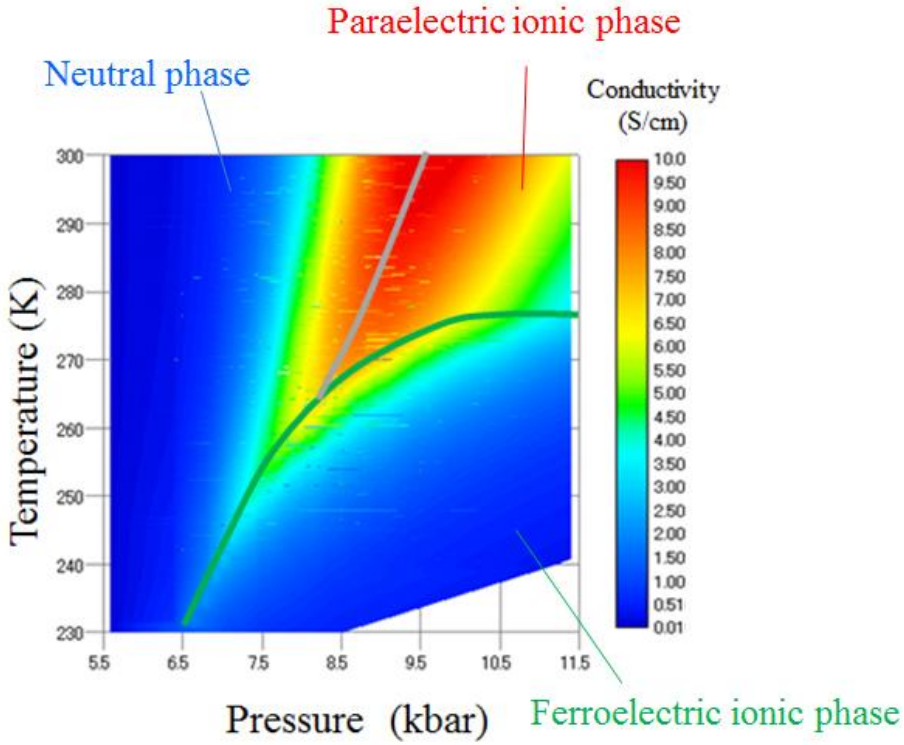


Fig. 3.2.6. Contour plots of electrical conductivity in the phase diagram

### 3.2.2 Discussion

In this section, we discuss the carriers responsible for the excess conduction on the basis of the analysis of the results in Fig. 3.2.5 (a). First, the theoretically proposed electronic states in the NI system are summarized [42] and especially the possibility of metallic state in the NI system is discussed.

Fig. 3.2.7 (a) and (b) illustrate one-particle excitation energies, which are predicted from the Hubbard model generally dealt with for the NI system but without the electron-lattice interaction. The excitation energies are described in terms of the onsite Coulomb energy $U$, the nearest neighbor Coulomb energy $V$, and the energy difference between the HOMO and the LUMO, $\Delta_0$. The relationship $\Delta_0$-$U$=$I_D$-$E_A$ holds and the condition of $\Delta_0$-$U$=$\alpha V$ is satisfied on the NI transition. The CT energies in the neutral and the ionic phases, expressed in Chapter 1 by using $I_D$ and $E_A$, are also described as $h\nu_{CT}$=$\Delta_0$-$U$-$V$ and $h\nu_{CT}$=-$\Delta_0$+$U$+(2$\alpha$-1)$V$, respectively, by using $\Delta_0$ and $U$. $E_N$ and $E_I$ are the energies required to dissociate an electron-hole pair to infinity, which correspond to the energies of the band gap; that is, the energies to create carriers. In Fig. 3.2.7 (a), $h\nu_{CT}$, $E_N$, and $E_I$ are shown with $\Delta_0$ as a parameter and the CT excitation energy was verified in the experiments as explained in Chapter 1. In Fig. 3.2.7 (b), the parameter $\Delta_0$ in the horizontal axis of Fig. 3.2.7 (a) is converted to $V$, which can be controlled by pressure in experiments because $V$ is sensitive to the change of lattice parameters. In Fig. 3.2.7 (b), the values of $\Delta_0$=2.9eV, $U$=1.5eV, $V$=0.7eV, and $\alpha$=2 are used [42]. It is noted that the calculation based on the Hubbard model in the NI system does not predict metallic states because there is always a gap, as shown in Fig. 3.2.7 (a) and (b). In fact, the Drude peak, which should be observed in metallic materials, has not so far been observed in the NI materials experimentally. Another noticeable point in Figs. 3.2.7 (a) and (b) is that the energies $E_N$ and $E_I$ are always higher than the CT energy, because the CT state is more stable by the energy $V$ than the band gap, where $V$ corresponds to the binding energy of the electron-hole pair. The NI system has the CT energy 0.6~0.7eV as shown in Fig. 1.2.3 (experiments) [1] and in Fig. 3.2.7 (b) (calculation). Therefore, to generate carriers in the NI system, the energy over 0.6eV is needed.

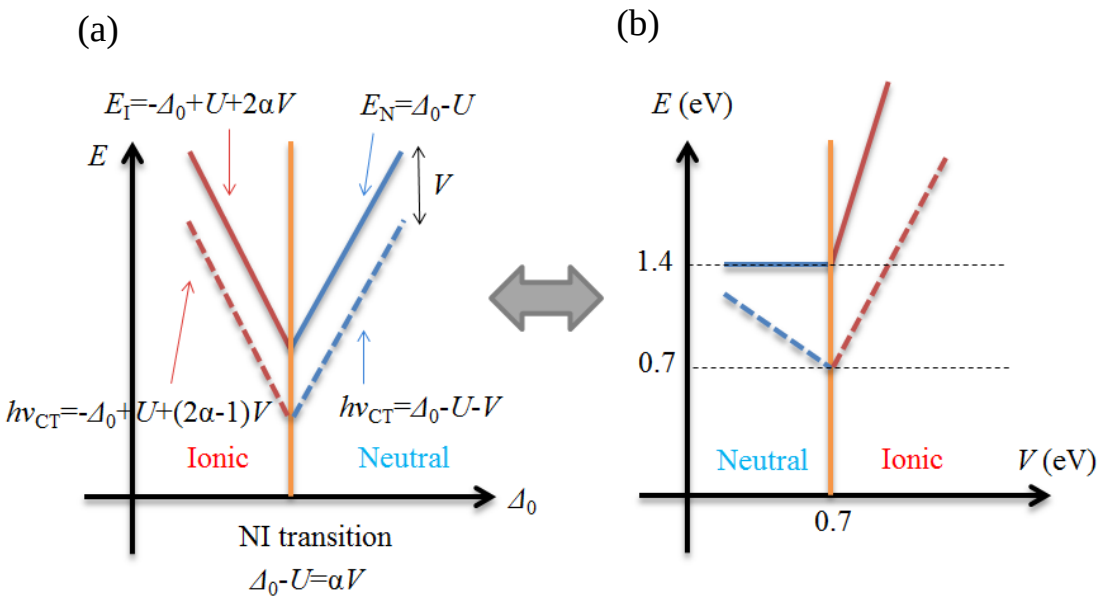


Fig. 3.2.7 Excitation energies in the NI system as functions of (a) $\Delta_0$ and (b) $V$.

While the discussion above is for the one-dimensional NI system, TTF-CA is a "quasi"-one-dimensional system, and thus three-dimensionality in **b** and **c** directions has to be taken into account. The transfer integral along **a** axis, approximately 0.2 eV [42, 63], is the larger than those in other directions; the value in **b** axis, the second largest, is about 0.02eV [63]. According to the band calculation, TTF-CA has an "indirect" band gap in the direction of Y (0, 1, 0)→Γ (0, 0, 0) [63], which is determined by the "direct" band gap at Γ point and the transfer integral along the **b** axis. Supposing the CT energy, here 0.6eV, as the "direct" band gap at Γ point, the indirect band gap is estimated at 0.52~0.62eV. However, the value of the resistivity reaching around 0.1Ωcm in the NI crossover region in the experiments is hardly explained by such a large band gap over 0.5eV. Therefore, to explain the present experiments, other mechanism than postulated by the Hubbard model should be invoked.

The NIDW excitations expected to be low-lying in energy has been theoretically suggested in the NI boundary. Considering high conductivity and one-dimensional nature of the excess conductivity around the NI crossover, they can be a promising candidate for the carriers in question. However, what we envisage here are not classical DWs appearing in the boundary between two different phases associated with the first-order transition but elementary excitations possessing DW-like properties in the non-dimerized phase. In order to examine whether the carriers in the NI crossover are NIDW's, we have to find features indicating the NIDW in the resistivity results. However, the resistivity is not activated but behaves metallic in the NI crossover region. Below, the results in Fig. 3.2.6 are revisited to reexamine the resistivity behavior. The NI boundary and crossover are tilted in the pressure-temperature phase diagram, and thus under temperature variation at fixed temperatures the resistivity turns out to be measured across the NI boundary. We make the following attempts to "correct" the inclined crossover line. Fig. 3.2.8 (a) shows the plots of the conductivity, which was measured under temperature seep, as functions of pressure with temperature fixed. The green and grey lines shown are the dimerization transition line and the NI boundary lines determined in the same way as in Figs. 3.2.5 and 3.2.6. If we adopt the pressure difference from the crossover pressure as a parameter at each temperature instead of pressure itself, Fig. 3.2.8 (a) is transformed to Fig. 3.2.8 (b), where the NI boundary runs vertical.

Fig. 3.2.9 shows temperature dependence of the resistivity along the NI boundary, which corresponds to the gray line in Fig. 3.2.8 (b). Remarkably, the resistivity behaves like non-metallic in contrast to the metallic behavior at fixed pressures. Though the temperature region is narrow, this result can be regarded as an activated behavior as shown in Fig. 3.2.10. The activation energy is estimated at 0.055eV, which is much smaller than the CT energy, and thus it is unlikely that the one-particle excitations explained previously.

(a)

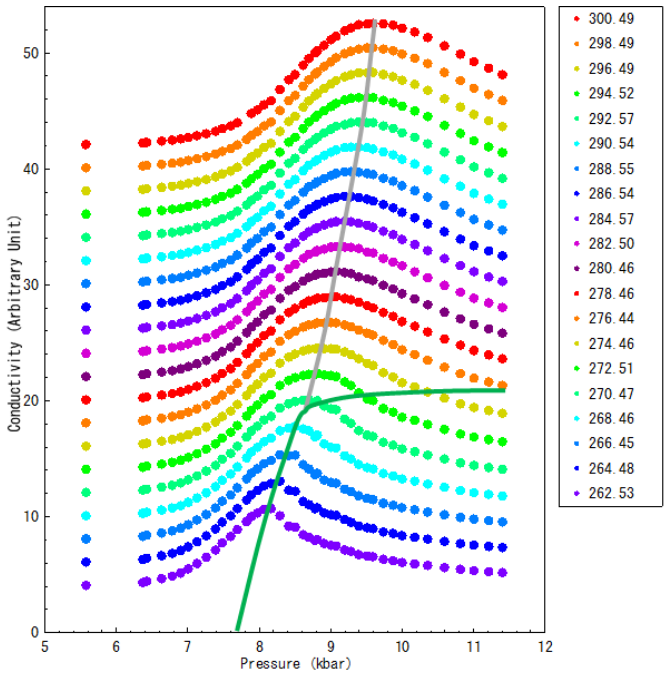


(b)

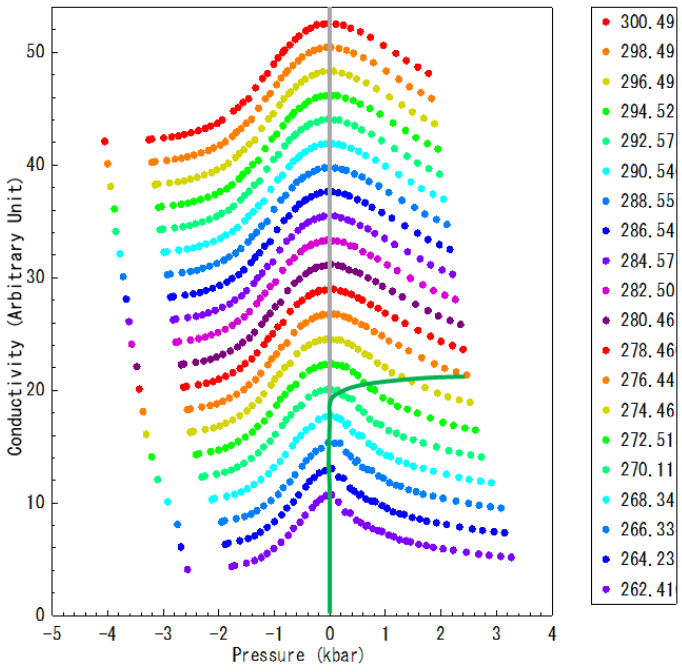


Fig. 3.2.8 (a) Electrical conductivity at fixed temperatures as functions of pressure (a) and deviation from the crossover pressure (b).

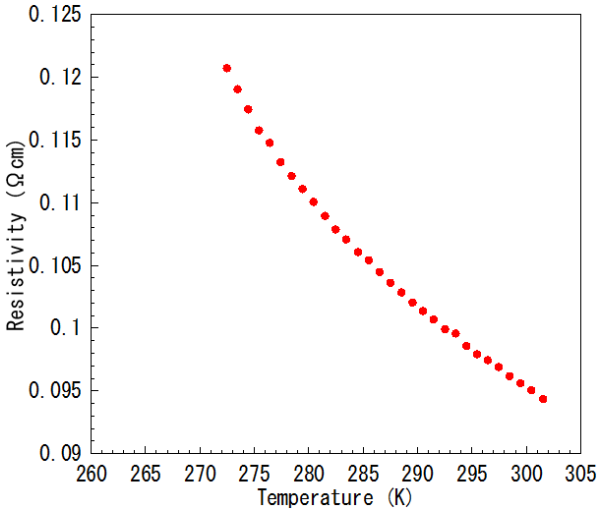


Fig. 3.2.9. Temperature dependence of the electric resistivity along the NI boundary.

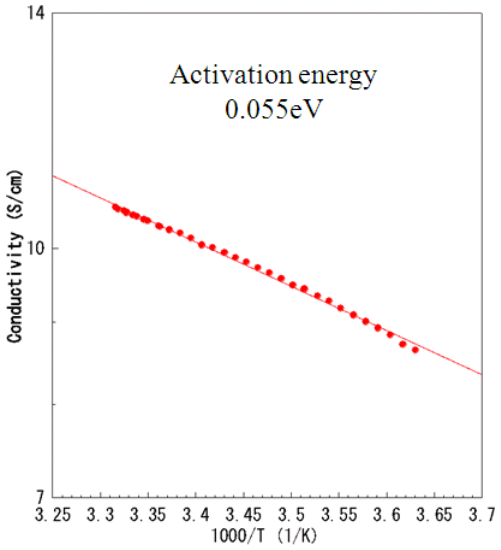


Fig. 3.2.10. Activation plot of the electric resistivity along the NI boundary.

Next we quantitatively compare the experimental value of the carrier excitation energy with the theoretically predicted NIDW excitation energy. The CT excitation, where one ionic DA pair is excited in the neutral phase as illustrated in Fig. 3.2.11 (a), requires the energy of $h\nu_{CT}=I_D-E_A-V=\Delta_0-U-V$ as described previously. In the case of Fig. 3.2.11 (b), where the two ionic DA pairs are created, the excitation energy of the ionic DA pairs $E$ is $E=2\times(\Delta_0-U-V)-V$. If the excitation of the two DA pairs is created at the NI boundary, the condition of the NI transition $\Delta_0-U=2V$ has to be satisfied, where the Madelung constant $\alpha$ is 2 for simplicity. Then, $E=2\times(\Delta_0-U-V)-V=2\times(2V-V)-V=V$, indicating that the energy needed to excite two DA pairs is the same as that for one DA pair at the NI boundary. In the similar way, how many DA pairs are created, the excitation energy is invariably equal to $V$. As seen in such a simple consideration, the DWs between the neutral and ionic domains are elementary excitations at the NI boundary, namely, they can be called NIDWs. The NIDW is also predicted to be able to move freely, not costing additional energy. Since the excitation energy $V$ corresponds to the energy of the two NIDWs as shown in Figs. 3.2.11 (a) and (b), the excitation energy per one NIDW is $V/2$. Furthermore, the NIDW is predicted to have quantum properties; that is, the NIDW gains the kinetic energy through the transfer integral, which are distinct properties from those in higher dimensions. Therefore, the NIDW excitation energy $E_{DW}$ becomes smaller than $V/2$, which is also much smaller than the CT energy. How much the energy $E_{DW}$ is decreased from $V/2$ can be estimated by referring to the theoretical result shown in Fig. 3.2.12 with the values of the transfer integral and the nearest neighbor Coulomb interaction $V$ [42]. Here, we estimate those values in the NI crossover region. At ambient pressure, the relationship between the lattice constant and the transfer integral along the **a** axis is estimated from the temperature dependence of the lattice constant obtained with the X-ray diffraction [28], and that of the transfer integral obtained from the first principle calculation along with the tight-binding approximation [63]. The calculation shows that the transfer integrals in the $N$ and $I_{ferro}$ phases at ambient pressure are reported to change by about 5% and 21% with a 1% change of the lattice constant on average, respectively. However, this change of the transfer integral in the $I_{ferro}$ phase appears to be large, because the quantum Monte Carlo theories predict the change of the transfer integral by 14% per 1% change of the lattice constant. In the present study, the change of the transfer integral is linearly averaged in the entire temperature region at ambient pressure, and consequently the transfer integral is assumed to change by 6.8% per 1% change of the lattice constant. Applying this to the pressure dependence of the lattice constant [64], the transfer integrals of 0.17~0.2eV [18, 42, 65-70] at ambient pressure are considered to change to 0.208~0.245eV when reaching the NI boundary pressure. As for the nearest neighbor Coulomb interaction $V$, the change of the Madelung energy under pressure was already estimated on the basis of the pressure dependence of the lattice constant. Using of $V$ = 0.6~0.7eV [1, 42, 66, 69, 70], the Coulomb interaction $V$ at the NI boundary pressure is estimated at 0.615~0.718eV. Thus, the value of $2t/V$ in the horizontal axis in Fig. 3.2.12 is

estimated at 0.58~0.8, giving an excitation energy of the NIDW 0.03~0.066eV. The experimental result 0.055eV is in this range.

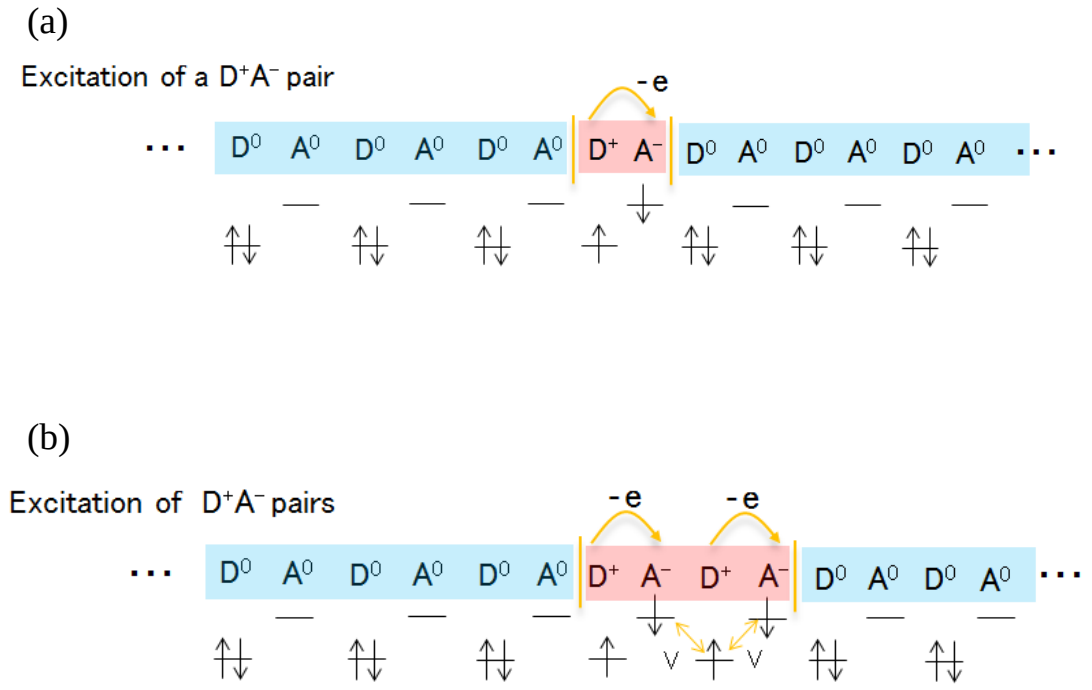


Fig. 3.2.11 (a) One ionic DA pair excited in the neutral phase. (b) Two ionic DA pairs excited in the neutral phase.

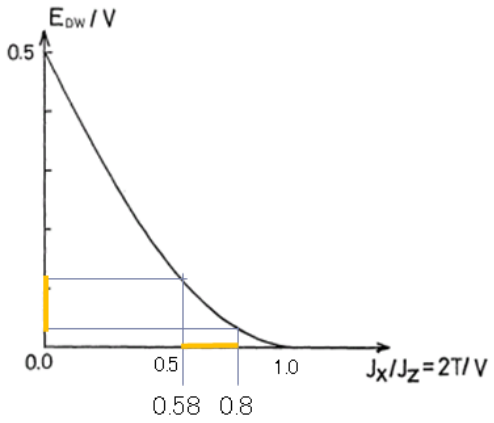


Fig. 3.2.12. The excitation energy of the NIDW as $2T/V$, where $T$ is the transfer integral and $V$ is the Coulomb interaction [42].

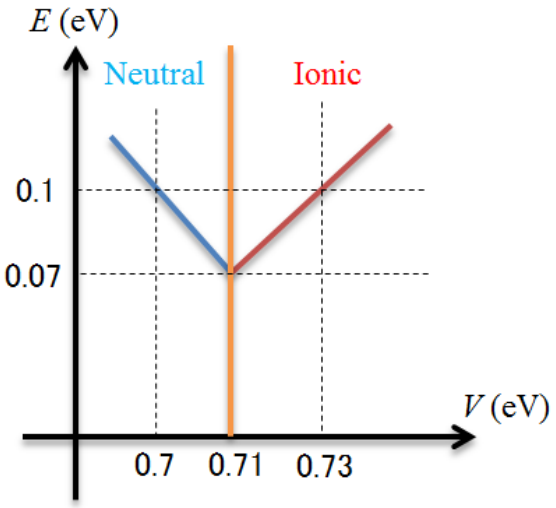


Fig. 3.2.13. Quantum Monte Carlo simulation of the NIDW excitation energy against $V$.

Quantum Monte Carlo simulation [42] predicts the *V* dependence of the NIDW excitation energy, which has a minimum at the NI boundary as shown in Fig. 3.2.13. In order to see this profile experimentally, the activation energy was evaluated along lines parallel to the NI boundary line. For example, the activation plots of conductivity at pressures deviated from the NI boundary by 0.3kbar and -0.3kbar are shown in Fig. 3.2.14. In either case, the metallic temperature dependence of the resistivity measures at a fixed pressure is not observed. The pressure dependence of the activation energy, which was estimated from the conductivity in 275-301K above the dimerization transition, is shown in Fig. 3.2.15. It appears qualitatively consistent with the theoretical prediction, although the experimental data show the rounded minimum unlike the V shape in the theoretical prediction (Fig.3.2.13). This is because the simulation was performed for an absolute zero while the experiments were performed in the crossover region at finite temperatures. The agreement between experimental results and theoretical prediction about the appearance of the minimal gap at the NI boundary and its absolute value supports the notion that the carrier in the NI crossover is the NIDW.

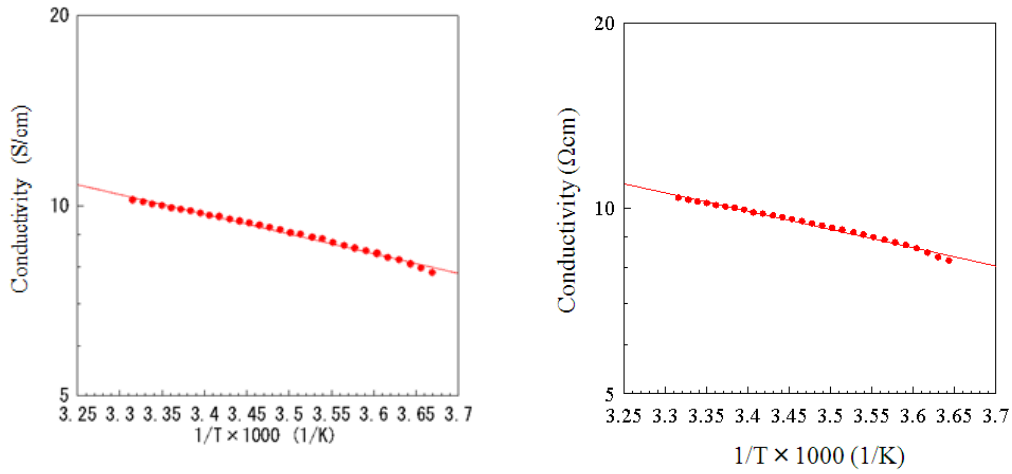


Fig. 3.2.14. Activation plot of conductivity on a line parallel to the NI crossover line, keeping pressure differences of left -0.3kbar and right +0.3kbar.

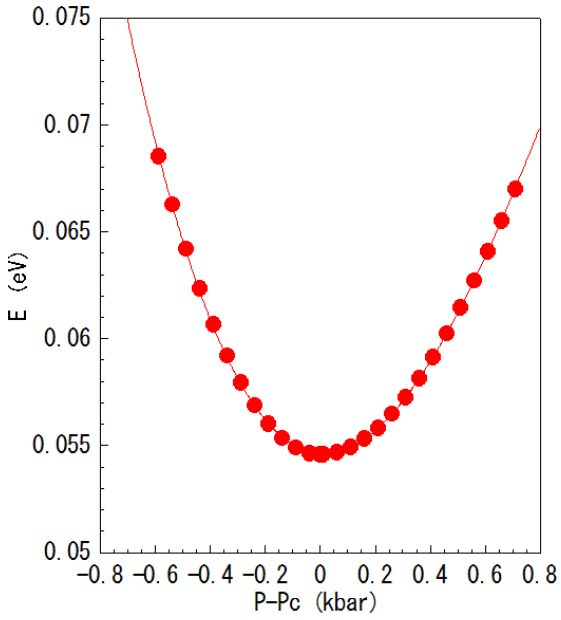


Fig. 3.2.15. Pressure dependence of the activation energy of electric conductivity.

## 3.3 Scaling analysis

As described in section 3.1, the resistivity and NQR measurements indicate the existence of the NI crossover, which implies the existence of a critical end point somewhere on the phase diagram. The BEG model as explained in Chapter 1 predicts that the critical end point exists outside the $I_{ferro}$ phase [54], whereas the recent quantum Monte Carlo simulation predicts that it would lie behind the $I_{ferro}$ phase [71, 72]. To address the issue of the critical end point in the present NI phase diagram, the conductivity around the NI boundary was examined with a scaling analysis. In general, there are two types of scaling analyses. One is the thermodynamic scaling, which is around the critical point at a finite temperature, and the other is the quantum scaling, which is around the quantum critical point at an absolute zero. The scaling examined here, however, is different from those two and is an attempt to scale the physical quantities around room temperature in a way similar to the quantum scaling. In general, the energy scale of systems determined by Hamiltonian is much higher than that of temperatures where experiments are performed. For example in the NI system, the nearest neighbor Coulomb interaction $V$, which is included in the Hamiltonian and triggers the NI transition, is estimated at about 0.6~0.7eV. Therefore, with respect to the energy scale in Hamiltonian, phenomena happening around room temperatures can be regarded apparently as those happening at low temperatures. The scaling on the basis of this idea was first applied to the Mott transition in organics with low critical end points of Mott transition and the resistivity is successfully scaled in a quantum critical manner [73, 74]. Meanwhile, it is suggested that the NI transition originally without the lattice dimerization would not be accompanied with symmetry breaking and can have the critical end point of the first-order transition similarly to the Mott systems, though the critical end point has never been identified experimentally. Thus, in an analogy with the Mott transition, we apply the Mott scaling of resistivity to the NI system, postulating the virtual critical end point of the charge transfer behind the dimerized ferroelectric ionic phase as illustrated in Fig. 3.3.1.

### 3.3.1 Method of analysis

As shown in Fig. 3.3.2, we assume that there is a critical point at zero temperature and a critical region spreading from the critical point. Pressure and temperature are originally independent external fields, but in the critical region, these external fields are not independent. Here, a ruler connecting pressure and temperature, is represented by a form of $T_0=c(P-P_c)^{z\nu}$, where $P$ is pressure and $P_c$ is a critical or crossover pressure of the NI transition. $P_c$ in the crossover region, which is assumed to correspond to the NI boundary, can be called Widom line. $\nu$ is the critical exponent of the correlation length, and $z$ is the dynamical exponent. The configuration of the critical region is determined by $z\nu$. $c$ stands for a constant. In the present study, we first normalize the resistivity at each pressure and temperature, $R(P, T)$, to the crossover value at the same temperature, $R_c(T)$ and attempt to scale the normalized electric resistivity, $R(P, T)/R_c(T)$ with temperature

measured with the ruler ]$T_0$=$c$($P$-$P_c$)$^{zv}$, as depicted in Fig. 3.3.2; For example, the temperature, $T$, of $R(P_1, T)/R_c(T)$ is measured with $T_0$=$c$($P_1$-$P_c$)$^{zv}$ and that of $R(P_2, T')/R_c(T')$ is measured with $T_0$=$c$($P_2$-$P_c$)$^{zv}$. If the two curves of $R(P, T)/R_c(T)$ versus $T/T_0$ for $P_1$ and $P_2$ are on the same curve, it means that the scaling is fulfilled.

This scaling is derived from the quantum scaling. A spatial correlation length $\xi$ diverges as $\xi \propto |P - P_c|^{-\nu}$, where $P$ is adapted as the external filed in this case. Additionally, in the case of finite temperatures, anther characteristic length $\xi_T$ along the temperature direction is needed. This is related to temperature in the form $\xi_T \propto T^{-1/z}$. Development of the critical fluctuation is determined by the development of these two lengths, which is described as $\xi/\xi_T \propto T/(P - P_c)^{z\nu}$. However, it is a problem whether $R(P,T)/R_c(T) \propto \xi/\xi_T \propto T/(P - P_c)^{z\nu}$ is satisfied or not. If the resistivity depends on the correlation lengths $\xi$ and $\xi_T$ the proportional relation noted above is satisfied, but in such a case where the carrier is the NIDW it is still an open question whether the proportional relation is rigorously satisfied or not. It has not been also confirmed that the NI transition has the quantum criticality. Thus, in this study, the quantum scaling is used as a matter of form on the basis of an analogy with the Mott systems.

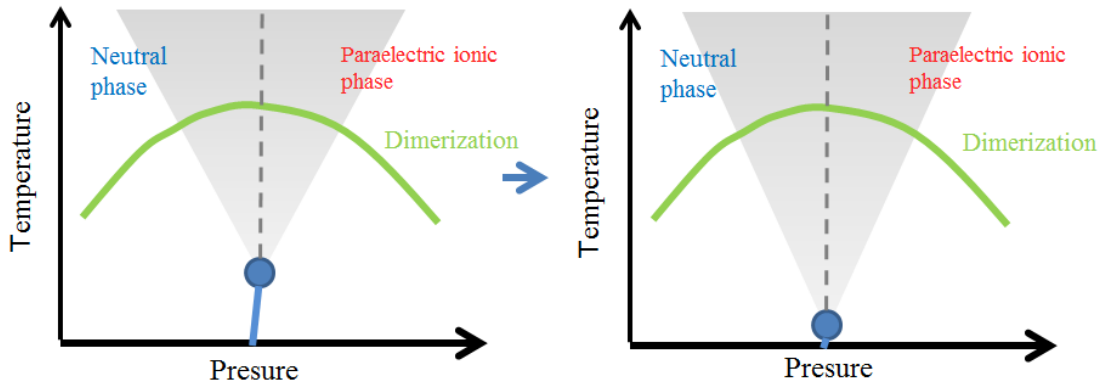


Fig. 3.3.1. Schematic critical point and critical region in the phase diagram the NI transition in the cases of (a) 1st-order transition and (b) quantum phase transition.

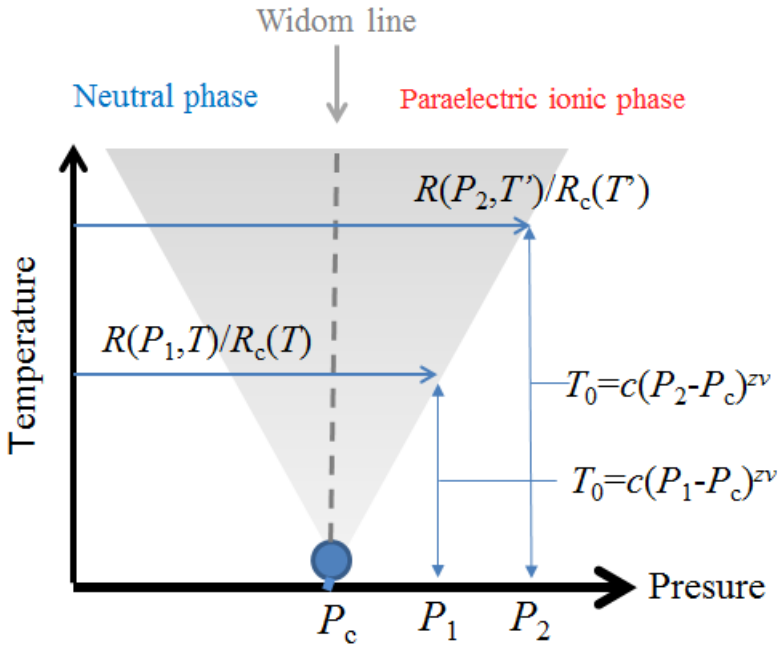


Fig. 3.3.2. Illustration of the scaling. $R(P, T)/R_c(T)$ is scaled with $T/T_0$ . where $T_0=c(P-P_c)^{zv}$.

### 3.3.2 Results

The data used for the scaling analysis are shown in Figs. 3.3.3 (a) and (b). Fig. 3.3.3 (a) shows the pressure dependence of the electric conductivity of TTF-CA at several temperatures (the identical data described in section 3.2). The temperature region is 272~300K, where the crossover is observed. The pressure where the conductivity takes a peak is defined as $P_c$, and the resistivity corresponding to the peak is defined as $R_c(T)$. Fig. 3.3.3 (b) shows the lines along which the data are acquired on the phase diagram.

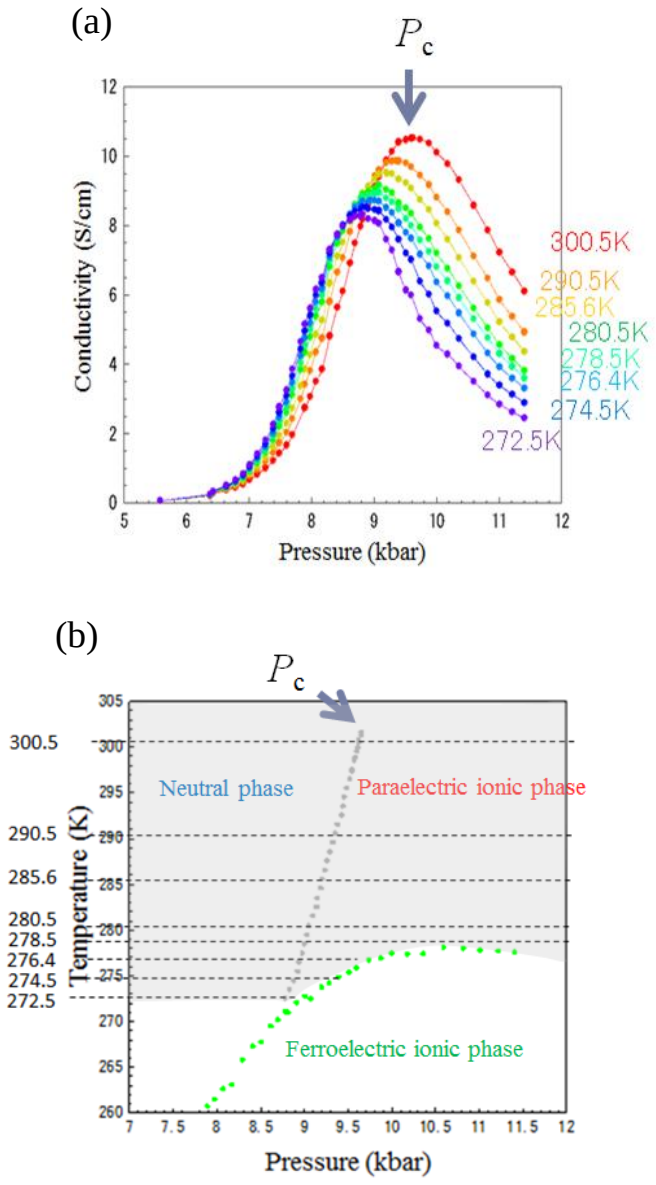


Fig. 3.3.3 (a) Pressure dependence of the electric conductivity of TTF-CA used for the scaling. (b) Measurement paths of the electric conductivity used for the scaling.

The $R(P, T)/R_c(T)$ vs $(P\text{-}P_c)T^{1/zv}$ with different $zv$ values is plotted in Fig. 3.3.4, where the parameter $zv$ is varied from 0.1 to 2. We find the resistivity well scaled when $zv$ is 0.5~0.6. Another plot of $R(P, T)/R_c(T)$ vs $T/T_0$ is shown in Fig. 3.3.5, for $zv$=0.5 and 0.1, indicating the value of $zv$=0.5 gives a successful scaling, which bifurcates into two branches; the neutral regime and the paraelectric ionic regime.

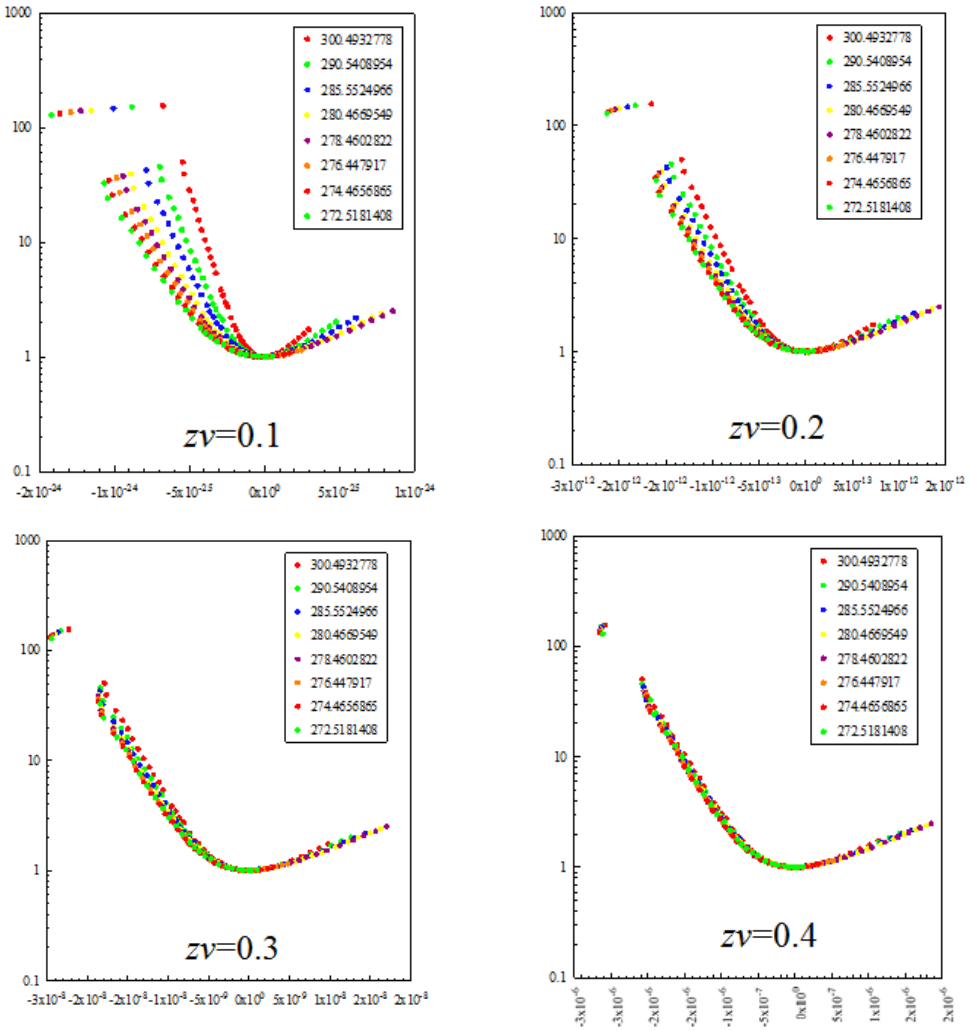


Fig. 3.3.4. Scaling plot of $R(P, T)/R_c(T)$ $(P\text{-}P_c)T^{1/zv}$.

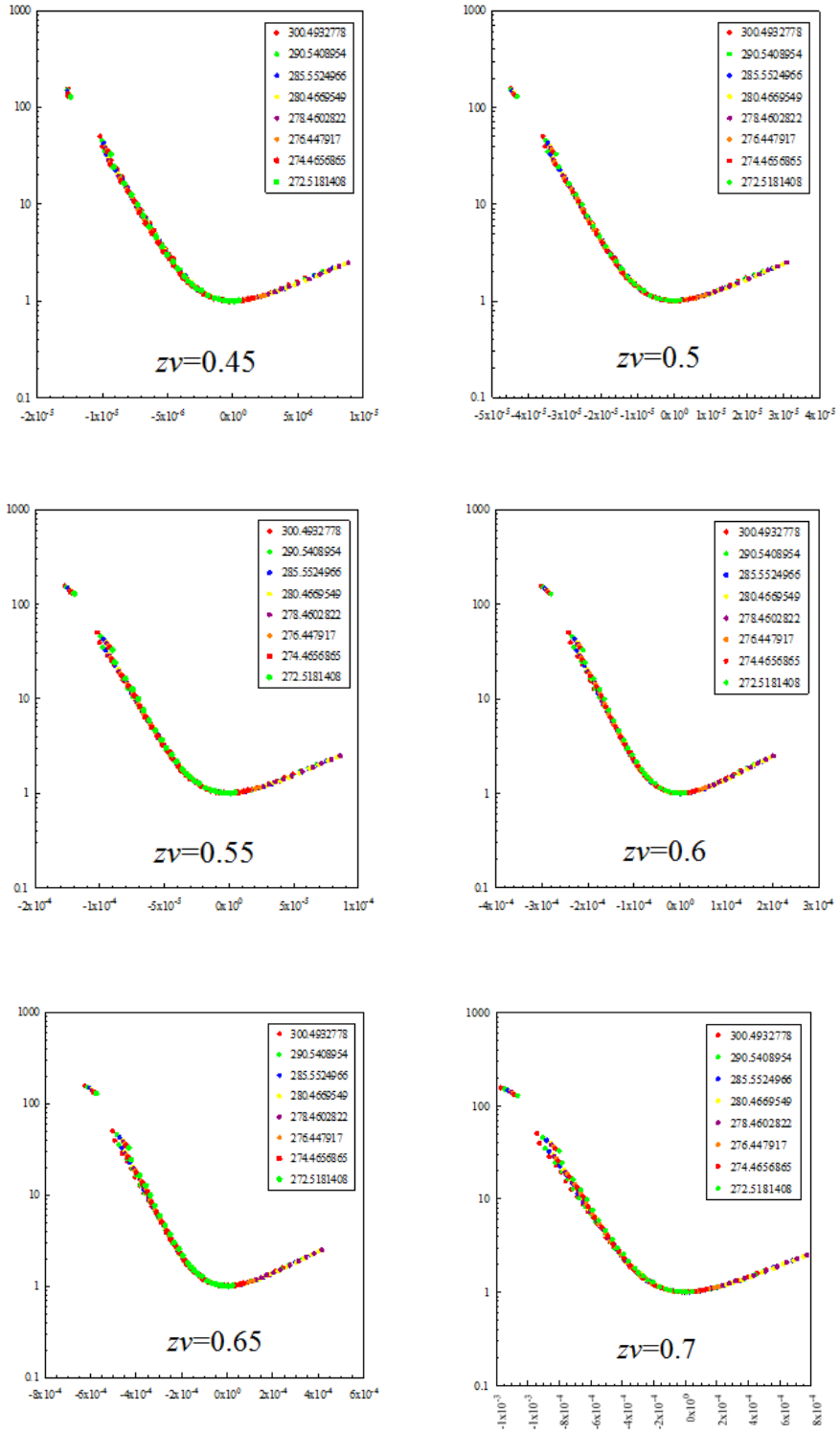


Fig. 3.3.4. Scaling plot of $R(P, T)/R_c(T)$ vs $(P\text{-}P_c)T^{1/zv}$.

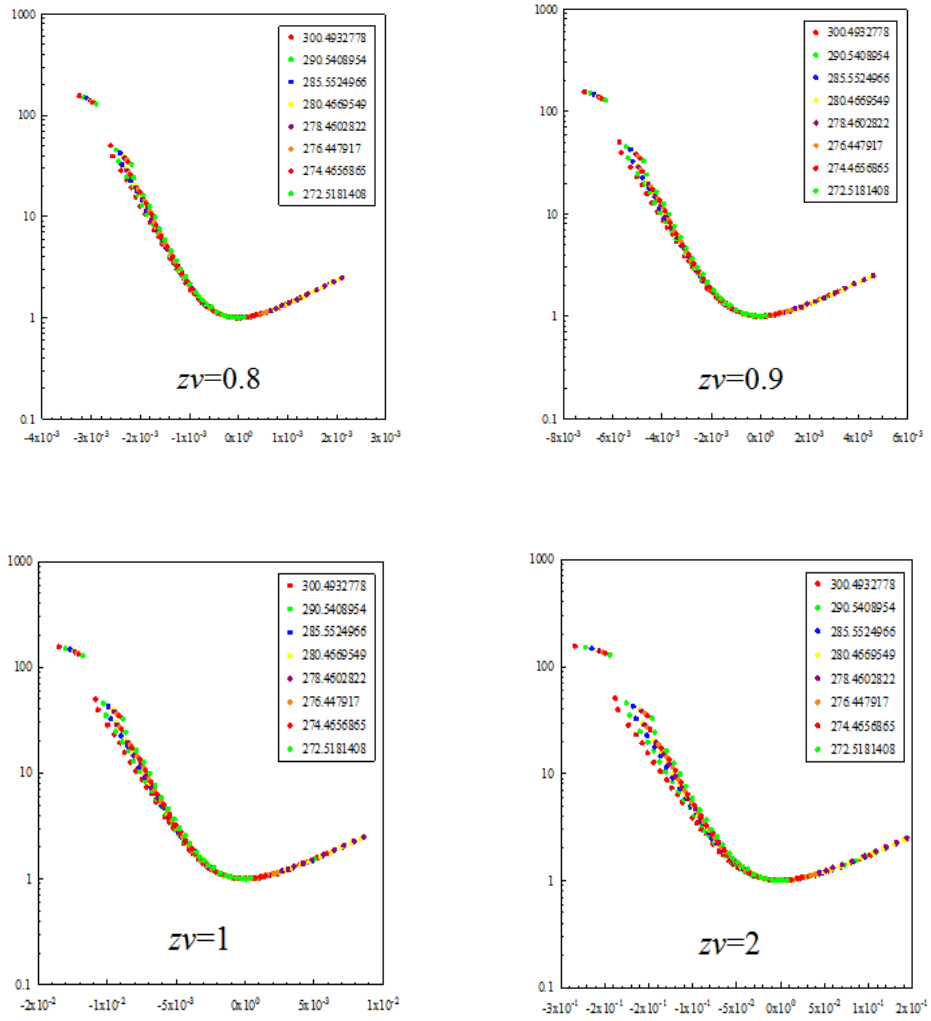


Fig. 3.3.4. Scaling plot of $R(P, T)/R_c(T)$ vs $(P\text{-}P_c)T^{-1/zv}$.

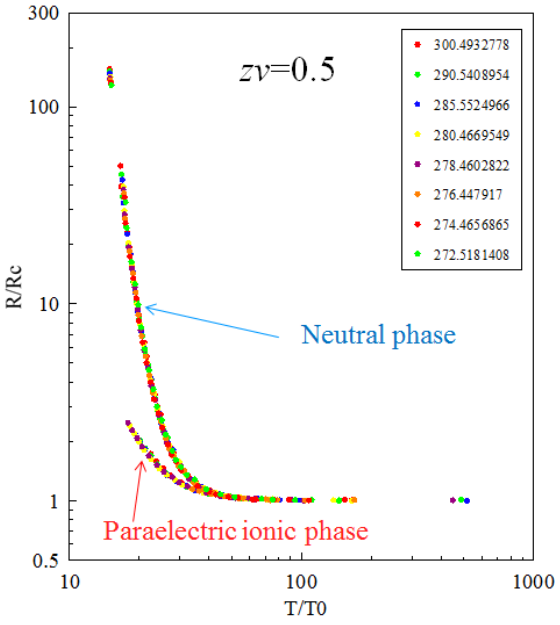


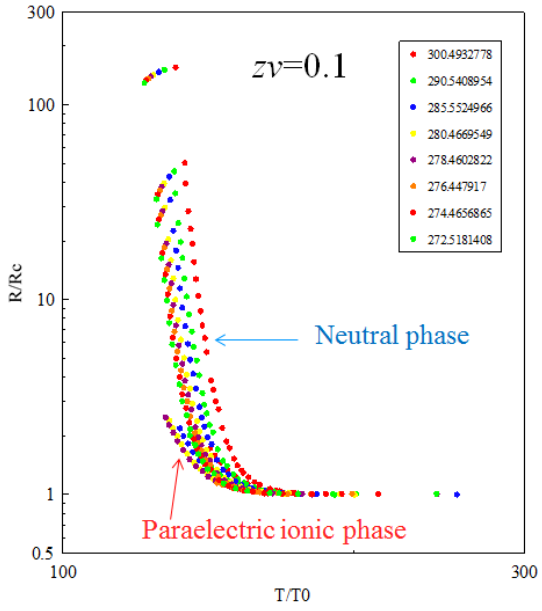


Fig. 3.3.5. Scaling plot of $R(P, T)/R_c(T)$ vs $T/T_0$ with $T_0=c(P_1-P_c)^{zv}$.

Next, the scaling analysis was attempted so as to include the ferroelectric ionic phase, as shown in Fig. 3.3.6 (a). Figs. 3.3.6 (b) and (c) shows $R(P, T)/R_c(T)$ vs $(P\text{-}P_c)T^{-1/z\nu}$ and $R(P, T)/R_c(T)$ vs $T/T_0$ , respectively. It is seen in both figures that only the curves in the ferroelectric ionic phase deviate from the scaling, indicating that the ferroelectric ionic phase can be distinguished from the neutral and paraelectric ionic phases in terms of the transport behavior.

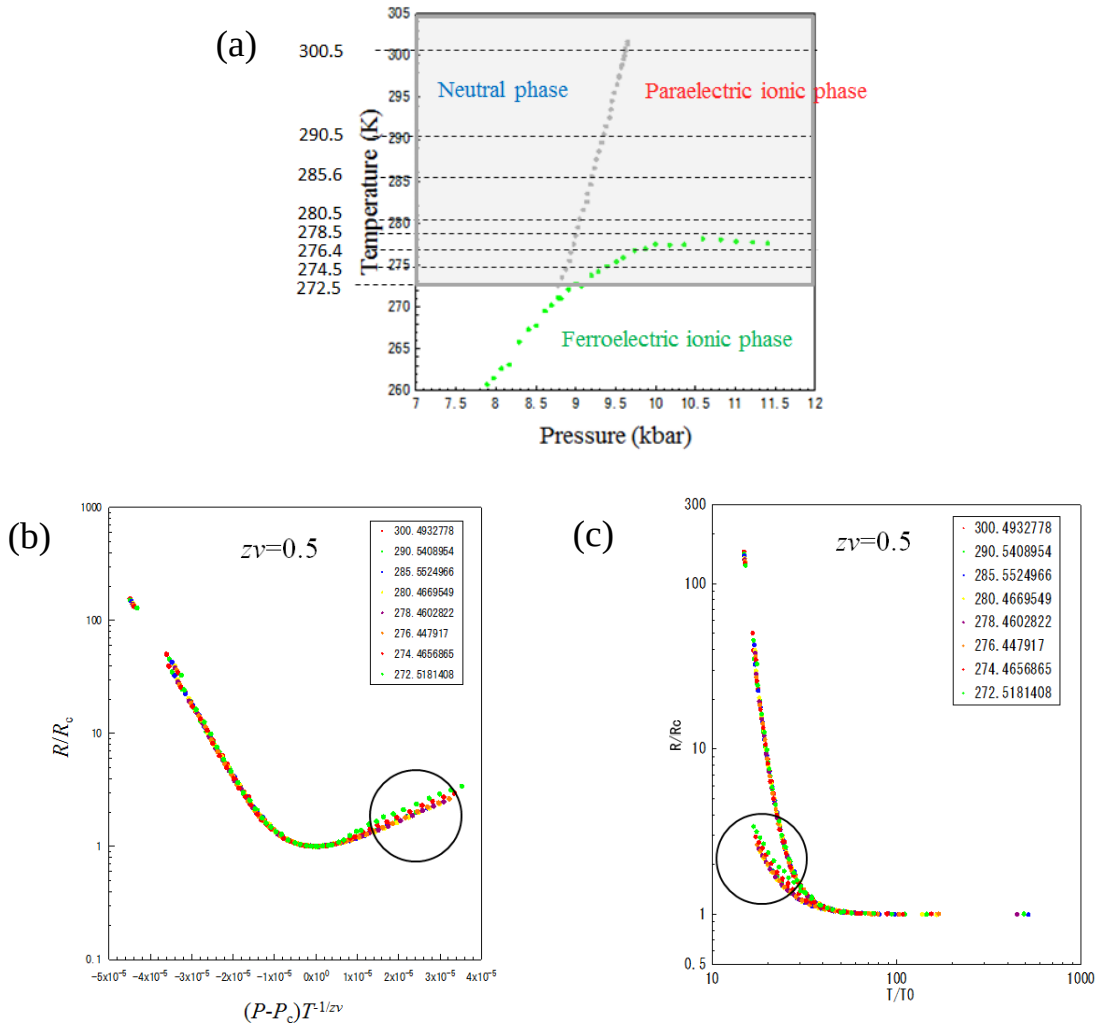


Fig. 3.3.6 (a) Measurement paths of the data used for the scaling. (b) Plot $R(P, T)/R_c(T)$ vs $(P\text{-}P_c)T^{-1/z\nu}$. (c) Plot $R(P, T)/R_c(T)$ vs $T/T_0$.

### 3.3.3 Discussion

First, we have to note that this scaling has some inconsistency with the activation behavior of the NIDWs, because physical quantities should obey power law in the quantum scaling. However, we proceed with the discussion with the activation behavior as $P_c$. As seen above, the resistivity in the NI crossover region is well scaled with $zv$ of 0.5~0.6. The successful scaling in the NI system may result from the fact that the nearest neighbor Coulomb interaction 0.6~0.7eV, which is much higher than room temperature, makes the charge fluctuation quantum critical even in the room temperature range, as in the Mott case [74]. Concerning the $zv$ value of 0.5~0.6 in the present study the critical exponent $v$ is generally over 1/2. It is probable that $z$ =1 and $v$=0.5~0.6 since, if $z$ is equal to 2 or larger, $v$ turns out to be less than 1/2. The case of $v$=0.5 means the relevance of the mean field theory, although the conductivity enhancement around the crossover region has pronounced one-dimensional feature, as shown in the previous section It is noted, however, that the temperature range available for the transport scaling in the present system is too narrow to justify the validity the quantum criticality of the NI transition and the charge-lattice coupling, which tends to make the fluctuations classical, should be considered. Thus, at present, we should take the scaling results as being only a phenomenological fulfillment with a reasonable $zv$ value.

Nevertheless, it is meaningful that the ferroelectric ionic phase is distinct from the neutral and paraelectric ionic phase in the transport scaling indicating that the charge transport in the two regimes with and without symmetry breaking is distinguished from each other; namely, quasi-particles in the former and NIDW's in the latter. Using the scaling relation, even though its fulfillment is phenomenological, one can infer the virtual behavior which the system would show without dimerization transition. Figure 3.3.7 (a) includes the extrapolation of the charge transfer Widom line into the dimerized ionic phase, where the Widom line in the non-dimeric phase is extrapolated as a linear line and Fig. 3.3.7 (b) shows the extension of the $R_c(T)$ to the dimerized ionic region. We examined the scaling of the resistivity in the orange-colored non-dimeric region in Fig. 3.3.7 (a), using the extrapolated $P_c$ and $R_c$. The results with $zv$=0.5 and 0.6 are shown in Fig. 3.3.8, which includes the data both in orange- and gray-colored regions. Noticeably, the scaling is successful even in the orange-colored region, which is separated from the virtual Widom line by a dimerized ferroelectric region. Alternatively, if the dimerization transition line (the orange-colored line in Fig. 3.3.9 (a)) and the resistivity on that are used as $P_c$ and $R_c$, the scaling fails as seen in Fig. 3.3.9 (b), which is the result for $zv$=0.5. These results indicate that the charge transfer Widom line penetrates into the ferroelectric ionic phase, although it is a virtual line; there are observed neither anomalies suggestive of the Widom line nor the critical end point in resistivity in the ferroelectric ionic phase. According to the resistivity scaling in the Mott systems, the finite-temperature critical end point influences the quantum scaling in the vicinity, where the scaling fails. In the present study, such a signature is not observed in the temperature range 240K~300K, indicating that the critical end

point of the charge transfer, if any, should be away from the temperature range studied. This consequence contradicts an earlier proposal that the charge transfer Widom line merges into the dimerization transition line at the tricritical point like the gas-liquid-solid phase diagram and the critical end point resides at a temperature above the dimerization transition.

We mention the nature of the dimerization transition here. If the system is pressurized at a fixed temperature 260K for example, the lattice dimerization occurs before reaching the charge transfer Widom line (ex. Fig. 3.3.9 (a)). This suggests that the dimerization transition in the low pressure region occurs in a low-$\rho$ region without enough Madelung energy gain for the charge transfer and concomitantly without enough paramagnetic spins. Thus, it is not compelling to regard the dimerization transition at low pressures as the simple spin-Peierls transition.

(a)

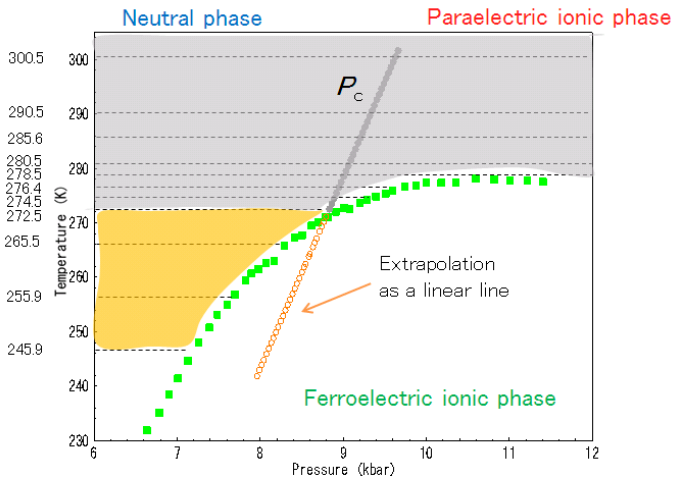


(b)

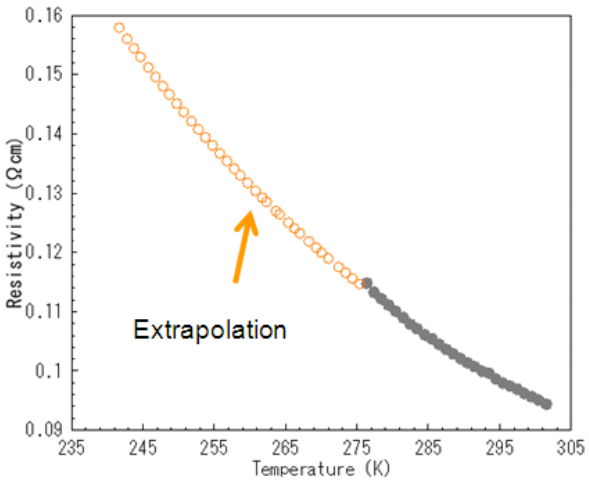


Fig. 3.3.7 (a) Extrapolation of (a) the Widom line and (b) the crossover resistivity $R_c(T)$ into the dimerized ferroelectric region.

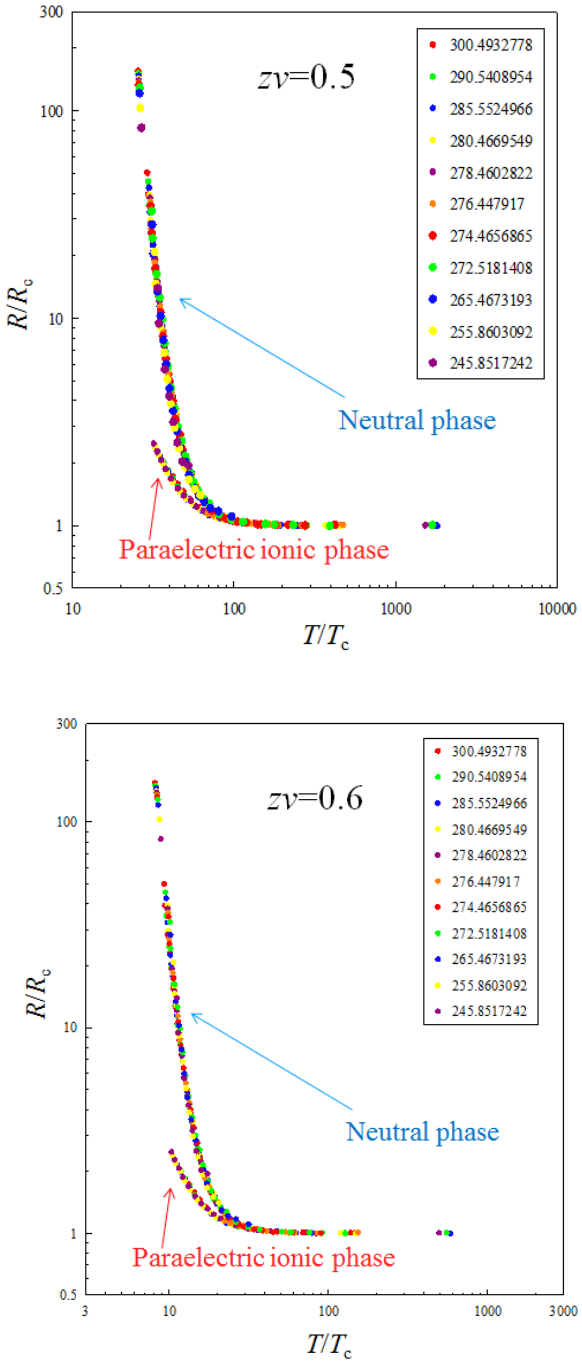


Fig. 3.3.8. Scaling plot $R(P, T)/R_c(T)$ vs $T/T_0$,.$T_0=c(P_1-P_c)^{z\nu}$, for the data in the grey- and orange-colored regions in Fig. 3.3.7 (a) with the use of the extrapolated values of. $P_c(T)$ and $R_c(T)$.

(a)

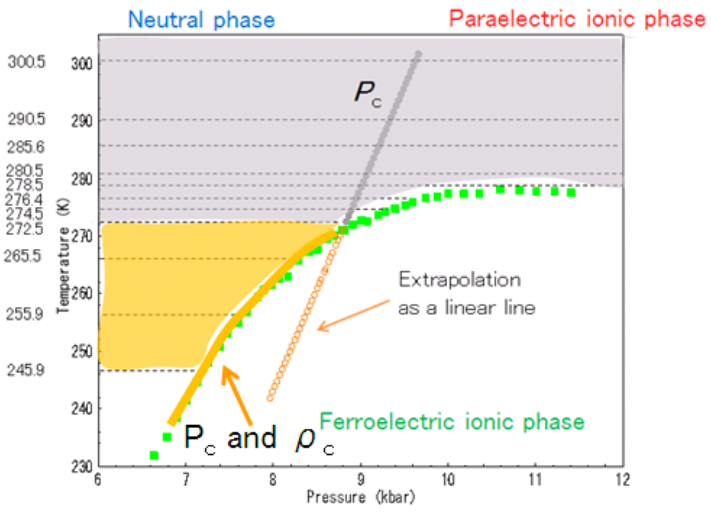


(b)

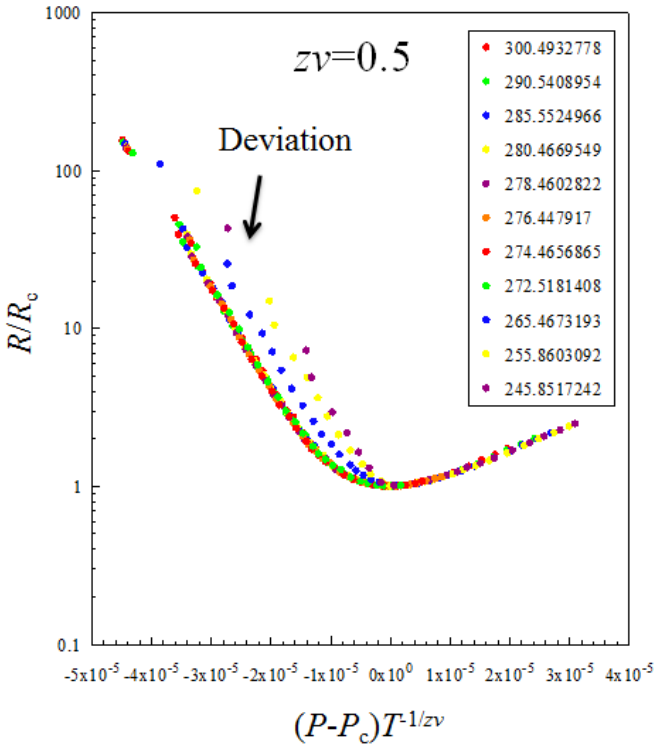


Fig. 3.3.9 (a) Phase diagram, where the orange-colored dimerization transition line tentatively adopted as $P_c(T)$ is highlighted.(b) Scaling plot $R(P, T)/R_c(T)$ vs $T/T_0$,.$T_0=c(P_1-P_c)^{zv}$, for the data in the grey- and orange-colored regions with the use of the dimerization transition line as $P_c(T)$ and the resistivity on that as $R_c(T)$.

## 3.4 Discussion on a conduction mechanism in TTF-CA

In section 3.2, we mentioned the possible existence of the NIDW excitation as carriers in the NI crossover on the basis of the experimentally determined activation energy, which is one-order-of-magnitude smaller than the one-particle excitation energy. Next, it should be made clear which the low energy excitation is, the NIDW or the LR-NIDW; as described in Chapter 1, there are two types of DW excitations in the NI system, the NIDW without dimerization and the LR-NIDW with dimerization. According to the NQR measurements, the carriers appear to be the NIDW's because the dimerization is not observed in the NI crossover [25], whereas the IR measurements detect the dimerization [9], suggestive of the LR-NIDW. The NIDW excitation energy is theoretically predicated as 0.03~0.066eV as shown in section 3.2, while the LR-NIDW excitation energy is evaluated as 0.005~0.035eV [33, 47, 52] because of lattice relaxation energy gain. The experimental result of 0.055eV is in the former range, but the both values are not so far apart as to remove the latter possibility.

Here, the previous studied on the transport mechanisms of the NIDW and the LR-NIDW are briefly reviewed because the most different points between the NIDW and the LR-NIDW appear in their transport properties [34, 46, 75]. The NIDW has an effective charge. For example, in the case of Fig. 3.4.1 (a), where an ionic domain is excited in the neutral background, electrons move to right side and charge bias, positive charge on the left side and negative charge on the right side, is generated in the ionic domain. Thus the domain has an effective charge at the boundary between the ionic and neutral molecules. The charge of the NIDWs is $\pm e/2$ in case of $\rho$=0 in the neutral state and $\rho$=1 in the ionic state. When $\rho$ takes a halfway value, the effective charge of the NIDWs is predicted to be $\pm e/2(\rho_I-\rho_N)$, where $\rho_N$ and $\rho_I$ mean $\rho$ in the neutral and ionic states, respectively. Thus, the NIDWs are particular excitations which have fractional charges. Since the NIDWs have the effective charges and are not bound as explained in section 3.2, they drift under an electric field (Fig. 3.4.1 (b)). Under a constant current, if the NIDWs reaches the end of the sample, charge cannot be carried any more (Fig. 3.4.1 (c)), but in finite temperatures new NIDWs as shown in Fig. 3.4.1 (d) can be thermally excited, and these NIDWs subsequently flow in the same way as in Figs. 3.4.1 (a), (b) and (c). There are also excitations of the NIDWs with opposite charges, but they are annihilated by the electric field. Therefore, a certain number of NIDWs, which are not annihilated by the electric field, exist in thermal equilibrium and they can be charge carriers. The LR-NIDW also has effective charges, and thus drifts by the electric field (Fig. 3.4.2 (a)). After the LR-NIDWs reach to the end of the system, however, current cannot be generated in contrast to the case of the NIDWs, since the LR-NIDWs excited in the dimerized background are all annihilated by the electric field (Fig. 3.4.2 (b)). In such a case, the excitations of spin solitons are suggested as shown in Fig. 3.4.2 (c). The spin solitons in the NI system are considered to have effective charge, and thus they can also contribute to the charge current. At the same time, in a region in between the pair of the solitons, the polarization

of the dimerization is reversed, which allows to generate the LR-NIDWs not annihilated by the electric field (Fig. 3.4.2 (d)). Therefore, in the case of the LR-NIDW, the excitations of spin solitons are required for a steady current flow.

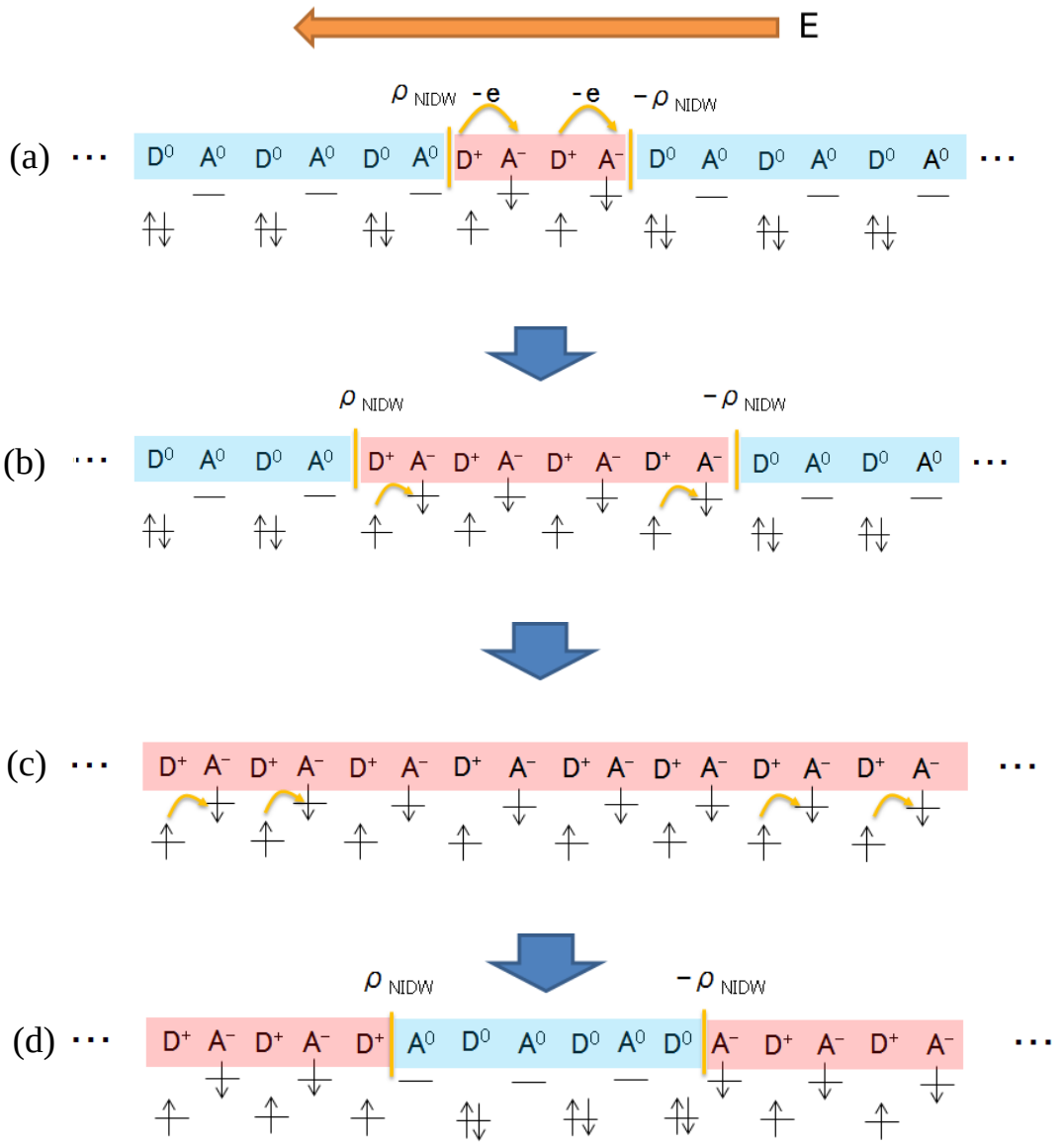


Fig. 3.4.1 (a) Excitation of the NIDWs. (b) Transport of the NIDWs. (c) The NIDWs reach the end of the sample. (d) New excitation of the NIDWs.

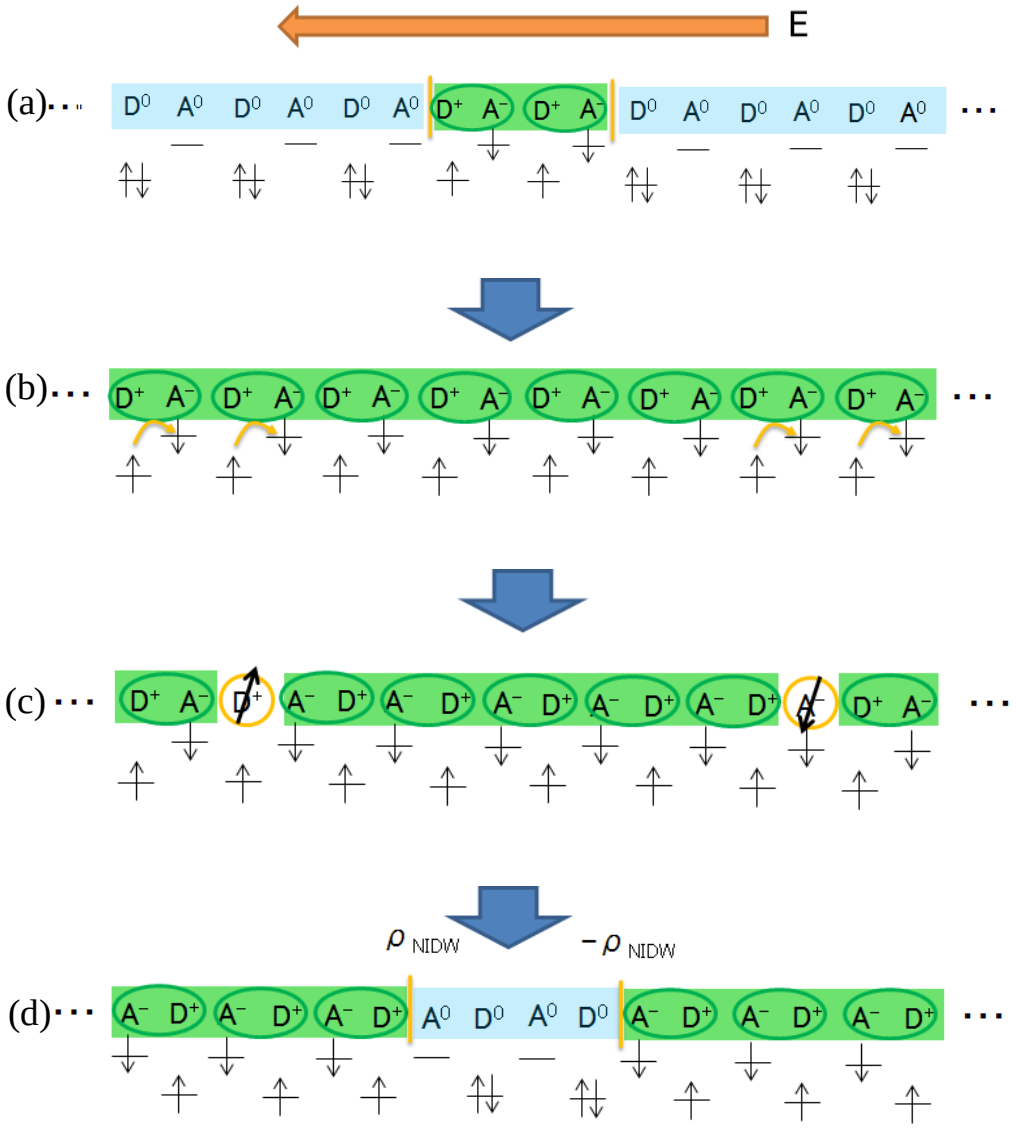


Fig. 3.4.2 (a) Excitation of the LR-NIDWs . (b) The LR-NIDWs reach the end of the sample. (c) Excitations of spin solitons. (d) New LR-NIDWs are excited.

Which DW excitations are responsible for the observed excess conduction? The scaling analysis, which shows the charge transfer Widom line penetrating into the ferroelectric ionic phase, supports the NIDW excitations. If the carriers are the LR-NIDW's, the charge transfer Widom line should not enter into the ferroelectric ionic phase. It is because the LR-NIDW is originally the excitation generated at the first order transition between the neutral and the ferroelectric ionic phases, and thus it is predicted, if the carrier is the LR-NIDW, the charge transfer Widom line should be continuously connected with the first-order dimerization transition line. On the other hand, the dimerization occurs as lattice fluctuations in the NI crossover, and we discuss effect of the dimerization in terms of the time scale of charge and lattice dynamics.

Concerning the apparent inconsistency between the NQR and the IR measurements about the dimerization, the distinct time scales of each measurement should be taken into account. In Fig. 3.4.3 (a), we show the characteristic time scales of NQR , IR and visible light experiments performed for TTF-CA; $3.7\times10^{7}$Hz [17, 25], about $1600\text{cm}^{-1}=4.8\times10^{13}$Hz (CA, $b_{1u}\nu_{10}$ mode) and about $2.5\text{eV}=6.0\times10^{14}$Hz (intramolecular excitation of TTF) [9, 16], respectively. According to the analysis of the IR and visible light data the exchange rate of the neutral and ionic state around the NI crossover at room temperature is about $50\text{cm}^{-1}=1.5\times10^{12}$Hz [9, 16]. As for the dimerization, the NQR and the IR measurements probing the dimerization have the time scales of $3.7\times10^{7}$Hz and about $1000\text{cm}^{-1}=3.0\times10^{14}$Hz (TTF $a_g\nu_4$ mode) [16], respectively, as shown in Fig. 3.4.3 (b). In contrast to the charge transfer, it is hard to determine the characteristic time of the dimerization from only these experimental results; nevertheless it is certain that it is much greater than the former but much lower than the latter. Another piece of information comes from the NQR $1/T_1$ behavior as shown in Fig. 3.4.4. The $1/T_1$ is enhanced under the pressure with a maximum at approximately 11kbar, indicating the development of the fluctuation of the dimerization since $1/T_1$ is a measure of the fluctuation of the order of MHz. The lattice fluctuation makes it difficult to distinguish the NIDWs from the LR-NIDWs, because the NIDWs are slowly transformed to the LR-NIDWs with lattice fluctuation time scale. On the basis of these results, we postulate the NIDW motion as shown in Fig. 3.4.5; the NIDWs are excited and move in an electric field independently from the dimerization. Owing to the thermal fluctuation, the excitation always occurs anywhere in the system, and sometimes the NIDWs with opposite charge annihilate. After a while, the dimerization occurs as a much slower process and forms the LR-NIDWs, and it returns to the NIDWs in the lattice fluctuation time. These processes with different time scales are going on as thermal fluctuations. If both time scales are faster than the NQR frequency, NQR sees the averaged $\rho$ and no dimerization.

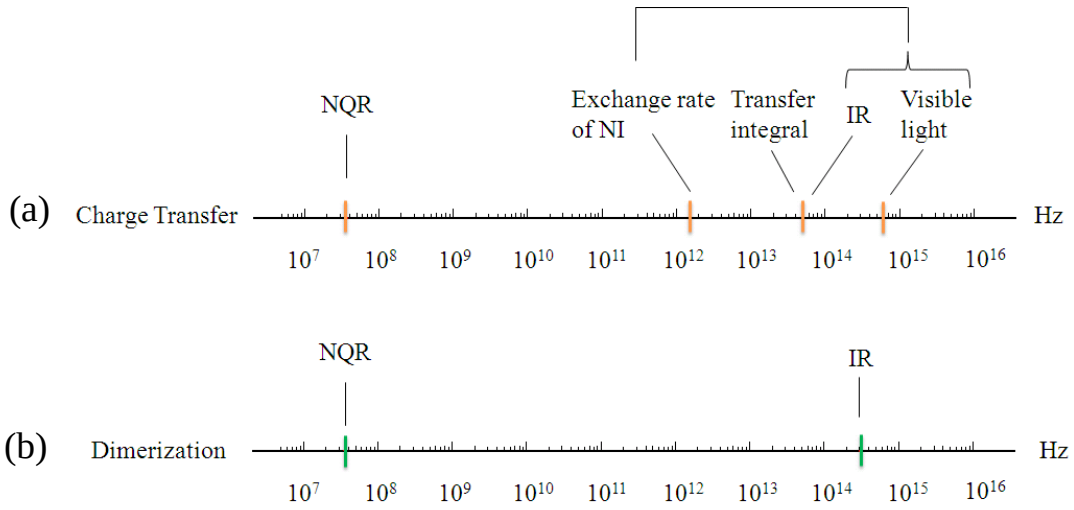


Fig. 3.4.3 (a) Time scale of experimental probes of the charge transfer. The charge transfer rate extracted experimentally and the inverse of the band width are also indicated. (b) Time scale of experimental probes of the dimerization.

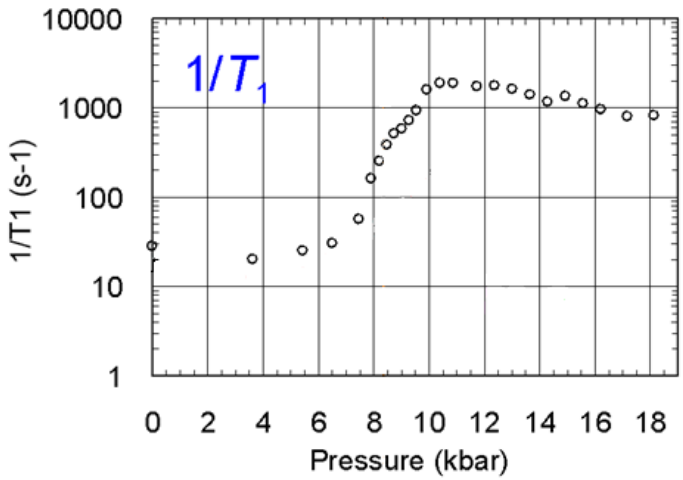


Fig. 3.4.4. Pressure dependence of $1/T_1$ of $^{35}$Cl NQR.

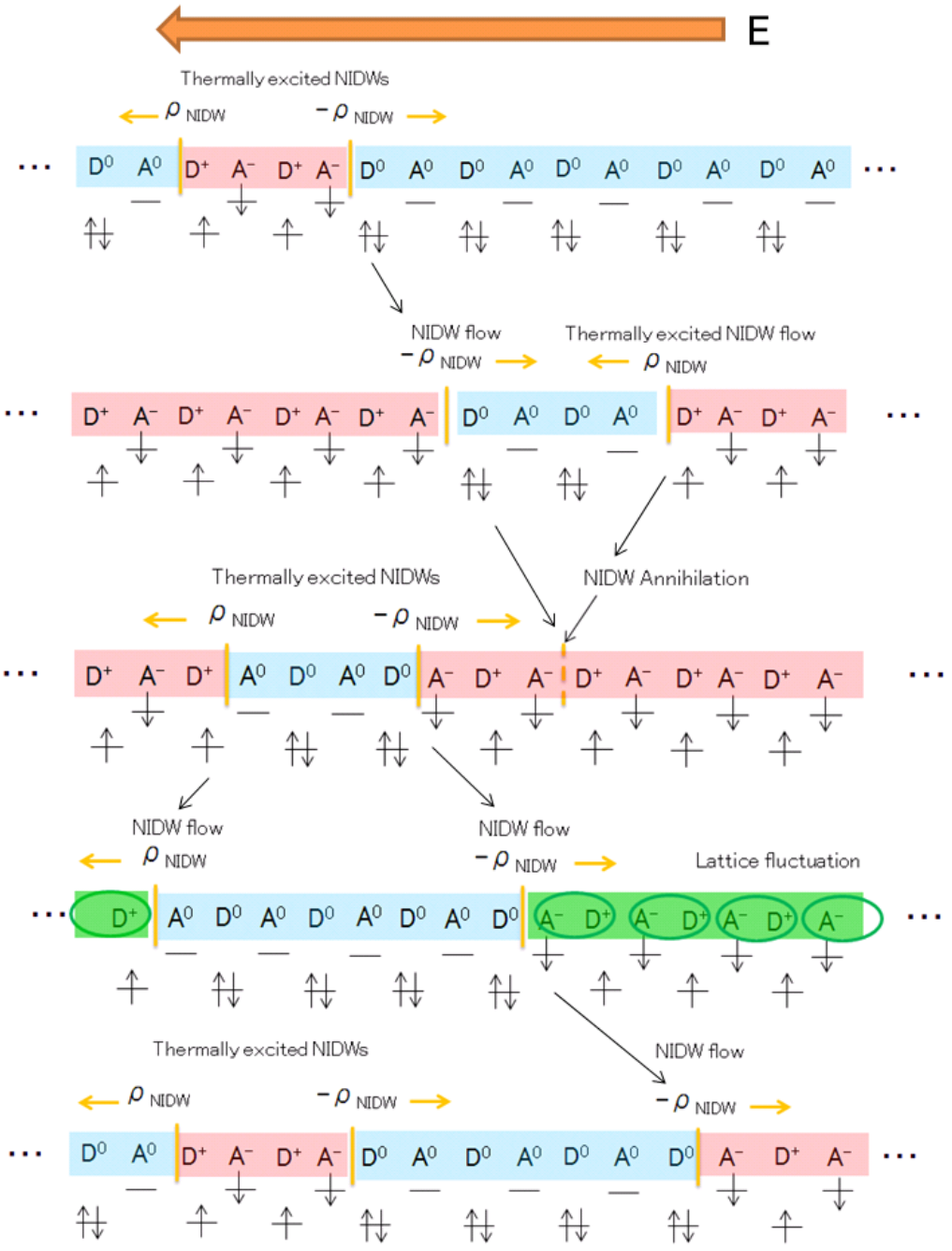


Fig. 3.4.5. Transport of the NIDWs.

NMR provides additional and distinctive information on the presence of the non-dimerized ionic molecules. If the system had only the neutral and the dimerized ionic molecules, the NMR measurements would not detect any spins. Figures. 3.4.6 (a) and (b) show the previous results of $^1$H NMR $1/T_1$ described in Chapter 1 [55]. The results show that $1/T_1$ is enhanced exponentially with increasing pressure. Such a drastic increase of $1/T_1$ indicates a progressive increase of the spin population by pressure. Comparing Figs. 3.4.6 (b) and (c) [9], it seen that the increases in $1/T_1$ and the fractions of ionic molecules go parallel to each other, strongly suggesting the generation of the paraelectric ionic molecules with spins. There is another possibility that $1/T_1$ detects the spin solitons. Although we cannot make a definite discussion on which mainly contributes to $1/T_1$, the similarity of Figs.3.4.6 (b) and (c) are suggestive of the primary role of the ionic molecules rather than solitons.

On the basis of this interpretation, the number of the spins corresponds to the number of the paraelectric ionic molecules, which is theoretically dealt with by the one-dimensional antiferromagnetic XXZ model. Below, we argue the $1/T_1$ data in terms of this model.

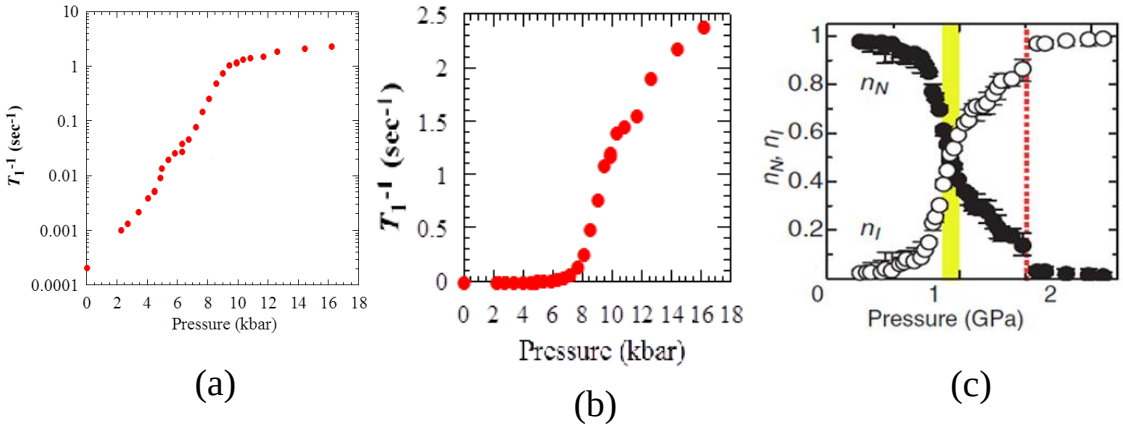


Fig. 3.4.6 Pressure dependence of $^1$H NMR $1/T_1$ in (a) a logarithmic scale and (b) linear scale [55]. (c) Pressure dependence of the relative populations of the ionic and neutral.molecules deduced by the IR and visible light measurements [9].

First we relate $1/T_1$ to the fraction of the paraelectric ionic molecules, *n*. Assuming the localized spins, $1/T_1$ is represented in the following,

$$\frac{1}{T_1} = \frac{\sqrt{2\pi} g^2 \gamma_n^2 A^2}{3\omega_e}, \qquad \omega_e^2 = \frac{8zJ^2 S(S+1)}{3\hbar^2}.$$

where $g$ is the g-factor, $\gamma_n$ is the gyromagnetic ratio, $A$ is the hyper fine field tensor, $z$ is the number of adjacent sites, $J$ is the exchange interaction with the nearest neighbor electron spins and $\hbar$ is the Planck constant divided by $2\pi$[24]. In this formula, the unknown parameters are $A$ and $J$. The formula also can be written

$$\frac{1}{T_1} = c\frac{A^2}{J}n$$

or

$$\frac{1}{T_1} = c\frac{A^2}{J}n^2$$

where $n$ is the ratio of the ionic molecules. We regard $A$ and $J$ as constants, because amount of change of $A$ and $J$ cannot explain the exponential change of $1/T_1$, though in fact $A$ and $J$ must change under pressure. A constant $cA^2/J$ is determined by using proportional relation between $1/T_1$ and $n$ or $n^2$ at 8.55kbar. There are two regimes for relating $1/T_1$ to $n$; in case that the spins move more slowly than the NMR frequency, $1/T_1$ is proportional to $n$, whereas, in the case the spins move faster than the NMR frequency, $1/T_1$ is proportional to $n^2$ because the nuclear spins feel the averaged hyperfine field of $an$, where $a$ is a hyperfine field for one $\mu_B$ on a molecule. Then, $A \propto$ an and $1/T_1 \propto A^2 \propto n^2$. Figures. 3.4.7 (a) and (b) show the pressure dependence of $n$ for each case.

(a)

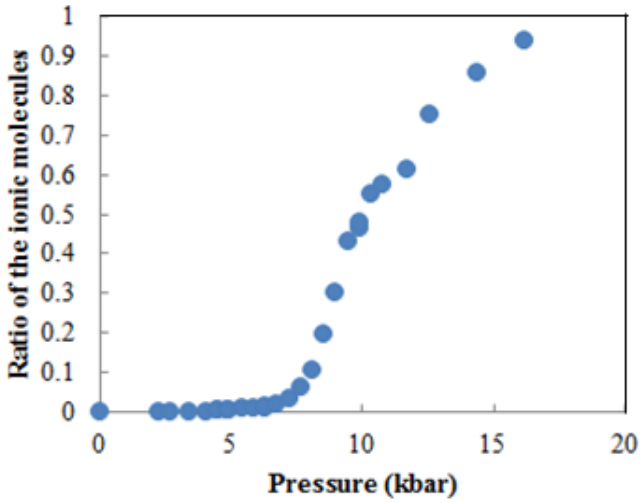


(b)

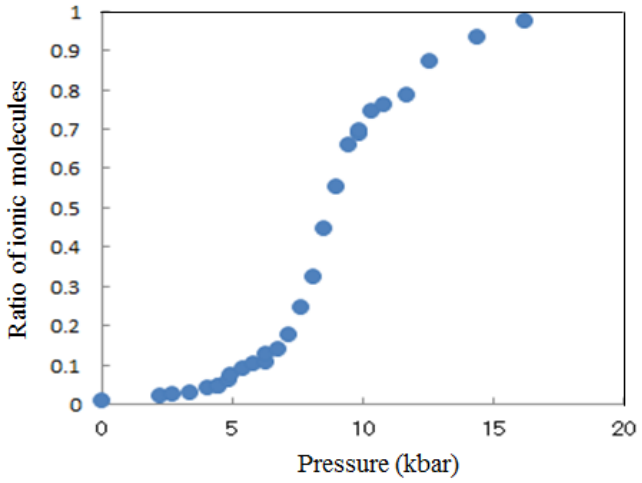


Fig. 3.4.7 Pressure dependence of the fraction of the ionic molecules $n$, which is assumed to be (a) $n \propto 1/T_1$ and (b) $n \propto (1/T_1)^{1/2}$.

The one-dimensional antiferromagnetic XXZ model is described in the following [76],

$$H = \left(\frac{I_D - E_A - 2V}{2}\right)\sum_{l=1}^{N}(-1)^l S_l^z + V\sum_{l=1}^{N} S_l^z S_{l+1}^z - 2t\sum_{l=1}^{N}(S_l^x S_{l+1}^x + S_l^y S_{l+1}^y).$$

In this model, a neutral donor (acceptor) molecule is represented by a down (up) spin, while an ionic donor (acceptor) molecules is represented by an up (down) spin, as shown in Fig. 3.4.8.

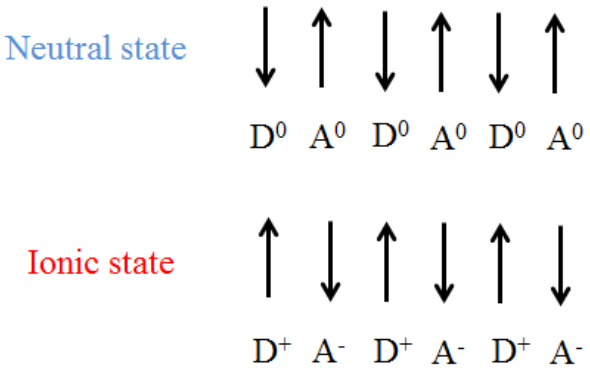


Fig. 3.4.8. Correspondence between the neutral/ionic states and the spin representation in the one-dimensional antiferromagnetic XXZ model.

This Hamiltonian cannot be dealt with directly for the present analysis. However, the Hamiltonian holds a DW picture [76], and thus we assume that $V$ and $t$ are squeezed to $J_{DW} = E_{DW}/2$, where $J_{DW}$ is the effective nearest neighbor Coulomb interaction. Consequently, the Hamiltonian is approximated to the classical antiferromagnetic Ising model,

$$H = \left(\frac{I_D - E_A - 2V}{2}\right)\sum_{l=1}^{N}(-1)^l S_l^z + J_{DW}\sum_{l=1}^{N} S_l^z S_{l+1}^z,$$

Furthermore the classical antiferromagnetic Ising model is converted to the classical ferromagnetic Ising model,

$$H = -\left(\frac{2V - I_D + E_A}{4}\right)\sum_{l=1}^{N}\sigma_l^z - J_{DW}\sum_{l=1}^{N}\sigma_l^z\,\sigma_{l+1}^z,$$

where the external field $h$=(2$V$-$I_D$-$E_A$)/4.

This can be solved, and the solution is converted to the expected value <$n$>, where $n$ is the number of the paraelectric ionic molecules. It is

$$\langle n\rangle = \frac{1}{2}\left(1 + \frac{sinh\frac{h}{k_BT}}{\sqrt{sinh^2\frac{h}{k_BT} + e^{-4\frac{J_{DW}}{k_BT}}}}\right)$$

We fitted this form to the experimental $n$ profile by two methods; in the first one, $h$ and $J_{DW}$ are used as parameters and $h$ is assumed to be a quadratic function because the change of the Madelung energy against pressure can be approximated by a quadratic function with four parameters. The fitting to the data of $n \propto (1/T_1)^{1/2}$ is shown in Fig. 3.4.9 (a). The other fitting includes three parameters, $V$ of ambient pressure, $I_D$-$E_A$ and $J_{DW}$, assuming that only $V$ is varied by pressure; the pressure dependence of $V$ is explained in section 3.2. The result of the fitting to the data of $n \propto (1/T_1)^{1/2}$.is shown in Fig. 3.4.9 (b).

(a)

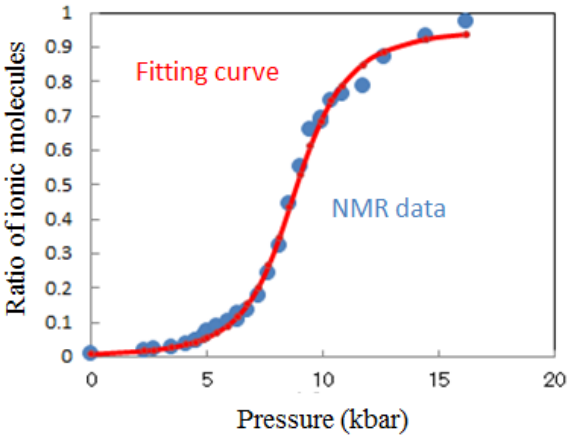


(b)

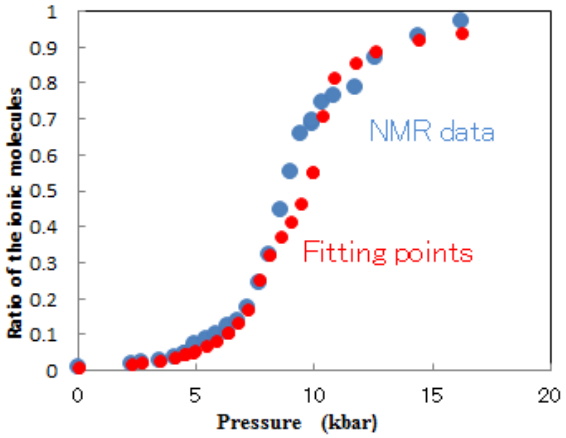


Fig. 3.4.9 (a) Fitting of the XZZ model to the experimental data (a) with $h$ and $J_{DW}$ as parameters and $h$ assumed to be a quadratic function, and (b) with $V$, $I_D$-$E_A$ and $J_{DW.}$ as fitting parameters.

Overall, both fittings in Figs. 3.4.9 (a) and (b) are successful. The fitting shown in Fig. 3.4.9 (a), yields $J_{DW}$~0.05eV was obtained, and consequently $E_{DW}$~0.1eV is deduced. The fitting in Fig. 3.4.9 (b) gives $J_{DW}$~0.035eV and consequently $E_{DW}$~0.07eV and the values of $V$ and $I_D$-$E_A$ are also estimated at 0.66eV and 0.136eV, respectively. The values of $E_{DW}$ are of the same order as the experimental value $E_{DW}$=0.055eV, though there is a little difference. The value of $V$ is in the expected range, since $V$ should be approximately equal to the CT energy, 0.6~0.7eV [42]. It is noted that the above fittings have the following problems; the theory doesn't take the three-dimensionality into account, and assumes no finite temperature critical end point. Nevertheless, the successful fittings suggest that the one-dimensional Ising model can approximately explain the NMR results. The fitting also explains the activation energy observed in resistivity around the NI crossover, where generally the activation energy should not be observed. Only in the case of the one-dimensional Ising model, the correlation length develops exponentially with the temperature decreased along the crossover line under the condition of $E/k_BT>1$. Thus, the number of the DWs, which is given by the inverse of the correlation length, also develops exponentially. Therefore, the conductivity, which is proportional to the number of the NIDWs, shows the activation type of behavior.

Finally, we mention characteristic behavior of resistivity of TTF-CA (Fig. 3.1.3) on the basis of the discussion so far. First, the resistivity shows a minimum value of approximately 0.1Ωcm (Fig. 3.1.1), and we explain it by the number of the NIDWs. In the case of the one-dimensional Ising model, the number of the NIDWs can be calculated so that the free energy of the NI system becomes a minimum. The free energy is described in the following,

$$F(T, n_{DW}) = n_{DW}E_{DW} - TS\big(n_{DW}(T)\big),$$

where $n_{DW}$ is the number of the NIDWs. $F(T,n_{DW})$ is the approximate free energy in a one-dimensional chain of the NI system, which does not include the LR-NIDWs by the lattice fluctuation for simplicity. The state of the system is determined so that the free energy takes a minimum,

$$\frac{\partial F}{\partial n_{DW}} = 0.$$

As a result,

$$\frac{n_{DW}}{N} = \frac{1}{e^{\frac{E_{DW}}{k_BT}} + 1}$$

is obtained, where $N$ is the number of sites in the one-dimensional system. By using this equation,

$$\frac{N}{n_{DW}} \cong 9.25 \cong 4\sim5\ DA\ pairs$$

can be obtained. This indicates that one NIDW exists per 4~5 DA pairs and the number of the NIDWs are estimated at $2.61\times10^{20}$cm$^{-3}$ at room temperature. For example, in the quasi-one-dimensional organic metal $(TMTSF)_2PF_6$, carrier density $1.4\times10^{21}$cm$^{-3}$ provides 0.0015Ωcm (**a** axis), 0.15Ωcm (**b** axis), and 30Ωcm (**c** axis) at room temperature [79, 80]. Therefore, though there are some ambiguities about mobility, $2.61\times10^{20}$cm$^{-3}$ of the NIDWs is speculated to explain the resistivity value 0.1Ωcm.

Finally, turning Fig. 3.2.8 (b) back to (a), we can obtain temperature dependence of the activation energy with pressure fixed, for example, the results at 8.1kbar are shown in Figs. 3.4.10 (a). $\exp(E_{DW}/k_BT)$, corresponding to the resistivity, can be also estimated in Figs. 3.4.10 (b). Consequently, we can interpret the metallic behavior of the resistivity (Fig. 3.1.3 (a) and (b)) as temperature dependence of the activation energy of the NIDWs.

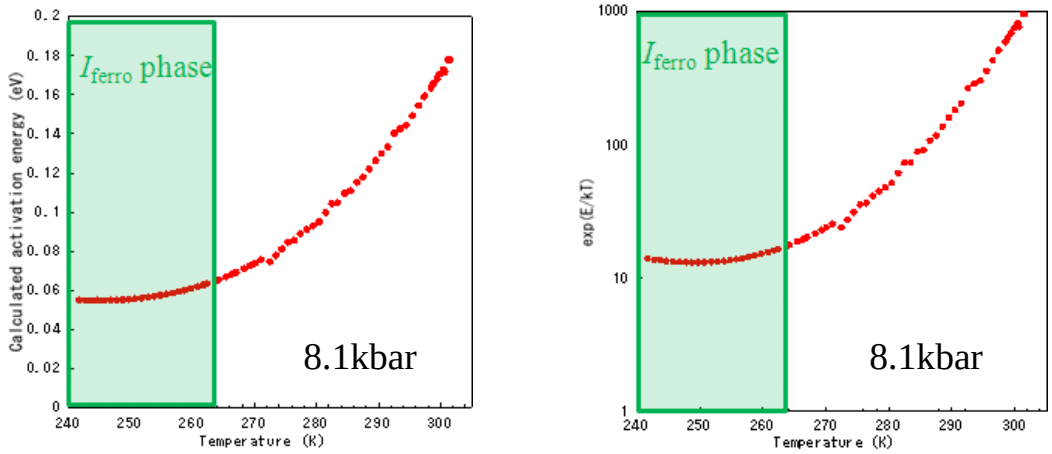


(a) (b)

Fig. 3.4.10. A region masked in green indicates the $I_{ferro}$ phase. (a) Calculated temperature dependence of the activation energy at 8.1kbar. (b) Calculated temperature dependence of $\exp(E_{DW}/k_BT)$ at 8.1kbar.

## 3.5 Summary

We have investigated the phase diagram of TTF-CA by four-terminal electric resistivity measurements under pressure. Although the phases at pressures below 9kbar had been well understood, the phases at higher pressures was not settled; in particular, it has been controversial whether an ionic phase without dimerization is extended in a vast range of pressure-temperature region. We found anomalies in the resistivity nearby the temperatures where NQR previously indicated the symmetry breaking due to the donor-acceptor dimerization in the phase diagram, consistent with the existence of the paraelectric ionic phase. The NI crossover region, where the charge transfer occurs without the lattice dimerization, was clearly identified.

Although the NI crossover occurs between two insulator phases, our four-terminal measurements showed a sharp resistivity minimum with the value of as low as 0.1Ωcm on the crossover, which cannot be explained with the conventional band picture, suggesting the NIDW conduction. To further explore the possible NIDW excitations, we examined the anisotropy of electrical conduction and found the conductivity highly one-dimensional around the NI crossover, indicating that the charge carriers responsible for the charge transport around the crossover possess extraordinarily high one-dimensional nature. Furthermore, we carried out the detailed resistivity measurements under accurately controlled and determined pressures with Manganin wires mounted in a pressure cell for sensing pressure precisely. The measurements yielded small activation energy 0.055eV in the NI crossover. The absolute value of the activation energy and pressure dependence of the activation energy is consistent with a theoretical prediction of the NIDWs as well as the highly one-dimensional nature. The possibility of the LR-NIDW with the lattice dimerization is not ruled out.

Before going to further discussion on the NIDWs, we performed scaling analysis around the NI crossover region. A form of quantum scaling relevant to the zero-temperature critical end point, which has been successfully applied to organic Mott systems, was employed. As a result, the scaling around the NI crossover was successful, and the ferroelectric ionic phase was found to show conducting behavior deviating from the scaling. Furthermore, the scaling analysis shows that the NI boundary, namely, charge transfer Widom line approaches the ferroelectric ionic phase in such a way as to crosses the ferroelectric transition (dimerization) line, not merge unto it, indicating that the critical end point does not exist in temperature range above the dimerization transition and is possibly masked by the dimerization transition.

On the basis of the scaling results, we propose the NIDW excitations as the charge carriers. The lattice dimerization can exist as fluctuation in the NI crossover, as the enhancement of NQR $1/T_1$ and the LR-NIDW and spin solitons may exist in the NI crossover. We also analyzed the previously reported NMR $1/T_1$ results, which can be a measure of the number of the paraelectric ionic molecules with spins. We showed that the one-dimensional Ising model can explain the NMR results,

which answer why the activation behavior can be observed in the NI crossover. We also estimated the number of the NIDWs at room temperature at $2.61\times10^{20}/cm^3$, which is consistent with the extremely small resistivity in the NI crossover. In addition, we show that temperature dependence of the activation energy can explain the seemingly metallic behavior in resistivity.

# Chapter 4 Metallization of the NI materials

There are no metallic compounds among the NI materials. Another purpose of the present study is the metallization of the NI materials. In the present study, we employed three methods for this purpose. One is application of extremely high pressures up to 82.5kbar, aiming at increasing the transfer integrals, which is a straightforward way for highly compressible organic materials, as described in section 4.1. Another is to apply uniaxial pressures to the particular crystallographic directions, which varies the structural and electronic anisotropies, leading to the possible control of the mixed/segregated-stack natures, as described in section 4.2, and dimensionality. The third is a choice of a two-dimensional ionic material, $M_2P$-$TCNQF_4$, which has an intermediate structure between the mixed- and segregated-stacks, as shown in section 4.3. Especially, we conducted the experiments described in this chapter in the light of the dimensional control of electronic states. Section 4.4 summarizes this chapter.

## 4.1 Electric resistivity measurements under cubic anvil pressure

In many cases, organic insulators undergo transitions to metals by hydrostatic pressure, since organic materials are so flexible that their lattice constants are easily contracted, leading to a remarkable increase in transfer integrals between molecules. However, TTF-CA doesn't become a metal even at high pressures up to 35kbar (Fig. 3.1.10), and thus higher pressures are required for the metallization. In the present study, we used the cubic anvil to pressurize the sample up to 82.5kbar, and measured resistivity to probe the electronic state.

### 4.1.1 Results

Fig. 4.1.1 shows the pressure dependence of resistivity of TTF-CA along the **a** axis at room temperature up to 82.5kbar. The results below 40kbar reproduced the behavior obtained with use of the piston-cylinder cramp-type cell as described in Fig. 3.1.1; namely, a drastic reduction, a formation of a broad minimum, and turnabout to an increase, followed by a leveling-off above 20kbar against pressure increase. It is noted that the pressure giving the resistivity minimum in the cubic anvil measurements is somewhat different from that obtained with the crump-type cell. This is, because the pressure of the cubic anvil system is not accurately measured in a low pressure region below 20kbar. As shown in Fig. 4.1.1, the resistivity is insensitive to pressure up to as high as 82.5kbar. This behavior of the paraelectric ionic phase at high pressures is in a sharp contrast to the behavior of the neutral phase. Figure 4.1.2 shows the temperature dependence of resistivity at four pressures, 20kbar, 40kbar, 60kbar, and 82.5kbar indicated by colored arrows in Fig. 4.1.1. It is obvious that no metallic behavior of resistivity is observed up to 82.5kbar. At 20kbar and 40kbar, the

behavior is not activation-like in a temperature region of 100~150K. We have no clear idea for explaining this, but the effect of the Jule heating is not ruled out. At 60kbar and 82.5kbar, the absolute values of the resistivity in temperature region below 150K are a little decreased.

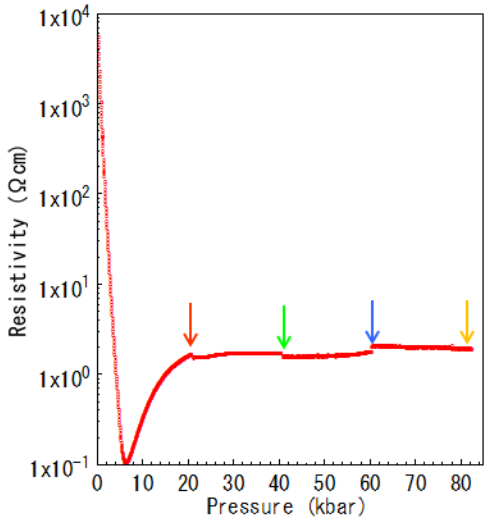


Fig. 4.1.1. Pressure dependence of the electric resistivity of TTF-CA along the **a** axis, measured with the use of the cubic anvil.

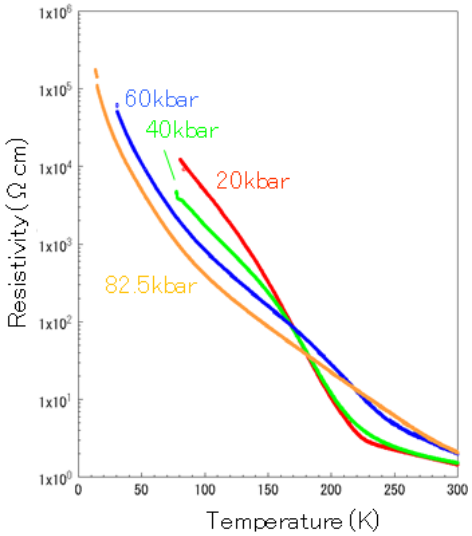


Fig. 4.1.2. Temperature dependence of the electric resistivity of TTF-CA along the **a** axis.measured with the use of the cubic anvil.

To examine the conduction mechanisms in the paraelectric and ferroelectric ionic phases, we also measured the resistivity along the **b** and **c** axes. The results around 27kbar are shown in Figs. 4.1.3, where vertical line at 216K is determined with the **a** axis results as explained in section 3.1. Since the measurements along the **a**, **b**, and **c** axes were not simultaneously performed, the pressure values of each measurement are somewhat different. The resistivity is insulating in all the directions. Fig. 4.1.4 show the activation plots of the resistivity along the three axes around 27kbar and 35kbar, where the resistivity curves are shifted so that the data at 143K are coincident around each pressure 27kbar and 35kbar. We confirm in the two pressure region that resistivity show activation behavior with the same activation energy for all three directions reasonably in the ferroelectric ionic phase. The conductivity in the paraelectric ionic phase also appears to be of activation type; however, the activation energy characterized by the slope is appreciably different between the data for the three axes. The activation plots along **a** axis at 5.1kbar, 8.2kbar, and 27kbar, where each pressure corresponds to the regions I~III in Fig. 3.1.3, respectively, are shown in Fig. 4.1.5 (a). In the region I and II, the activation energy is estimated in the temperature range of 140~170K, and in the region III, it is estimated in the range of 135~210K. The pressure dependence of the activation energies for the **a** axis direction in the ferroelectric ionic phase is shown in Figs. 4.1.5 (b). The activation energy monotonously decrease from 0.26eV to 0.19eV with increasing pressure up to 10kbar, and are nearly constant around 0.19eV for pressures above 10kbar. Small variation in the activation energy values is derived from sample dependence, because we used three samples for the resistivity measurements. Also shown in this figure is the activation energy of the $^{1}$H-NMR relaxation rate $1/T_1$ in the ferroelectric ionic phase, measured by T. Nishikawa [55]. The activation energies of $1/T_1$ are smaller than those of the resistivity; nevertheless, their pressure profile is similar to each other. Fig. 4.1.5 (c) shows the activation energies of resistivity in the paraelectric ionic phase against pressure. They are apparently dependent on the direction and are small compared with the values in the ferroelectric phase especially for the **a** axis direction; *e.g.*, it is 0.05eV at 34.6kbar, indicating that the low-lying carrier excitations contribute to the relatively high conductivity in the paraelectric ionic phase.

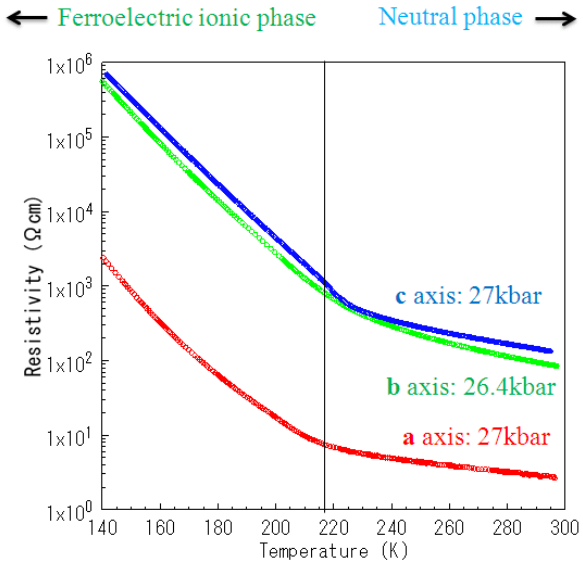


Fig. 4.1.3. Temperature dependence of the electric resistivity along **a**, **b**, and **c** axes at 27kbar 26.4kbar, and 27kbar, respectively. The vertical line lying at 216K shows the dimerization transition temperature estimated from the axis resistivity (section 3.1).

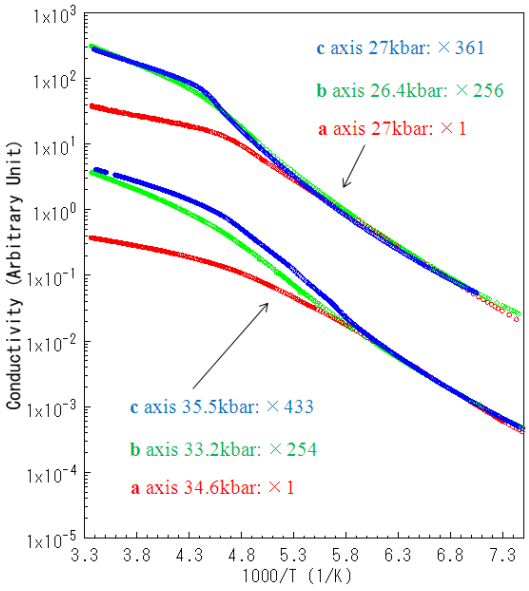


Fig. 4.1.4. Activation plot of the electric resistivity. Upper three curves: **a** axis at 27kbar, **b** axis at 26.4kbar, and **c** axis at 27kbar. Lower three curves: **a** axis at 34.6kbar, **b** axis at 33.2kbar, and **c** axis at 35.5kbar. The resistivity curves are shifted so that the data at 143K are coincident around each pressure 27kbar and 35kbar.

(a)

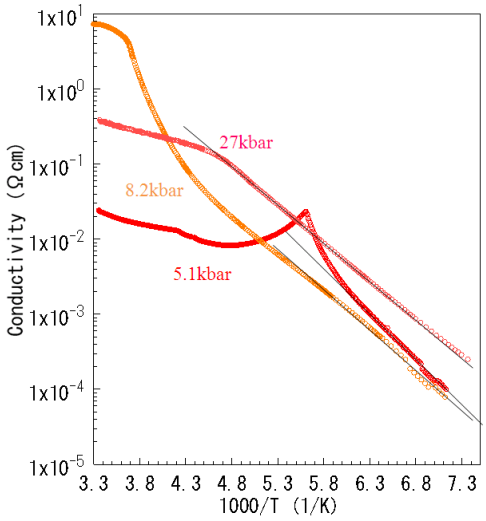


Fig. 4.1.5. (a) Activation plots of the resistivity along **a** axis at 5.1kbar, 8.2kbar, and 27kbar, corresponding to the regions I~III in Fig. 3.1.3, respectively.

(b) (c)

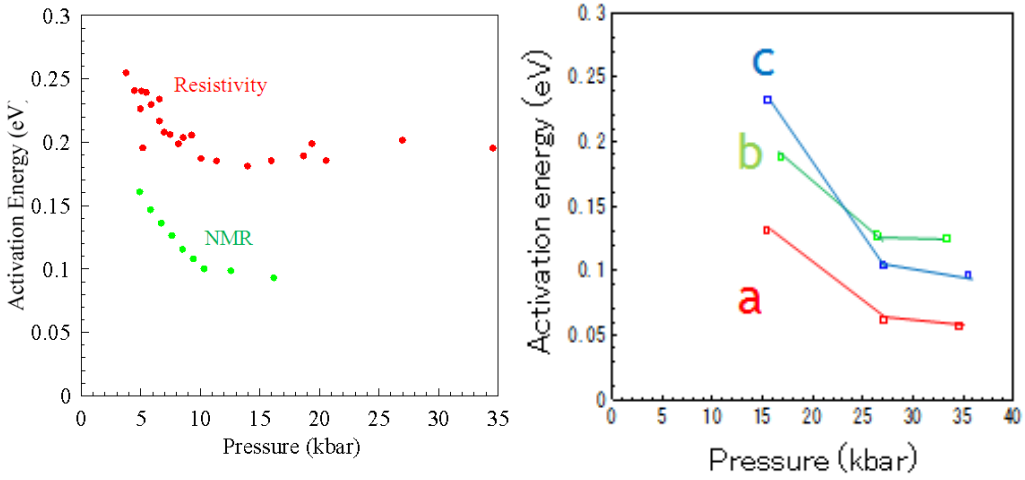


Fig. 4.1.5. (b) Pressure dependence of the activation energies of electric resistivity along **a** axis and of $^{1}$H NMR $1/T_1$ in the ferroelectric ionic phase. (c) Pressure dependence of the activation energy of the electric resistivity in the **a**, **b**, and **c** directions in the paraelectric ionic phase.

### 4.1.2 Discussion

The fact that the activation energy in all the directions is almost the same as shown in Fig.4.1.4 suggests that the carriers in the ferroelectric ionic phase are one-particle excitations. The observed gap is attributed to the smallest energy gap in band dispersion regardless of the directions. In the ferroelectric ionic phase, the mobile solitons were suggested to play a role of carriers [42]; however, recently it has been experimentally indicated that the solitons are not the carriers [44]. The result in the present study is consistent with the recent consequence. The solitons should be localized in chains by the three-dimensionality. According to the band structure calculations of TTF-CA, the smallest energy gap is in the direction Y (0, 1, 0)→Γ (0, 0, 0) [31, 32, 63]. Thus, the decrease of the activation energy with increasing pressure up to 10kbar implies an increase in the transfer integral in the **b** axis direction. We estimate the smallest band gap from the resistivity, which is the doubled activation energy, as 0.52eV around 4kbar, and 0.38eV for pressures above 10kbar. The $1/T_1$ has activation energies smaller than the charge excitation energy probed by the resistivity. This indicates that the spin excitations without charge are lowest lying in energy. Two mechanisms are conceivable; one is spin soliton and the other is spin triplet. The former is predicted as the lowest energy excitation in the one-dimensional system [40]. However, the ferroelectric phase is a three-dimensionally ordered state. The solitons, if thermally excited as free particles, would destroy the ferroelectric ordering, thus contradicting the experimental fact. So, the solitons, if they exist, may be excited as soliton-antisoliton bound pairs. This form of excitations is not inconsistent with the previous indication that spin solitons are not main contribution to the conductivity. However, the three dimensionality of the ferroelectric ionic phase tends to prohibit the soliton excitations and favors the singlet-triplet excitations. Furthermore, the pressure dependence of the activation energies of the resistivity and $1/T_1$ is similar; 10kbar appears to be a characteristic point, for both. Alternatively, it is seen that the two gaps moderately approach each other at low pressures below 10kbar, implying that the spin-charge coupling is gradually developed. Noticeably, the scaling analysis described in Chapter3 suggests that the nature of the ferroelectric phase at low pressures is possibly distinguished from the widely accepted picture of spin-Peierls states. It is likely that spin-charge coupled Peierls phase crosses over to the spin-charge decoupled spin-Peierls phase around 10kbar.

In the paraelectric ionic phase, the activation energy depends on the direction in which resistivity is measured (Fig. 4.1.5 (c)). This implies that carriers in the paraelectric ionic phase are not due to the one-particle excitations. The pressure dependence of the resistivity at room temperature (Fig. 4.1.1) indicates that the properties of the carriers are hardly affected by the lattice contraction. Besides, the absolute value of the resistivity along the **a** axis is about several Ωcm, which is extraordinarily small as an insulator. The NQR and IR measurements support a picture of a dimer liquid state in the paraelectric ionic phase, implying that spin solitons are easily excited. In the

paraelectric ionic phase, the interchain interaction between the one-dimensional chains is disturbed thermally. The activation energy for the **a** axis is so small, *e.g.*, about 0.06eV at 35kbar, and is comparable to the theoretical prediction of approximately 0.1eV [42]. All of these appear consistent with the soliton excitations. However, the activation energies for the **b** and **c** axes are also small, *e.g.*, 0.1~0.15eV around 35kbar, though they are larger than the value for the **a** axis. This feature appears against the soliton picture because the soliton excitations are essentially a phenomenon in one dimension. Thus, there may be low energy carrier excitations other than the spin solitons at least in the **b** and **c** directions.

## 4.2 Electric resistivity measurements under uniaxial pressure

In TTF-CA, TTF and CA stack alternatively along the **a** axis. This is the reason why this material is addressed as a mixed-tack material. Along the **b** axis, however, the same kinds of molecules, TTF or CA are nearest neighbors (see Fig. 4.1.6). Therefore, if the inter-molecular distance along the **b** axis is contracted, the crystal gets to possess the segregated-stack nature along the **b** axis like TTF-TCNQ, offering an access to the metallization of the NI materials. This idea is also promising from the band calculation of TTF-CA [63], which shows that the lowest band gap is in the direction of the **b** axis, and predicts that the increased transfer integral along the **b** axis makes the system metallic. The dispersion along the **a** axis always has the energy gap corresponding to the energy difference between the HOMO of TTF and the LUMO of CA, which indicates that the system is inevitably an insulator even under pressure. Therefore, we applied uniaxial pressure along the **b** axis to TTF-CA. The resistivity measurements were carried out along the **a** and **b** axes to examine the electronic states.

### 4.2.1 Results

Fig. 4.2.1 shows electric resistivity along the **a** and **b** axes against **b**-axis uniaxial pressure at room temperature. The resistivity along the **b** axis exhibits a drastic decrease in a low pressure region; the decrease from the ambient pressure value is three orders of magnitude at 2kbar, and six orders of magnitude at 10kbar. Such a rapid decrease is not observed under hydrostatic pressure (see Fig. 4.2.2). We examined the sample dependence of the **b**-axis resistivity under the **b**-axis pressure, and confirmed the reproducibility of the drastic decrease. In contrast to the **b**-axis resistivity, the **a**-axis resistivity shows almost the same pressure dependence under hydrostatic and **b**-axis pressures. This implies that NIDW's contribute significantly to the **a**-axis conduction even under **b**-axis pressure.

The results for the **b**-axis pressure show a large change in the anisotropy as shown in Fig. 4.2.3, which considerably differs from the hydrostatic case. In Fig. 4.2.3, the anisotropy is defined as the ratio of the **a**-axis conductivity to the **b**-axis conductivity, ($\sigma_a/\sigma_b$). The anisotropy over one means that the mixed-stack along the **a** axis is dominating, while the anisotropy below one means that the segregated-stack character along **b** axis is dominating. At ambient pressure the system has the properties of the mixed-stack, but with increasing the **b**-axis pressure to 2.5kbar the anisotropy is decreased to a minimum of 0.006, suggesting that the system gets to take on the segregated feature along the **b** axis. As pressure is further applied, the pressure dependence turns around to a steep increase, reaching a maximum of 4 around 12kbar, where the mixed-stack feature is recovered again, which is likely due to the NIDW conduction. Then, the anisotropy is decreased again above 12kbar, and the system gradually gets to bear the feature of the segregated-stack. These results indicate that the electronic state of TTF-CA is controlled between the mixed-stack regime and the segregated-stack regime by uniaxial pressure.

Fig. 4.2.4 shows the temperature dependence of the **b**-axis resistivity under the **b**-axis uniaxial and hydrostatic pressures. TTF-CA in the segregated-stack regime at 4.5kbar, 20.1kbar, and 31.5kbar is still an insulator. However, the resistivity obviously has smaller values than those under the hydrostatic pressure. Fig. 4.2.5 shows the temperature dependence of the **a**-axis resistivity under the **b**-axis pressure at 6.8 and 10.0kbar. At 6.8kbar, where the system is in the segregated-stack regime, a metallic temperature-dependence is observed at 250~300K, which is attributed to the NIDW conduction. Activation plot of the **b**-axis resistivity under the **b**-axis pressure is shown in Fig. 4.2.6 (a), and the pressure dependence of activation energies of the **a**-axis and **b**-axis resistivity under the **b**-axis pressure is presented in Fig. 4.2.6 (b). The activation energies were estimated in the temperature region of 40~100K. Remarkably, the activation energies under the **b**-axis pressure are in a range of 0.04~0.06eV, which is much smaller than the values under the hydrostatic pressure, 0.19~0.26eV. After all, we could not obtain the metallic state in TTF-CA; however, the results indicate that the uniaxial pressure in a particular direction is a promising way for the metallization of the NI systems.

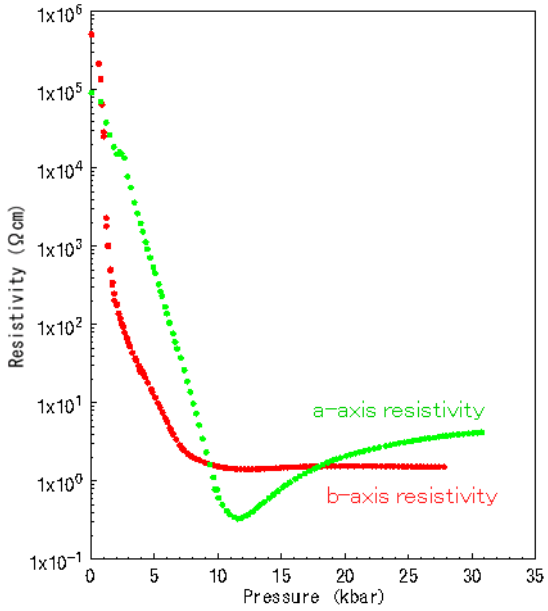


Fig. 4.2.1. Pressure dependence of resistivity along the **a** and **b** axes under the **b** axis uniaxial pressure at room temperature.

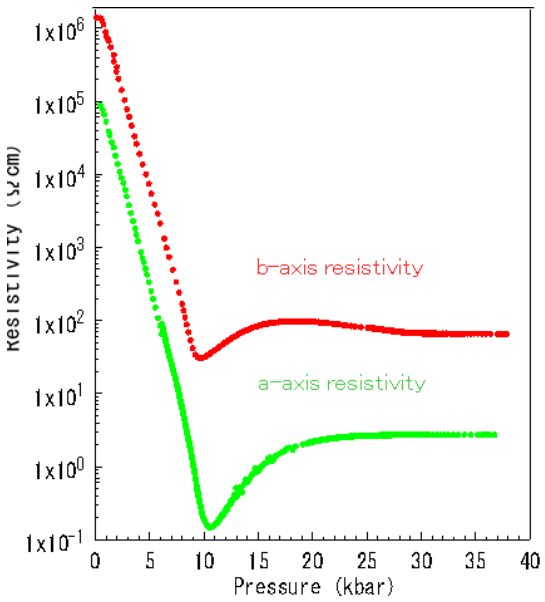


Fig. 4.2.2. Pressure dependence of resistivity along the **a** and **b** axes under the hydrostatic pressure at room temperature.

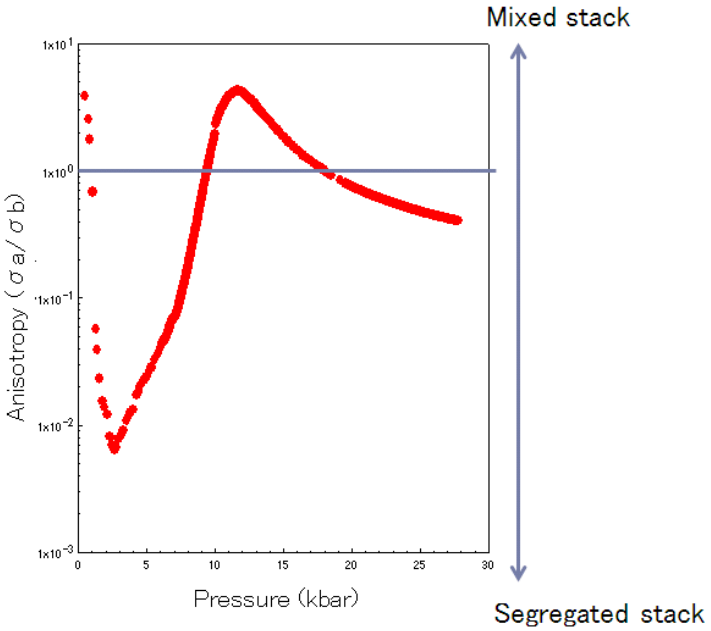


Fig. 4.2.3. Pressure dependence of the anisotropy of conductivities along the **a** and **b** axes, ($\sigma_a/\sigma_b$), under the **b** axis uniaxial pressure at room temperature.

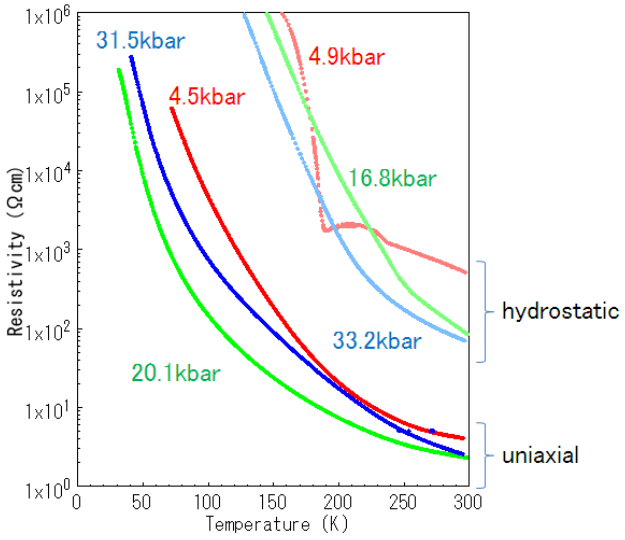


Fig. 4.2.4. Temperature dependence of the **b** axis resistivity under the **b**-axis uniaxial and hydrostatic pressures.

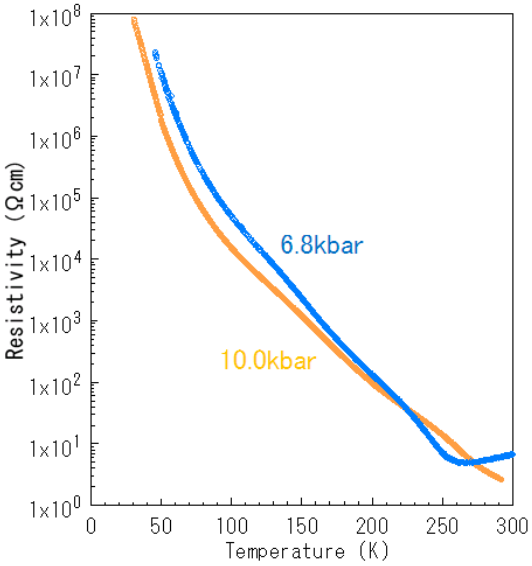


Fig. 4.2.5. Temperature dependence of the **a** axis resistivity under the **b** axis uniaxial pressure at 6.8 and 10.0kbar.

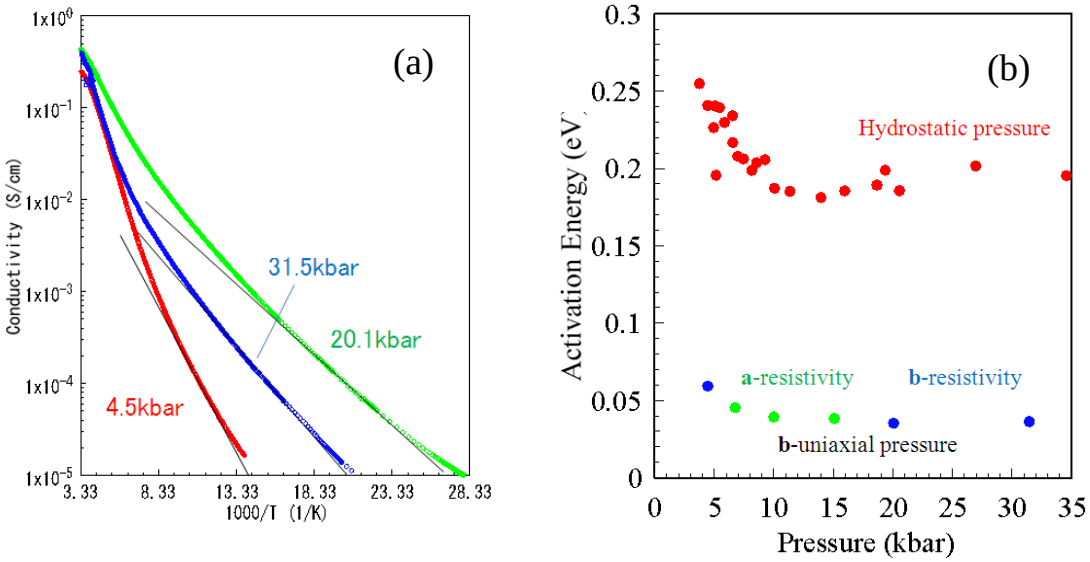


Fig. 4.2.6. (a) Activation plot of the **b**-axis resistivity under the **b**-axis pressure (b) Pressure dependence of activation energy of the **a**- and **b**-axis resistivity under the **b**-axis pressure.

### 4.2.2 Discussion

The exponential-like decrease of the resistivity against the **b**-axis pressure (Fig. 4.2.1) is considered to be due to change of the number of conduction carriers, because in general mobility. is not changed exponentially. As mentioned in the previous section, the pressure dependence of the **a**-axis resistivity under the **b**-axis pressure indicates that the NIDWs are excited similarly to the case under the hydrostatic pressure. On the basis of these results, we propose, as a candidate of the conduction mechanism, NIDW-mediated conduction along the **b** axis in the following. Fig. 4.2.7 shows a schematic electronic state projected onto the **ab** plane of TTF-CA under pressure, where the neutral and ionic molecules are arranged with forming domains along the **a** axis. If the neutral molecules lie side by side in the **b** axis direction, electrons cannot move along the segregated-stack direction unless they are excited on the conduction band, because the HOMOs of the donor molecules are fully occupied with electrons. However, in the presence of the NIDWs, for example in the grey-colored region in Fig. 4.2.7, electrons can move through unoccupied ionic molecules. It can be regarded as the hole-doped state. Thus, as the number of the NIDWs is increased exponentially under pressure, electrons which can move are increased and they can be carriers. This conduction can be observed under the hydrostatic pressure, but the transfer integral along the **b** axis should be increased more than the hydrostatic pressure case, and in consequence, the resistivity under the **b** axis uniaxial pressure is enormously decreased.

However, in the NIDW-mediated conduction, the **b**-axis resistivity should have similar behavior to the **a**-axis resistivity, and this is not achieved in the **b**-axis pressure. Another candidate is change of band dispersion along the **b** axis; for example, drastic increase of the transfer integral along **b** axis under **b**-axis pressure.

As for the low temperature ferroelectric state, the activation energies of the **a-** and **b**-axis resistivity are approximately the same, which is suggestive of the quasi-particles excitations. Moreover, the activation energy varies similarly against hydrostatic pressure and uniaxial pressure, as shown in Fig. 4.2.6. The activation energy moderately decreases, as pressure is increased up to 10kbar, followed by a constant above 10kbar.

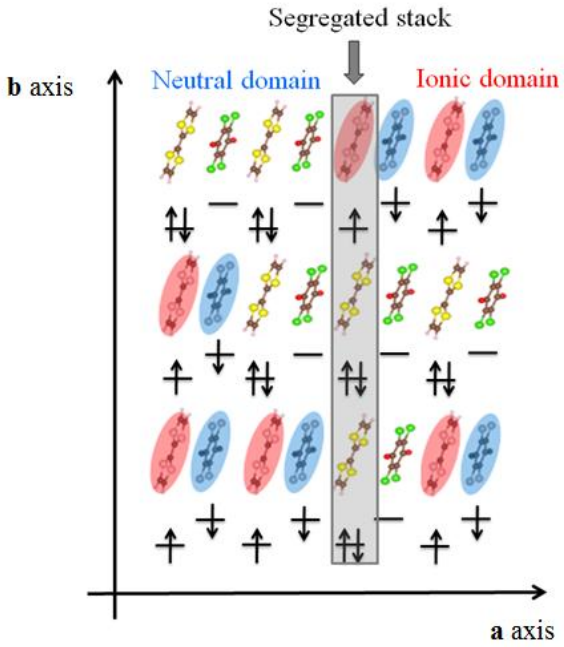


Fig. 4.2.7. Schematic of electronic state projected onto the **ab** plane of TTF-CA under the pressure.

## 4.3 Electric resistivity measurements of $M_2P$-$TCNQF_4$ under hydrostatic pressure

As seen in the last section, the strategy to compress TTF-CA in a direction of the segregated-stack works well for rendering the NI material to a highly conductive state. Fig.4.3.1 situates three materials in the notional axis connecting the mixed-stacking and segregated-stacking configurations [58], where TTF-CA and TTF-TCNQ are located in the two limiting regimes, respectively. Since the mixed-stacking and segregated-stacking compounds afford insulators and metals, respectively, the intermediate electronic states are expected to occur in the intermediate structures. the NI system,$M_2P$-$TCNQF_4$, is located there as shown in Fig. 4.3.1. Thus, we have investigated this material for a promising access to the metallization of the NI materials.

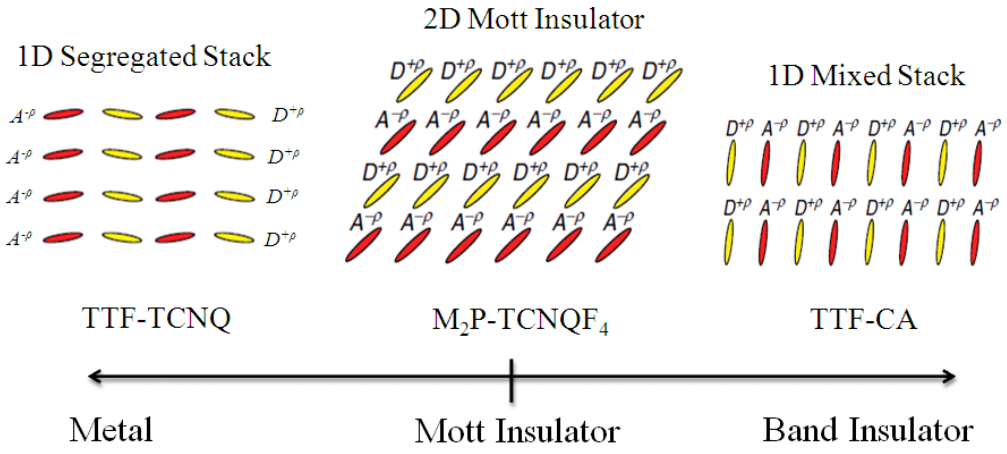


Fig. 4.3.1. Three materials located in a notional axis which connects the mixed-stacking and segregated-stacking structures [59].

### 4.3.1 Physical properties of $M_2P$-$TCNQF_4$

Table 4.3.1 shows inter-molecular distances, transfer integrals and the optical gap along the DD/AA and DA directions [58]. The inter-molecular distances in $M_2P$-$TCNQF_4$ are similar in every direction, differently from TTF-CA, where the DD/AA distances are approximately twice as long as the DA distances [28]. Correspondingly, the transfer integrals in $M_2P$-$TCNQF_4$ are not so different in every direction (Table 4.3.1), while the transfer integral in the DA pair is one order of magnitude larger than those of the DD/AA pairs in TTF-CA [63]. Moreover, $M_2P$-$TCNQF_4$ is suggested as the Mott insulator by the experimental results of $\rho$ in excess of 0.95 and paramagnetic behavior above 122K as shown in Fig. 4.3.2, which shows the temperature dependence of the spin susceptibility [58, 77, 78]. At 122K, lattice dimerization with the spin singlet occurs, as was also evidenced by an enhancement in the intensity of the $a_g$ molecular vibrational mode and a reduction in the spin

susceptibility (Fig. 4.3.2). Among the optical gaps listed in Table 4.3.1, the lowest value is assigned to be the Mott gap corresponding to the AA excitations [58]. Thus, we have aimed at closing the Mott gap in the AA direction by means of increasing the transfer integral along the AA direction under hydrostatic pressure.

Table. 4.3.1. Inter-molecular distances, transfer integrals and the optical gaps in the DD/AA and DA directions [58].

| | Intermolecular distance (Å) | Transfer integral (eV) | Optical gap (eV) |
|---|---|---|---|
| DA | 5.8725 | 0.0671 | 0.9 |
| DD | 6.9920 | 0.0293 | 1.37 |
| AA | 6.9920 | 0.0431 | 0.72 |

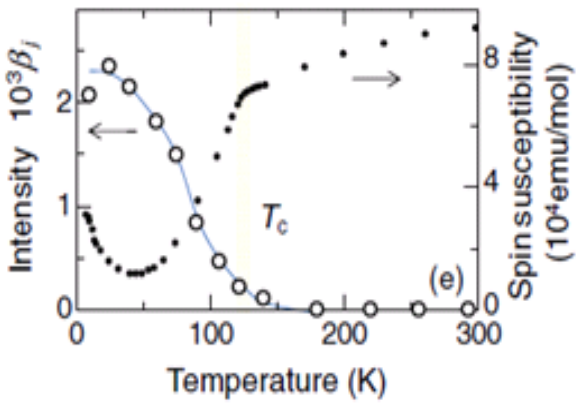


Fig. 4.3.2. Temperature dependence of spin susceptibility and intensity of $a_g$ molecular vibrational mode at ambient pressure [58].

### 4.3.2 Results

Fig. 4.3.3 shows the pressure dependence of resistivity of $M_2P$-$TCNQF_4$ along the DD/AA direction at room temperature, measured under the cubic anvil hydrostatic pressure. With increasing pressure, the resistivity of approximately 400kΩcm at ambient pressure is monotonously decreased and reaches about 4Ωcm, a five-orders-of-magnitude drop, at 80kbar. This behavior is very different from that of TTF-CA, which shows nearly constant resistivity above 20kbar. We consider that the monotonous resistivity reduction in $M_2P$-$TCNQF_4$ is attributed to a simple Mot-gap closing by increased transfer integrals similarly to general organic Mott materials. The temperature dependence of the resistivity of $M_2P$-$TCNQF_4$ along the DD/AA direction at several pressures is shown in Fig. 4.3.4. In a pressure range of 5.13~19.44kbar, the resistivity was measured with the clamp-type cells, while above those pressures the cubic anvil apparatus was used. In all pressures up to 80kbar, the resistivity of $M_2P$-$TCNQF_4$ shows insulating behavior against temperature variation, and the metallization was not achieved. Any kinks indicating the dimerization transition were not also observed in the present study; thus the phase diagram of this material is still unknown. Activation plot of the resistivity in 5.13~60kbar and at 80kbar, as shown in Figs. 4.3.5 (a) and (b), respectively, gives the pressure dependence of the activation energy obtained as shown in Fig. 4.3.6. In Fig. 4.3.5 (a), the conductivity up to 19.44kbar well obeys the activation type behavior and deviates somewhat from the linearity at low temperatures. At 80kbar, the behavior is no longer the simple activation type; it can be characterized by a continuous decrease of the activation energy against pressure increase. Tentatively, the activation energies are estimated at high temperatures around 300K and low temperatures around 10~30K (see Fig. 4.3.6). Noticeably, the latter value of approximately 4.3meV signifies that the system is approaching the metallic phase.

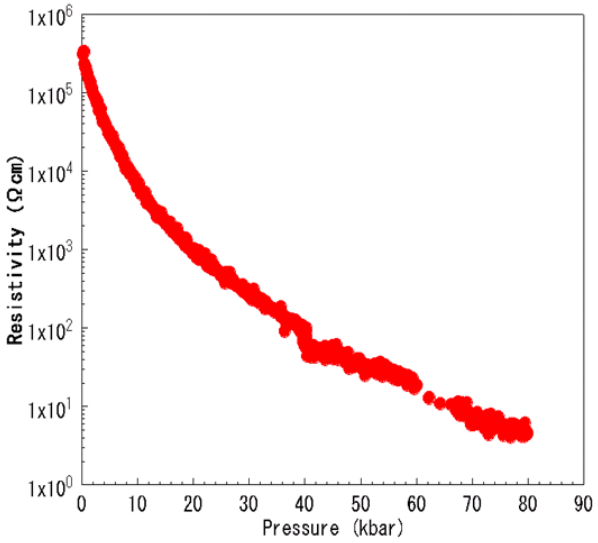


Fig. 4.3.3. Pressure dependence of resistivity of $M_2P$-$TCNQF_4$ along the DD/AA direction at room temperature.

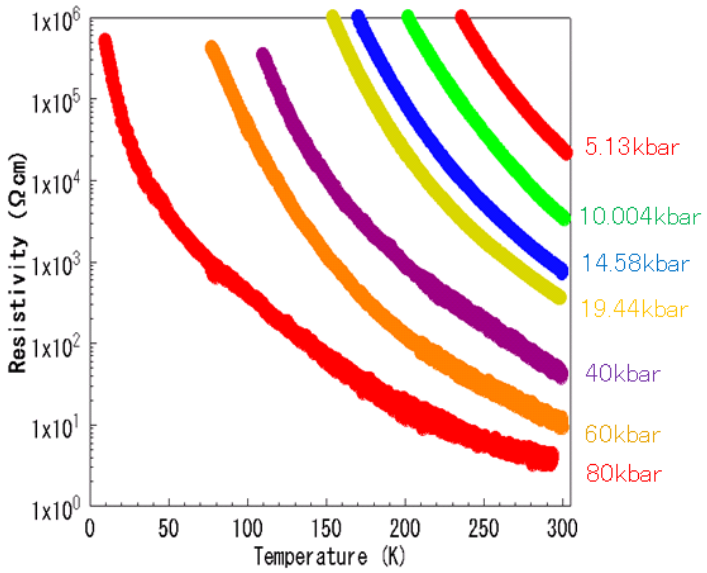


Fig. 4.3.4. Temperature dependence of resistivity of $M_2P$-$TCNQF_4$ along the DD/AA direction at several pressures.

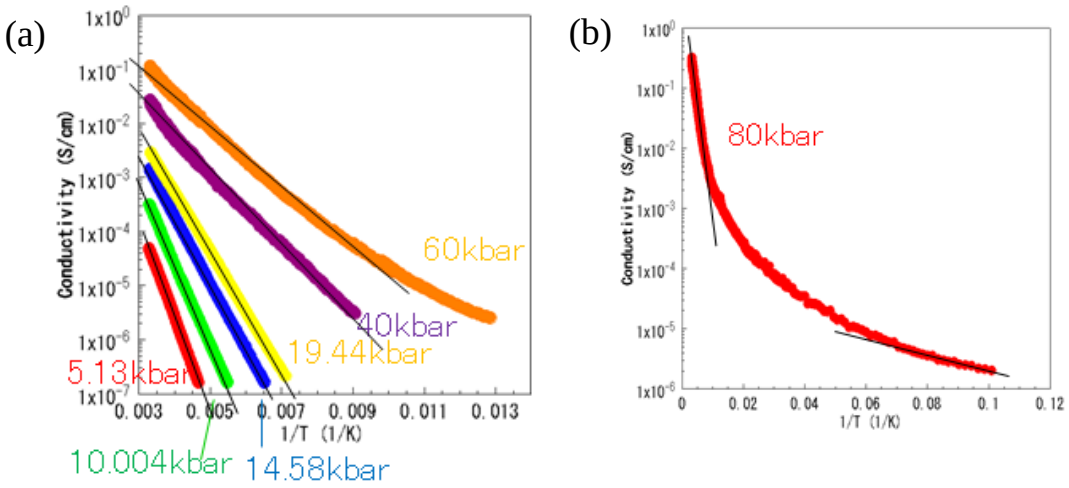


Fig. 4.3.5. Activation plot of resistivity of $M_2P$-$TCNQF_4$ at (a) several pressures in a range of 5.13~60kbar and (b) 80kbar.

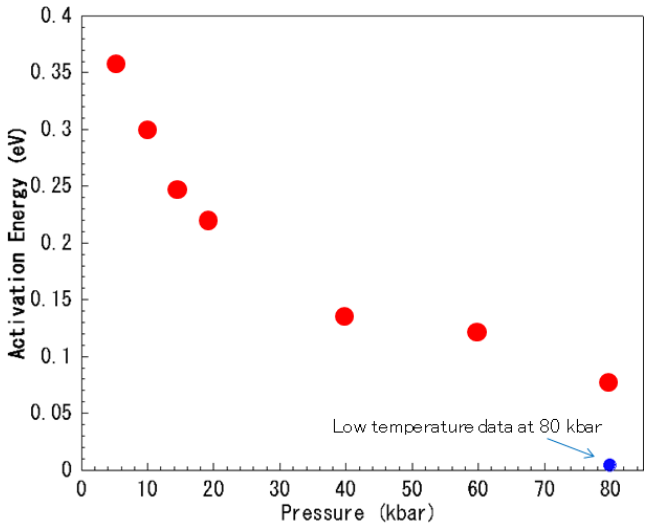


Fig. 4.3.6. Pressure dependence of the activation energy of $M_2P$-$TCNQF_4$.

### 4.3.3 Discussion

The activation energy of about 0.36eV at 5kbar, though we were not able to use the four-terminal method at ambient pressure because of the high resistance, agrees with the Mott gap 0.72eV of the AA direction estimated in the optical measurements at ambient pressure, since the optical gap is double the activation energy in the transport. This suggests that the carriers taking on the electric conduction are quasi-particles thermally excited on the upper Hubbard band. This is also supported by the activation plot of the resistivity of the DA direction with the two-terminal method at ambient pressure, where the huge resistivity did not allow the reliable four-terminal measurements, as shown in Fig. 4.3.7, yielding activation energy of about 0.75eV. Generally, when a charge gap is opened, the quasi-particle excitation energy in resistivity corresponds to the lowest gap in the band dispersion, resulting in the same activation energy for the measurements along the DD/AA and DA directions. These experimental results exactly mean that quasi-particles excited on the upper Hubbard band are charge carriers, and thus the decrease of the activation energy against pressure variation is due to the increase of the transfer integral of the AA direction which is suggested to have a minimum gap (see Table. 4.3.1), leading to a hopeful perspective that further pressure may cause the gap to be closed. It should be mentioned that $M_2P$-TCNQ$F_4$ consisting of two molecular species is different from conventional organic Mott insulators, where thermally activated carriers are on the same of molecular species. Something new is expected in the Mott transition and the metallic phase in association with the multi-orbital character.

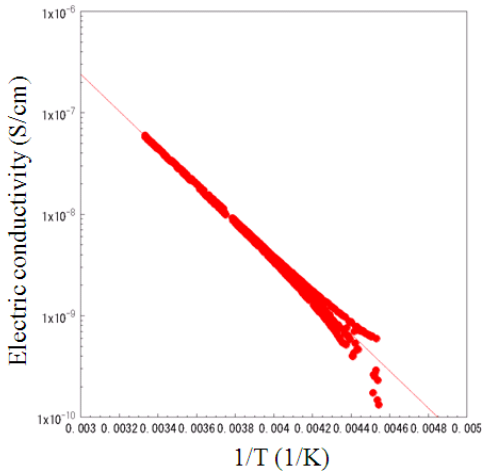


Fig. 4.3.7. Activation plot of the electric resistivity of the DA direction with the two-terminal method at ambient pressure.

## 4.4 Summary

We have attempted the metallization of the NI materials by three methods. First, we investigated TTF-CA under extremely high pressures using the cubic anvil apparatus, which is a kind of brute force method. TTF-CA did not become a metal up to 82.5kbar. We examined the conduction mechanisms in the ionic phases at low temperatures, where the activation energy is gradually decreased with increasing pressure up to 10kbar and levels off at the higher temperatures. The resistivity showed direction-independent activation energies that support quasi-particle excitations and are unfavorable for the previously suggested soliton conduction which would show strongly direction-dependent temperature dependence. It is still an open question why the carriers have such small excitation energies of 0.38~0.52eV relative to the simple band calculation. In the paraelectric ionic phase, although this phase is also insulating, the activation energies deduced from the activation plot of resistivity are not coincident for the directions of the measurements, thus not supporting the quasi-particle excitations over a well-defined energy gap, as observed in the ferroelectric ionic phase. Two situations are conceivable; a case that the charge transport is not thermally activated and the other case that the conduction carriers differ from the quasi-particles and their properties are qualitatively directional-dependent. Considering that a dimer liquid is indicated as a state complying with both of the NQR and the IR results, the spin solitons with charges are among the candidates of charge carriers.

The second method is to apply the uniaxial pressure along the **b** axis, in which the DD or AA are neighbors. The metallization was not achieved in this experiment as well, but we found a drastic reduction in resistivity along the **b** axis. This result points to a drastic change of electronic state from the mixed-staking regime toward the segregated-stacking regime. We suggest that the drastic resistivity reduction is attributed to the NIDW-mediated conduction as one of candidates, which is like a self-doped conduction along the **b** axis. On the other hand, another carrier candidate is a quasi-particle excitation along the **b** axis. The low-temperature ferroelectric phase under the **b**-axis pressure shows activation energies several times smaller than the hydrostatic case.

Lastly, $M_2P$-$TCNQF_4$, which is situated intermediately between the mixed- and segregated-stack electronic states, is investigated under the cubic anvil hydrostatic pressure. This method brought $M_2P$-$TCNQF_4$ to a nearly metallic state with the low activation energies of 4.3meV at 80kbar. The observed transport results are explainable by quasi-particle excitations in the AA direction over the Hubbard gap. The manner of the gap reduction against pressure increase suggests that further pressure potentially make $M_2P$-$TCNQF_4$ a metal.

# Chapter 5 Conclusions

In the present thesis, we have studied the NI transition systems to understand the physics of the phenomena due to the interplay of the strong electron-electron and electron-lattice interaction. We focused on the two issues; i) conduction mechanism in the NI crossover, where the charge degrees of freedom are recovered in insulating phases in a unique way, and ii) conduction mechanism coupled with the lattice degrees of freedom in the ionic phases. We also investigated the phase diagram of TTF-CA with scaling analysis from a view point of charge-lattice decoupling. Furthermore, we have tried to metallize the NI transition materials, seeking for novel metallic states.

First, we constructed the *P-T* phase diagram of TTF-CA by the four-terminal electric resistivity measurements under pressures up to 35kbar, where there is apparently inconsistency between the previous results of the NQR and IR measurements on the lattice dimerization. The resistivity results are consistent with the existence of the paraelectric ionic phase in a high temperature and pressure region and also confirmed the NI crossover, which stems from the original NI transition without symmetry breaking.

The NI crossover, in spite of transience between two insulator phases, is accompanied by a resistivity minimum with a low value of 0.1Ωcm, which is comparable to the resistivity of typical organic conductors. This is hard to be explained with conventional one-particle carrier excitations. We investigated the directional dependence of resistivity, namely the anisotropy, against temperature and pressure variations and performed the detailed resistivity measurements under accurately controlled pressure. As a result, we have found the enhancement of the charge transport strongly related to the donor-accepter charge transfer and highly one-dimensional. Moreover, we obtained the activation energy of 0.055eV in charge transport on the NI crossover and its pressure dependence, which suggests that the NIDW excitations most likely dominate the electric conduction, though the case of the LR-NIDWs is not ruled out.

We carried out the scaling analysis of the resistivity across the NI crossover tentatively in terms of a form of the quantum scaling. We found that the scaling is successful in the paraelectric region and the charge transport in the ferroelectric ionic phase was definitely distinguished from that in the NI crossover region by the scaling. The analysis also shows that the charge transfer Widom line approaches the ferroelectric ionic phase in such a way as to crosses the ferroelectric transition (dimerization) line, not merge unto it, suggesting that that a virtual critical end point may be behind the ferroelectric dimerized phase. These features are consistent with the picture that the charge carriers in the NI crossover are the NIDW excitations, though the LR-NIDWs may also result from the lattice fluctuation. To test the NIDW picture further, we assumed the previously reported $^{1}$H-NMR relaxation rate as a measure of the numbers of the ionic molecules and performed the

fitting of the data with the one-dimensional antiferromagnetic XXZ model, which is suggested to model the NI transition. The fitting indicates that the NI system can be interpreted as the Ising model, which explains the observation of the activation energy in the NI crossover region. On the basis of this result, we estimated the number of the NIDW excitations at room temperature at $2.61\times10^{20}cm^{-3}$, which can contribute to the extremely small resistivity values in the NI crossover. In addition, we interpret the seemingly metallic behavior of the resistivity in the NI crossover as an manifestation of the temperature dependence of the activation energy of the NIDW excitations.

The anisotropy of charge transport in the ferroelectric ionic phase showed that carriers in the phase can be identified as one-particle excitations, which exclude possibility of the soliton conduction suggested before. In the paraelectric ionic phase, the activation energies, if any, in each direction are not coincident, implying that the carriers in that phase are not one-particle excitations. The dimer liquid state, suggested by the NQR and the IR measurements, supports the spin soliton conduction with 0.06eV as one of candidates for conduction carriers.

We conclude that the NIDW excitations with much lower energy than one-particle excitations dominate in the NI phase boundary, where the charge degrees of freedom are recovered. In the case where the charge is nearly fully transferred, the lattice degrees of freedom can play an important role in the low energy excitations like the spin solitons in the paraelectric ionic phase. In situations where there is no room for both degrees of freedom, one-particle excitations over the band gap energy get visible like in the ferroelectric ionic phase. These unique elementary excitations appear on the phase diagram of TTF-CA; the charge transfer Widom line shows the vital being of the charge degrees of freedom, and the dimerization transition line distinguishes the existence or non-existence of the lattice degrees of freedom.

With the aim at metalizing the NI materials, we have made three attempts.. First, we measured the resistivity of TTF-CA under high pressures up to 82.5kbar, attained by the cubic anvil apparatus, but did not observe a metallic behavior. The second method was to compress TTF-CA in the **b** axis direction to get closer DD or AA contacts, which is expected to make the system acquire the segregated nature in the **b** axis. The metallization of TTF-CA was not also achieved; however, this method caused a drastic change in the resistivity anisotropy and an reduction of the activation energy in the ferroelectric ionic phase, which was not attained by the 80kbar hydrostatic pressure. These signify a successful control of TTF-CA between the mixed- and the segregated-stack regimes. As the third strategy, we directed our attention to another material, $M_2P$-$TCNQF_4$, which has intermediate properties between the mixed- and the segregated-stack regimes, and measured the resistivity under the cubic anvil hydrostatic pressure. Although $M_2P$-$TCNQF_4$ is still an insulator for the pressures investigated, the activation energy at low-pressures, 0.36 eV, could be reduced to as small as 4.3meV at 80kbar. The whole data, along with the existing structural and optical data, are explainable by the picture that the conduction carriers are quasi-particles excited over the Mott gap in the AA direction.

Further pressure is expected to cause the Mott gap to be closed.

The present study revealed that various phases coupled to the charge and lattice degrees of freedom emerge, and in those phases, there exist particular charge transport mechanisms with low energy exotic excitations related to the charge and the lattice degrees of freedom, which cannot be observed in normal electronic phases. These results verify variety of charge transport mechanisms in the charge-lattice coupled system. We also show availability of control of anisotropy and dimensionality for the metallization of NI materials that are always insulators. We expect that the metallization will lead to novel phenomena, for example, new superconducting phases deriving from large dielectric fluctuation. We can conclude that the present study gives new knowledge to physics of dielectric materials in terms of the charge-lattice coupling.

# References


[1] J.B. Torrance, J.E. Vasquez, J.J. Mayerle, and V.Y. Lee, Phys. Rev. Lett. **46**, 253 (1981).

[2] V. Oison, C. Katan, and C. Koenig, J. Phys. Chem. A **105**, 4300 (2001).

[3] J.B. Torrance, A. Girlando, J.J. Mayerle, J.I. Crowley, V.Y. Lee, P. Batail, and S.J. Laplaca, Phys. Rev. Lett. **47**, 1747 (1981).

[4] H. M. McConnell, B. M. Hoffman, and R. M. Metzger, Proc. Nat. Acad. Sci. U. S. A. **53**, 46 (1965).

[5] Y. Tokura, H. Okamoto, T. Koda, T. Mitani, and G. Saito, Solid State Commun. **57**, 607 (1986).

[6] A. Girlando, F. Marzola, C. Pecile, and J. B. Torrance, J. Chem. Phys. **79**, 1075 (1983).

[7] K. Takaoka, Y. Kaneko, H. Okamoto, Y. Tokura, T. Koda, T. Mitani, and G. Saito, Phys.Rev.B **36**,3884 (1987).

[8] M. Masino, A. Girlando, and Z. G. Soos, Chem. Phys. Lett. **369**, 428 (2003).

[9] H. Matsuzaki, H. Takamatsu, H. Kishida, and H. Okamoto, J. Phys. Soc. Jpn. **74**, 2925 (2005).

[10] S. Horiuchi, Y. Okimoto, R. Kumai, and Y. Tokura, J. Chem. Phys. **325**, 78 (2006).

[11] M. Masino, A. Girlando, and A. Brillante, Phys. Rev. B **76**, 064114 (2007).

[12] A. Dengl, R. Beyer, T. Peterseim, T. Ivek, G. Untereiner, M. Dressel, J. Chem. Phys. **140**, 244511 (2014). (arXiv:1312.6732 [cond-mat.str-el])

[13] Y. Tokura, T. Koda, G. Saito, and T. Mitani, J. Phys. Soc. Jpn. **53**, 4445 (1984).

[14] S. Inagaki, and H. Fukuyama, J. Phys. Soc. Jpn. **52**, 2504 (1983).

[15] N. Nagaosa, and J. Takimoto, J. Phys. Soc. Jpn. **55**, 2735 (1986).

[16] H. Takamatsu, Master Thesis (2003).

[17] M. Hososda, Master Thesis (2010).

[18] Y. Tokura, T. Koda, T. Mitani, and G. Saito, Solid State Commun. **43**, 757 (1982).

[19] S. Horiuchi, Y. Okimoto, R. Kumai, and Y. Tokura, J. Phys. Soc. Jpn. **69**, 1302 (2000).

[20] H. Okamoto, Y. Tokura, T. Koda, and G. Saito, Synth. Met. **19**, 527 (1987).

[21] M. Gourdji, L. Guibé, A. Péneau, J. Gallier, B. Toudic, and H. Cailleau, Solid State Commun. **77**, 609 (1991).

[22] J. Gallier, B. Toudic, Y. Delugeard, H. Cailleau, M. Gourdji, A. Péneau, and L. Guibé, Phys. Rev. B **47**, 11688 (1993).

[23] M. H. Lemée-Cailleau, M. Le Cointe, H. Cailleau, T. Luty, F. Moussa, J. Roos, D. Brinkmann, B. Toudic, C. Ayache, and N. Karl, Phys. Rev. Lett. **79**, 1690 (1997).

[24] C. P. Slichter: Principles of Magnetic Resonance (*Springer*, 1990).

[25] F. Iwase *et al*., *PSJ 2008 Spring Meeting* 26pTF-6.

[26] A. A. Koukoulas *et al.*, Chem. Phys. Lett. **167**, 379 (1990)

[27] Y. Kanai, M. Tani, S. Kagoshima, Y. Tokura, and T. Koda, Synth. Met. **10**, 157 (1984).

[28] M. Le Cointe, M.H. Lemée-Cailleau, H. Cailleau, B. Toudic, L. Toupet, G. Heger, F. Moussa, P. Schweiss, K.H. Kraft, and N. Karl, Phys. Rev.B **51**, 3374 (1995).

[29] M. Le Cointe, M.H. Lemée-Cailleau, H. Cailleau, and B. Toudic, Journal of Molecular Structure, **374**, 147 (1996).

[30] K. Kobayashi, S. Horiuchi, R. Kumai, F. Kagawa, Y. Murakami, and Y. Tokura Phys. Rev. Lett. **108**, 237601 (2012).

[31] S. Ishibashi, and K. Terakura, Physica B **405**, 338 (2010).

[32] S. Ishibashi, and K. Terakura, J. Phys. Soc. Jpn. **83**, 073702 (2014).

[33] Z. G. Soos and A. Painelli, Phys. Rev. B **75**, 155119 (2007).

[34] N. Nagaosa, J. Phys. Soc. Jpn. **55**, 2754 (1986).

[35] K. Yonemitsu, J. Phys. Soc. Jpn. **80**, 084707 (2011).

[36] S. Horiuchi, Y. Okimoto, R. Kumai, and Y. Tokura, Science **299**, 229 (2003).

[37] S. Horiuchi, Y. Okimoto, R. Kumai, and Y. Tokura, Synth. Met. **133**, 615 (2003).

[38] Y. Okimoto, R. Kumai, S. Horiuchi, H. Okamoto, and Y. Tokura, J. Phys. Soc. Jpn. **74**, 2165 (2005).

[39] F. Iwase, K. Miyagawa, S. Fujiyama, K. Kanoda, S. Horiuchi, and Y. Tokura, J. Phys. Soc. Jpn. **76**, 073701 (2007).

[40] P. Ranzieri, M. Masino, A. Girlando, and M. H. Lemée-Cailleau, Phys. Rev. B **76**, 134115 (2007).

[41] K. Sunami, Master Thesis (2011).

[42] N. Nagaosa, and J. Takimoto, J. Phys. Soc. Jpn. **55**, 2745 (1986).

[43] H. Kishida, H. Takamatsu, K. Fujinuma, and H. Okamoto, Phys. Rev. B **80**, 205201 (2009).

[44] F. Kagawa, S. Horiuchi, H. Matsui, R. Kumai, Y. Onose, T. Hasegawa, and Y. Tokura, Phys. Rev. Lett. **104**, 227602 (2010).

[45] W. P. Su, J. R. Schrieffer, and A. J. Heeger, Phys. Rev. Lett. **42**, 1698 (1979).

[46] H. Okamoto, T. Mitani, Y. Tokura, S. Koshihara, T. Komatsu, Y. Iwasa, T. Koda, and G. Saito, Phys. Rev. B **43**, 8224 (1991).

[47] M. Buron-LeCointe, M. H. Lemée-Cailleau, H. Cailleau, S. Ravy, J. F. Bérar, S. Rouzière, E. Elkaïm, and E. Collet, Phys. Rev. Lett. **96**, 205503 (2006).

[48] T. Mitani, G. Saito, Y. Tokura, and T. Koda, Phys. Rev. Lett. **53**, 842 (1984).

[49] T. Mitani, Y. Kaneko, S. Tanuma, Y. Tokura, T. Koda, and G. Saito, Phys. Rev. B **35**, 427 (1987).

[50] H. Hanfland, A. Brillante, A. Girlando, and K. Syassen, Phys. Rev. B **38**, 1456 (1988).

[51] H. Okamoto, T. Koda, Y. Tokura, T. Mitani, and G. Saito, Phys. Rev. B **39**, 10 693 (1989).

[52] T. Luty, H. Cailleau, S. Koshihara, E. Collet, M. Takesada, M. H. Lemée-Cailleau, M.

Buron-Le Cointe, N. Nagaosa, Y. Tokura, E. Zienkiewicz, and B. Ouladdiaf, Europhys. Lett. **59**,619 (2002).

[53] M. Le Cointe-Buron, M. H. Lemee-Cailleau, H. Cailleau and T. Luty, Journal of Low Temperature Physics **111**, 677 (1998).

[54] J. I. Kishine, T. Luty, and K. Yonemitsu, Phys. Rev. B **69**, 075115 (2004).

[55] T. Nishikawa, Master Thesis (2012).

[56] H. Okamoto, T. Komatsu, Y. Iwasa, T. Koda, Y. Tokura, S. Koshihara, T. Mitani, and G. Saito, Synth. Met. **27**, 189 (1988).

[57] H. Okamoto, Y. Ishige, S. Tanaka, H. Kishida, S. Iwai, and Y. Tokura, Phys. Rev. B **70**, 165202 (2004).

[58] M. Ohkura, Y. Ishige, R. Sawada, H. Matsuzaki, Y. Nogami, H. Nishikawa, M. Yamashita, S. Horiuchi, and H. Okamoto, Phys. Rev. B **84**, 085136 (2011).

[59] Z. G. Soos, H. J. Keller, J. Queckborner, D.Wehe, and S. Flandoris, J. Chem. Phys. **74**, 5287 (1981).

[60] Model 2182/ 2182A Nanovoltmeter User's Manual.

[61] K. Murata, K. Yokogawa, H. Yoshino, S. Klotz, P. Munsch, A. Irizawa, M. Nishiyama,K. Iizuka, T. Nanba, T. Okada, Y. Shiraga, and S. Aoyama, Review of Scientific Instruments **79**, 085101 (2008).

[62] HP of Uwatoko group of ISSP. http://uwatoko.issp.u-tokyo.ac.jp/cubic.html

[63] V. Oison, C. Katan, P. Rabiller, M. Souhassou, and C. Koenig, Phys. Rev. B **67**, 035120 (2003).

[64] R. M. Metzger and J.B. Torrance, J. Am. Chem. Soc. **107**, 117 (1985).

[65] C.S. Jacobsen and J.B. Torrance, J. Chem. Phys. **78**, 112 (1983).

[66] P. Huai, H. Zheng, and K. Nasu, J. Phys. Soc. Jpn. **69**, 1788 (2000).

[67] V. Oison, C. Katan, P. Rabiller, M. Souhassou, and C. Koenig, Phys. Rev. B **67**, 035120 (2003).

[68] Z. G. Soos, S. A. Bewick, A. Peri, and A. Painelli, J. Chem. Phys. **120** 6712 (2004).

[69] K. Yonemitsu. Phys. Rev. B **73**, 155120 (2006).

[70] K. Yonemitsu, J. Phys. Soc. Jpn. **80**, 084707 (2011).

[71] T. Tamura, Master Thesis (2009).

[72] Y. Otsuka, H. Seo, K. Yoshimi, and T. Kato, Physica B (2012), doi:10.1016/j.physb.2012.01.031

[73] H. Terletska, J. Vucˇicˇevic´, D. Tanaskovic´, and V. Dobrosavljevic´, Phys. Rev. Lett. **107**, 026401 (2011).

[74] T. Furukawa, Doctor Thesis (2013).

[75] T. Mitani, Y. Tokura, Y. Kaneko, K. Takaoka, T. Koda, and G. Saito, Synth. Met. **19**, 515 (1987).

[76] R. Bruinsma, Per Bak, and J. B.Torrance, Phys. Rev. B **27**, 456 (1983).

[77] Z. G. Soos, H. J. Keller, J. Queckborner, D.Wehe, and S. Flandoris, J. Chem. Phys. **74**, 5287 (1981).

[78] M. Meneghetti, A. Girlando, and C. Pecile, J. Chem. Phys. **83**, 3134 (1985).

[79] G. Mihály, I. Kézsmárki, F. Zámborszky, and L. Forró. Phys. Rev. Lett. **84**, 2670 (2000).

[80] J. Moser, J. R. Cooper, D. Jérome, B. Alavi, S. E. Brown, and K. Bechgaard. Phys. Rev. Lett. **84**, 2674 (2000).